

# ATTITUDE ESTIMATION AND STABILIZATION OF A QUADROTOR AIRCRAFT

by

Fereshteh Ghashghaee

Under Supervision of Dr. Abdelhamid Tayebi

A Thesis Submitted in Partial Fulfillment  
of the Requirements for the Degree of

Master of Science  
in Control Engineering

Lakehead University, Thunder Bay, Ontario

August 2011

## Abstract

In the past few years, researchers have shown great interest in quadrotor aircraft as a platform for UAV research due to simplicity of construction as well as maintenance, ability to hover in small indoor locations or hazardous environments, vertical take-off and landing capability, etc. Attitude stabilization of a quadrotor requires accurate information about current orientation of the vehicle. With the emergence of Micro-Electro-Mechanical System (MEMS) sensors, a relatively cost-effective way for attitude estimation consists of using gyroscope, accelerometer and magnetometer devices strapped down on vehicle's center of mass. A number of previous works deal with fusing angular velocity with measurements of accelerometer and magnetometer to construct an estimation of aircraft orientation.

Through this thesis, a brief survey of attitude representation formulations for a rigid body is presented followed by a dynamical model of quadrotor aircraft. Since the uncertainties involved with sensor measurements could affect the attitude estimation, sensor calibration methods are discussed and implemented to improve the accuracy of the measurements. Also, implementation of two attitude estimation algorithms is discussed. The first algorithm uses raw vector measurements to construct an estimation of aircraft attitude using the unit-quaternion formulation while the second approach introduces a more practical observer by using filtered vector measurements. A number of experimental results are presented to illustrate the performance of each estimator in real time.

A practical experimental setup is designed and implemented on a model size quadrotor frame, featuring an inertial measurement unit (gyroscopes, 3-axis accelerometer, 3-axis magnetometer), DC motor drivers, the required power and safety plants and a microcontroller.

## Acknowledgements

I feel rather fortunate to have had *Prof. Abdelhamid Tayebi* as my supervisor throughout the time at Lakehead University, for all the guidance, encouragement and tolerance I have received from him. I am especially grateful for the critical way of thinking and discipline he has instilled into my mind, which I can benefit from for the rest of my life.

I also wish to thank the other members of my committee, *Dr. X. Liu* and *Dr. K. Liu*, both at Electrical Engineering Department of the Lakehead University.

As a special note, I would like to appreciate the help of my fellow graduate student Alain Richard in Automatic Control Lab.

Last but not least, I would like to thank my parents for their love and support. I am the most grateful to my sister who gave and continues to give me the strength and courage to fulfill my dream. My friend Jamshid whom I respect and trust the most. Without all these people, I would not be the person who I am today.

*Fereshte Ghashghaee*

# Contents

|          |                                                           |           |
|----------|-----------------------------------------------------------|-----------|
| <b>1</b> | <b>Introduction</b>                                       | <b>1</b>  |
| 1.0.1    | Brief Quadrotor History . . . . .                         | 2         |
| 1.1      | Problem Statement . . . . .                               | 4         |
| 1.1.1    | Attitude Estimation . . . . .                             | 4         |
| 1.1.2    | Attitude Stabilization . . . . .                          | 5         |
| 1.2      | Overview . . . . .                                        | 5         |
| <b>2</b> | <b>Attitude Representation</b>                            | <b>7</b>  |
| 2.1      | Euler Angles Formulation . . . . .                        | 8         |
| 2.2      | Rotation Matrix . . . . .                                 | 10        |
| 2.2.1    | Rotation About An Axis . . . . .                          | 11        |
| 2.2.2    | Composition Of Rotations . . . . .                        | 12        |
| 2.2.3    | Relationship Between Rotation Matrix and Euler Angles     | 13        |
| 2.3      | Euler Axis Formulation . . . . .                          | 14        |
| 2.4      | Quaternion Formulation . . . . .                          | 15        |
| 2.4.1    | Quaternion Algebra . . . . .                              | 15        |
| 2.4.2    | Euler-Rodrigues Quaternion Formulation . . . . .          | 18        |
| 2.4.3    | Relation Between Quaternion and Euler Angles . . . . .    | 18        |
| 2.4.4    | Relation Between Quaternion and Rotation Matrix . . . . . | 19        |
| <b>3</b> | <b>Aerodynamic Study</b>                                  | <b>22</b> |
| 3.1      | Momentum Theory Analysis . . . . .                        | 22        |
| 3.1.1    | Hovering Rotor Analysis . . . . .                         | 24        |
| 3.1.2    | Axial Movement (Climb and Descend) analysis . . . . .     | 26        |
| 3.2      | Rotor Blade Element Theory Analysis . . . . .             | 27        |
| <b>4</b> | <b>Quadrotor Concept</b>                                  | <b>33</b> |
| 4.1      | Modeling a Quadrotor Aircraft . . . . .                   | 35        |
| 4.1.1    | Modeling the Kinematics of an aircraft . . . . .          | 35        |
| 4.1.2    | Dynamical Model . . . . .                                 | 38        |
| 4.1.3    | Quadrotor Model . . . . .                                 | 41        |

|          |                                                                                    |           |
|----------|------------------------------------------------------------------------------------|-----------|
| <b>5</b> | <b>Attitude Estimation</b>                                                         | <b>43</b> |
| 5.1      | Estimation Algorithms . . . . .                                                    | 44        |
| 5.1.1    | Algorithm 1: Attitude Estimation Using Raw Vector<br>Measurements . . . . .        | 45        |
| 5.1.2    | Algorithm 2: Attitude Estimation Using Filtered Vec-<br>tor Measurements . . . . . | 47        |
| 5.2      | Measurements and Calibrations . . . . .                                            | 49        |
| 5.2.1    | Gyroscopes . . . . .                                                               | 49        |
| 5.2.2    | 3-axis Accelerometer . . . . .                                                     | 53        |
| 5.2.3    | Magnetometer . . . . .                                                             | 54        |
| <b>6</b> | <b>Attitude Control</b>                                                            | <b>59</b> |
| 6.1      | PD Control . . . . .                                                               | 60        |
| 6.1.1    | Stability Proof . . . . .                                                          | 60        |
| 6.2      | Rotors Speed Controller . . . . .                                                  | 62        |
| 6.3      | Control Design Summary . . . . .                                                   | 64        |
| 6.4      | Attitude Tracking Problem . . . . .                                                | 64        |
| <b>7</b> | <b>Simulations</b>                                                                 | <b>66</b> |
| 7.1      | Simulation 1 . . . . .                                                             | 67        |
| 7.2      | Simulation 2 . . . . .                                                             | 68        |
| 7.3      | Simulation 3 . . . . .                                                             | 68        |
| <b>8</b> | <b>Experimental Results</b>                                                        | <b>76</b> |
| 8.1      | Test-bed Platform . . . . .                                                        | 76        |
| 8.1.1    | Actuators . . . . .                                                                | 77        |
| 8.1.2    | Processor and Software . . . . .                                                   | 77        |
| 8.1.3    | Sensors . . . . .                                                                  | 78        |
| 8.1.4    | Discussion . . . . .                                                               | 79        |
| 8.2      | Experimental Data . . . . .                                                        | 80        |
| <b>9</b> | <b>Conclusion</b>                                                                  | <b>91</b> |
| 9.1      | Perspectives . . . . .                                                             | 92        |
| <b>A</b> | <b>Identification of Model Parameters</b>                                          | <b>93</b> |
| <b>B</b> | <b>Mathematical Notation and Identities</b>                                        | <b>97</b> |

# List of Figures

|     |                                                                                        |    |
|-----|----------------------------------------------------------------------------------------|----|
| 2.1 | z-x-z convention of Euler angles. . . . .                                              | 9  |
|     | (a) First rotation . . . . .                                                           | 9  |
|     | (b) Second rotation . . . . .                                                          | 9  |
|     | (c) Last rotation . . . . .                                                            | 9  |
| 2.2 | z-y-x convention of Euler angles. . . . .                                              | 9  |
|     | (a) First rotation . . . . .                                                           | 9  |
|     | (b) Second rotation . . . . .                                                          | 9  |
|     | (c) Last rotation . . . . .                                                            | 9  |
| 2.3 | Two Frames of Reference. . . . .                                                       | 10 |
| 2.4 | Composition of rotations . . . . .                                                     | 12 |
| 3.1 | The Flow Model in Momentum Theory Analysis. . . . .                                    | 23 |
| 3.2 | The Blade Model for Rotor Blade Element Theory. . . . .                                | 27 |
| 3.3 | Aerodynamic of Blade Element. . . . .                                                  | 28 |
| 3.4 | Induced Airflow Around the Blade. . . . .                                              | 29 |
| 3.5 | Aerodynamic Forces Applied to Blade Element. . . . .                                   | 29 |
| 4.1 | A quadrotor structure. . . . .                                                         | 33 |
| 4.2 | Quadrotor Motion. . . . .                                                              | 34 |
|     | (a) Roll Motion . . . . .                                                              | 34 |
|     | (b) Pitch Motion . . . . .                                                             | 34 |
|     | (c) Yaw Motion . . . . .                                                               | 34 |
| 4.3 | Forces Acting on a Quadrotor. . . . .                                                  | 39 |
| 5.1 | Collected Data From Biased X-Gyro . . . . .                                            | 50 |
| 5.2 | Collected Data From Biased Y-Gyro. . . . .                                             | 51 |
| 5.3 | Collected Data From Biased Z-Gyro. . . . .                                             | 51 |
| 5.4 | Collected Data From the Calibrated X-Gyro . . . . .                                    | 52 |
| 5.5 | Collected Data From the Calibrated Y-Gyro. . . . .                                     | 53 |
| 5.6 | Collected Data From the Calibrated Z-Gyro. . . . .                                     | 53 |
| 5.7 | Collected Data From Biased Magnetometer (through 360° rotation about z axis) . . . . . | 57 |
| 5.8 | Collected Data From Biased Magnetometer (through 360° rotation about x axis). . . . .  | 57 |

|      |                                                                                       |    |
|------|---------------------------------------------------------------------------------------|----|
| 5.9  | Collected Data From the Calibrated Magnetometer (through 360° rotation about z axis). | 58 |
| 5.10 | Collected Data From the Calibrated Magnetometer (through 360° rotation about x axis). | 58 |
| 6.1  | Electro-mechanical model of a DC motor.                                               | 63 |
| 6.2  | Control Strategy Diagram.                                                             | 64 |
| 7.1  | Aircraft Orientation, Simulation 1.                                                   | 70 |
| 7.2  | Aircraft Angles, Simulation 1.                                                        | 70 |
| 7.3  | Angular Velocity, Simulation 1.                                                       | 70 |
| 7.4  | Input Voltage, Simulation 1.                                                          | 70 |
| 7.5  | Control Effort 1, Simulation 1.                                                       | 71 |
| 7.6  | Control Effort 2, Simulation 1.                                                       | 71 |
| 7.7  | Control Effort 3, Simulation 1.                                                       | 71 |
| 7.8  | Control Effort 4, Simulation 1.                                                       | 71 |
| 7.9  | Aircraft Orientation, Simulation 2.                                                   | 72 |
| 7.10 | Aircraft Angles, Simulation 2.                                                        | 72 |
| 7.11 | Angular Velocity, Simulation 2.                                                       | 72 |
| 7.12 | Input Voltage, Simulation 2.                                                          | 72 |
| 7.13 | Control Effort 1, Simulation 2.                                                       | 73 |
| 7.14 | Control Effort 2, Simulation 2.                                                       | 73 |
| 7.15 | Control Effort 3, Simulation 2.                                                       | 73 |
| 7.16 | Control Effort 4, Simulation 2.                                                       | 73 |
| 7.17 | Aircraft Orientation, Simulation 3.                                                   | 74 |
| 7.18 | Aircraft Angles, Simulation 3.                                                        | 74 |
| 7.19 | Angular Velocity, Simulation 3.                                                       | 74 |
| 7.20 | Input Voltage, Simulation 3.                                                          | 74 |
| 7.21 | Control Effort 1, Simulation 3.                                                       | 75 |
| 7.22 | Control Effort 2, Simulation 3.                                                       | 75 |
| 7.23 | Control Effort 3, Simulation 3.                                                       | 75 |
| 7.24 | Control Effort 4, Simulation 3.                                                       | 75 |
| 8.1  | The Quadrotor Aerial Robot in Automatic Control Lab.                                  | 76 |
| 8.2  | Hardware Communication Diagram.                                                       | 77 |
| 8.3  | The Estimated $q_0$ , Experiment 1-1.                                                 | 83 |
| 8.4  | The Estimated $q_1$ , Experiment 1-1.                                                 | 83 |
| 8.5  | The Estimated $q_2$ , Experiment 1-1.                                                 | 83 |
| 8.6  | The Estimated $q_3$ , Experiment 1-1.                                                 | 83 |
| 8.7  | The Estimated $q_0$ , Experiment 1-2.                                                 | 84 |
| 8.8  | The Estimated $q_1$ , Experiment 1-2.                                                 | 84 |

|      |                                               |    |
|------|-----------------------------------------------|----|
| 8.9  | The Estimated $q_2$ , Experiment 1-2. . . . . | 84 |
| 8.10 | The Estimated $q_3$ , Experiment 1-2. . . . . | 84 |
| 8.11 | The Estimated $q_0$ , Experiment 1-3. . . . . | 85 |
| 8.12 | The Estimated $q_1$ , Experiment 1-3. . . . . | 85 |
| 8.13 | The Estimated $q_2$ , Experiment 1-3. . . . . | 85 |
| 8.14 | The Estimated $q_3$ , Experiment 1-3. . . . . | 85 |
| 8.15 | The Estimated $q_0$ , Experiment 2-1. . . . . | 86 |
| 8.16 | The Estimated $q_1$ , Experiment 2-1. . . . . | 86 |
| 8.17 | The Estimated $q_2$ , Experiment 2-1. . . . . | 86 |
| 8.18 | The Estimated $q_3$ , Experiment 2-1. . . . . | 86 |
| 8.19 | The Estimated $q_0$ , Experiment 2-2. . . . . | 87 |
| 8.20 | The Estimated $q_1$ , Experiment 2-2. . . . . | 87 |
| 8.21 | The Estimated $q_2$ , Experiment 2-2. . . . . | 87 |
| 8.22 | The Estimated $q_3$ , Experiment 2-2. . . . . | 87 |
| 8.23 | The Estimated $q_0$ , Experiment 2-3. . . . . | 88 |
| 8.24 | The Estimated $q_1$ , Experiment 2-3. . . . . | 88 |
| 8.25 | The Estimated $q_2$ , Experiment 2-3. . . . . | 88 |
| 8.26 | The Estimated $q_3$ , Experiment 2-3. . . . . | 88 |
| 8.27 | The Estimated $q_0$ , Experiment 3-1. . . . . | 89 |
| 8.28 | The Estimated $q_1$ , Experiment 3-1. . . . . | 89 |
| 8.29 | The Estimated $q_2$ , Experiment 3-1. . . . . | 89 |
| 8.30 | The Estimated $q_3$ , Experiment 3-1. . . . . | 89 |
| 8.31 | The Estimated $q_0$ , Experiment 3-2. . . . . | 90 |
| 8.32 | The Estimated $q_1$ , Experiment 3-2. . . . . | 90 |
| 8.33 | The Estimated $q_2$ , Experiment 3-2. . . . . | 90 |
| 8.34 | The Estimated $q_3$ , Experiment 3-2. . . . . | 90 |

# List of Tables

|     |                                                                                        |    |
|-----|----------------------------------------------------------------------------------------|----|
| 7.1 | Simulation Parameters . . . . .                                                        | 66 |
| 7.2 | Quadrotor Aircraft Model Parameters. . . . .                                           | 67 |
| 7.3 | Disturbance Specification in Simulation 2. . . . .                                     | 68 |
| 8.1 | Experiment 1 Parameters . . . . .                                                      | 80 |
| A.1 | Collected Data for Motor Constant Identification. . . . .                              | 94 |
| A.2 | Collected Data for Determination of Body Inertia Component<br>$I_{f\varphi}$ . . . . . | 95 |
| A.3 | Collected Data for Determination of Body Inertia Component<br>$I_{f\theta}$ . . . . .  | 96 |
| A.4 | Collected Data for Determination of Rotor Inertia $I_r$ . . . . .                      | 96 |

## List of Abbreviations

---

---

| Abbreviated Form | Description                                |
|------------------|--------------------------------------------|
| A / D            | Analog to Digital converter                |
| back e.m.f       | Back Electro-Motive Force                  |
| DCM              | Direction Cosine Matrix                    |
| DC motor         | Direct Current motor                       |
| EKF              | Extended Kalman Filtering                  |
| GPS              | Global Positioning System                  |
| IMU              | Inertial Measurement Unit                  |
| MEMS             | Micro-Electro-Mechanical Systems           |
| PD               | Proportional Derivative (control)          |
| PID              | Proportional-Integral-Derivative (control) |
| PWM              | Pulse Width Modulation                     |
| UAV              | Unmanned Aerial Vehicle                    |
| VTOL             | Vertical Take-off and Landing              |

---

## List of Important Symbols

| Symbol                                       | Description                                                                  |
|----------------------------------------------|------------------------------------------------------------------------------|
| $\psi$                                       | Roll (bank) angle                                                            |
| $\theta$                                     | Pitch (elevation) angle                                                      |
| $\varphi$                                    | Yaw (heading) angle                                                          |
| $R_B^I$                                      | Rotation transforming the inertial frame to the body-fixed frame             |
| $R_I^B$                                      | Rotation transforming the body-fixed frame to the inertial frame             |
| $s_\psi, s_\theta, s_\varphi$                | $\sin_\psi, \sin_\theta, \sin_\varphi$                                       |
| $c_\psi, c_\theta, c_\varphi$                | $\cos_\psi, \cos_\theta, \cos_\varphi$                                       |
| $Q = \begin{pmatrix} q_0 \\ q \end{pmatrix}$ | The quaternion formulation of the rigid body orientation                     |
| $\hat{Q}$                                    | The estimated attitude                                                       |
| $p$                                          | The displacement of the center of mass of the aircraft                       |
| $v$                                          | The linear velocity of the aircraft                                          |
| $\Omega$                                     | The angular velocity of the aircraft                                         |
| $S(u)$                                       | The skew-symmetric matrix associated to a vector $u$                         |
| $F$                                          | The total force affecting the aircraft in the inertial frame                 |
| $M$                                          | The total mass                                                               |
| $\tau_a$                                     | Airframe torque                                                              |
| $\tau_i$                                     | Rotor torque                                                                 |
| $G_a$                                        | Gyroscopic torque                                                            |
| $Q_i$                                        | Reactive torque                                                              |
| $\omega$                                     | The angular velocity of the rotor                                            |
| $\omega_{d,i}$                               | The desired angular velocity of the rotor                                    |
| $T$                                          | Thrust                                                                       |
| $I_f$                                        | The body Inertia matrix                                                      |
| $I_r$                                        | The momentum inertia of the rotor                                            |
| $d$                                          | The distance between the center of mass of the aircraft and the rotor center |

|                      |                                                                       |
|----------------------|-----------------------------------------------------------------------|
| $k$                  | Proportionality constant                                              |
| $b$                  | The blade characteristic coefficient                                  |
| $e_1, a_g$           | The available gravitational acceleration vector in the inertial frame |
| $e_2, \mathcal{H}_I$ | The available Earth magnetic field in the inertial frame              |
| $b_1$                | Accelerometer measurements                                            |
| $b_2$                | Magnetometer measurements                                             |
| $\hat{b}_1$          | The estimated acceleration in the body-fixed frame                    |
| $\hat{b}_2$          | The estimated magnetic field in the body-fixed frame                  |
| $B_g$                | Constant bias in gyro readouts                                        |
| $B_a$                | Constant bias in accelerometer readouts                               |
| $B_m$                | Constant bias in magnetometer readouts                                |
| $R_a$                | Armature Resistance                                                   |
| $I_a$                | Armature current                                                      |
| $V_i$                | Input voltage                                                         |
| $v_{e.m.f}$          | Back e.m.f voltage                                                    |
| $\omega_m^i$         | Motor speed                                                           |
| $\tau_m$             | Motor torque                                                          |
| $K_m$                | Motor Constant                                                        |
| $K_g$                | Gear Ratio                                                            |

# Introduction

During the last years, the interest in unmanned aerial vehicles (UAVs) has increased tremendously among the researchers. Primarily, these type of vehicles have been the subject of interest for various field of applications including military and rescue operations, surveillance, inspection, aerial remote mapping, *etc.*

Several configurations have been investigated and developed to achieve autonomous flight. The rotary wing aircraft (helicopter) is a popular structure accommodated in this category, considering its maneuverability and the capability to land / take off vertically. Quadrotor aircraft is one of the successful helicopter design configurations which has mentionable advantageous factors in comparison with the conventional helicopters. Among the expedient characteristics of a quadrotor aircraft are the simplicity of design and control, due to using the fixed-pitch rotors as well as the elimination of tail rotor.

With the arrival of MEMS technology and consequently, the availability of miniature sized inertial sensors, the past decade has witnessed a rising interest in quadrotor UAV platforms among the academic research teams. From a theoretical perspective, many authors have investigated control strategies to maintain a stable hovering condition for UAVs. However, in practice, the uncertainties and faults involved with sensor measurements as well as the highly unstable nature of flying objects make the attitude stabilization of the aerial robots a major challenge. From the control engineering point of view, this factors make the attitude control of rigid bodies an extremely interesting concept.

### 1.0.1 Brief Quadrotor History

Generally, two main generations could be defined in quadrotor design history. The earlier generation were developed seeking the capability of carrying passengers and usage in military missions. While the latest quadrotor design generation took off with the emergence of low cost and light weight MEMS sensors making it possible to build model sized aircraft capable of autonomous flight. In the past decade the quadrotors have been used mainly as a popular test bed to design an unmanned aerial vehicle. Small size, agile maneuverability, low cost, simple maintenance and the capability of flight indoor as well as outdoor environments are some advantageous characteristics, leading to a significant growth of academic research interest in quadrotor platforms as potential unmanned aerial vehicles.

The history of quadrotor design dates back more than a century. In summer of 1907, only four years after the Wright brothers recorded the first controllable flight by an airplane, Louis and Jacques Breguet in association with Professor Charles Richet built a quadrotor named Gyroplane [23]. This model was an X-shaped steel construction. At the end of each arm, a four blade rotor was mounted. One pair of diagonally opposed rotors rotated in a clockwise direction while the other pair rotated counter-clockwise. All rotors were driven by a 40/45 h.p Antoinette piston-engine mounted in the rectangular central chassis which was considered to protect pilot and engine. Pilot M.Volumard was chosen for flight tests in which the vehicle took off with success and could hover in low altitudes. Even tough Breguet-Richet quadrotor aircraft can not take the credit for the first free flight (during experiments, each rotor was kept in a steady condition with assistance of a man.), but it was the first quadrotor aircraft with the experiment of a vertical take off with the help of a pilot (see more details in [23]).

The first distance flight by a quadrotor was recorded on April 14, 1924 in France for Etienne Oemichen's second helicopter [27]. This quadrotor was built in 1920, an X-shaped frame with one large propeller at the end of each arm. Five small horizontal propellers were added to achieve lateral stability as well as one mounted at the nose for steering and another couple of propellers for forward motion. All propellers were driven by a single 120hp Le Rhone rotary engine. This quadrotor showed a considerable degree of stability and controllability, considering the limited facilities available at the time. However, Oemichen was dissatisfied with the limited altitude the aircraft could reach during several experiments, resulting in the abandon of the multi rotor schemes to concentrate on single rotor layouts.

In almost the same period of time, in 1922 US army financed the experiments of Dr.George De Bothezat to build a four rotor aircraft powered by one main

engine [9]. The frame was X-shaped with arms slightly inclined inward. Even though the aircraft was relatively heavy weighted, it could record stable flight of 90 seconds (see references [23] and [4] for more details). Due to high cost and relatively insufficient performance, the US army gradually lost interest in the project, causing the experiments to stop from further possible achievements.

The ten years following World War II witnessed the start and stop of a large number of companies attempting to manufacture and sell a variety of helicopter configurations. Converawings company in Amityville, New York was the company that sponsored D.H. Kaplan's quadrotor project [17]. This model had an H-shaped configuration, four rotors were mounted at the very end of arms. The system was designed such that almost all movements could be achieved using four rotors. For instance, increasing the pitch of two rotors on one side while decreasing those of the two rotors on the other side would lead to roll movement. For moving right or left, the four rotors would be inclined slightly inward from the vertical position. Also, to generate the yaw motion about the vertical axis of the aircraft, the thrust generated by the rotors could be changed leading to the desired movement. This quadrotor was flown successfully on Long Island in 1956 by its designer and test pilot, D.H.Kaplan. Due to lack of orders for commercial or military versions however, the project was terminated later.

As mentioned earlier, the recent advent of light weight miniature electronics has spurred the interest in building small sized quadrotors as unmanned aircraft. The first modern quadrotor was built by *Area Fifty One* in 1996, later improved to manufacture the commercial radio controlled aerial robot called *Draganflyer*<sup>®</sup> by the well-known Canadian company, RCToys (refer to [15] and also rctoys website at [1]). Since then, a large number of groups and individuals have worked on the development of the quadrotor aerial robot. In fact, the low maintenance requirement and the symmetrical mechanical configuration of the quadrotor makes it a wise choice as a test bed to validate different new flight control and stabilization algorithms developed by academic research teams. For instance, in 2001, a very small scaled quadrotor aerial robot was initially developed in the Mesicopter project [2] sponsored by Stanford University, investigating the challenging control and manufacture of this aircraft. A vision based control algorithm was used through this particular project leading to successful hovering. Another successor in the modern generation of quadrotor aerial robots was developed through *STAR-MAC* project [3] widely known for aggressive maneuverability and successful multi agent flights.

For nearly a decade now, the unmanned aerial vehicles have been subject of research in Automatic Control lab, at Lakehead University (see for instance

[26] and [35]). Through this thesis the challenging concept of design and implementation of a quadrotor aerial robot is investigated, seeking the required attitude stabilization for a hovering flight.

## 1.1 Problem Statement

Developing an autonomous quadrotor aerial robot could be divided in two main tasks; attitude estimation and attitude stabilization. Through the following sections, a brief description concerning each of these problems is given.

### 1.1.1 Attitude Estimation

Determination of the orientation of a rigid body relative to an inertial frame of reference is a fundamental problem in a number of engineering disciplines, including aerial or under water robotics, aeronautics and space engineering. This problem has been studied extensively over the past years. Different types of formulations can be used to represent the orientation of an object. Euler angles, Rodriguez parametrization, rotation matrix and quaternion formulation are among the common attitude representation methods. There are a considerable number of publications available, discussing the orientation formulations, advantages and drawbacks of each of these methods [32], [38], [39].

The prenominal requirement to achieve attitude balance is an accurate estimation of the vehicle orientation. Theoretically, the kinematics of motion, suggest that the attitude of a rigid body can be calculated while its exact angular velocity is known. However, in practice the gyro sensors used for angular velocity measurements are not flawless. In long term missions specifically, gyros drift and uncertainties over time cause errors to accumulate, making the integration of kinematic equations an impractical way to estimate the attitude. This fact reveals the challenging side of attitude estimation problem.

A common approach to obtain a relatively accurate attitude estimation is using inertial sensors; accelerometers and magnetometers in addition to gyroscopes. Fusion of inertial measurements to develop attitude observers has been the subject of many valuable discussions in literature [19], [41], [12].

In practice, the measurements provided by low cost inertial sensors are contaminated with noise, biases and misalignments. The compensation for measurement uncertainties and cancelation of noise as far as possible, are yet the other important tasks to deal with through the attitude estimation process. Considering the effect of noise on accelerometer and magnetometer in high

frequencies, an appropriate solution to cancel out the noise is the well-known low pass filtering method. However, the limitation in bandwidth decrease must be taken into account, since there is a compromise between measurement bandwidth and sensor response time.

Through this project, the problems involved with the attitude estimation are addressed.

### 1.1.2 Attitude Stabilization

As far as the orientation information of the aircraft is provided accurately, a feedback control scheme can be developed to regulate the airframe attitude into a stable hovering condition. In literature, a number of authors have presented control algorithms to solve the attitude stabilization problem, assuming a precise estimation of the aircraft attitude is available as well as bias-free rate gyro measurement. In majority of these publications, a type of PD controller is presented using the orientation and angular velocity as proportional and derivative feedback [40], [36], [42].

Attitude stabilization problem can be also investigated considering the biased angular velocity measurements. While the attitude of the rigid body is assumed to be known, a variety of bias observers are presented (for instance in [24]). The literature, has taken even a further step ahead, suggesting the development of attitude control designs in the absence of angular velocity measurements. Reference [41] represents one of these type of controllers.

In this project, using the rate gyro measurements in addition to the attitude information obtained through the appropriate estimation algorithms, the stabilization of a quadrotor aerial robot is investigated in details.

## 1.2 Overview

This thesis begins with a description of the most common attitude representations used in literature. The characteristics of each formulation method is discussed briefly while the advantages and drawbacks are reviewed. The relation between these formulations is also given. Chapter three starts with a brief study of aerodynamics and goes further to give a summarized analysis of aerodynamic elements in a hovering flight. Through this chapter two well known aerodynamic analyses are presented. This document continues in Chapter four which overviews the basic information involved with a quadrotor aircraft. This chapter begins with a description of the quadrotor aerial robot structure and different possible flight regimes followed by a dynamic modeling of the aircraft as a vital task for attitude control. The

attitude estimation algorithms used through this project, are presented in chapter five. Two different estimation algorithms [41] are discussed while the stability proof is presented for each of them. This chapter continues with the calibration methods used in this project for the required sensors. Chapter six contains the attitude stabilization strategy selected through this project. A PD control approach is presented accompanied by the stabilization proof. The system is simulated in chapter seven. While the discussed controller is applied, the simulation results are presented, showing the satisfactory performance of stabilization algorithm. Chapter eight describes the experimental setup which has been used in this project to implement the control algorithms. The performance of attitude observers are validated using the real-time data. Finally, in chapter nine provides some possible future works followed by a concluding discussion.

## Attitude Representation

The simulation and description of motion are important issues in many modern technologies including aircraft and spacecraft technology. In a more general point of view, for all rigid bodies there is a need to describe both position and orientation in either an inertial coordinate system or a frame fixed to the body of moving object.

There are considerable varieties of textbooks and papers dealing with different representations of attitude specially in robotics fields. ( See for instance, [39] ). Also, [32] is one of many sources in literature dealing with attitude representation and dynamics of aircraft exclusively. Reference [38] is an example of a comprehensive paper written on attitude representations.

There are several existing methods to represent the orientation of a rigid body and relating non-inertial coordinates to inertial ones. Each of these known methods has a number of advantages and disadvantages, making them useful depending on the application they are used for.

In the following sections,  $x_I, y_I, z_I$  are considered as orthogonal unit vectors describing the inertial coordinate system. This inertial frame is fixed to the Earth. On the other hand,  $x_B, y_B, z_B$  are orthogonal unit vectors forming the body-fixed frame. This frame is rigidly attached to the center of mass of the rigid body. The orientation of the rigid body describes how these two frames are located with respect to each other.

## 2.1 Euler Angles Formulation

The orientation of the non-inertial frame relative to the inertial frame can be described in terms of three consecutive rotations about the body-fixed unit axes  $x_B, y_B, z_B$  through three Euler angles. Depending on the sequence of rotations about three axes, 12 independent ways are possible to define a set of Euler angles. Starting from the inertial frame, three rotations are performed about one of three body-fixed axes, arriving to the final frame. None of two consecutive rotations should be about the same axis.

When the first and the last of three rotations are about the same axis while the second rotation is about a different one, the set of Euler angles is called a **Symmetric Set**. There are six symmetric sets of Euler angles :

$$\begin{aligned} \theta_x \rightarrow \theta_y \rightarrow \theta_x, \quad \theta_x \rightarrow \theta_z \rightarrow \theta_x, \quad \theta_y \rightarrow \theta_x \rightarrow \theta_y \\ \theta_y \rightarrow \theta_z \rightarrow \theta_y, \quad \theta_z \rightarrow \theta_x \rightarrow \theta_z, \quad \theta_z \rightarrow \theta_y \rightarrow \theta_z \end{aligned}$$

Here,  $\theta$  is considered to show an Euler angle. The index denotes the axis around which the rotation has occurred. For instance,  $\theta_x \rightarrow \theta_y \rightarrow \theta_x$  expresses the sequence of Euler angles as the first and last rotations are about  $x_B$  and the second rotation is about  $y_B$ .

The remaining Euler angles sets are named **Asymmetric Sets**;

$$\begin{aligned} \theta_x \rightarrow \theta_y \rightarrow \theta_z, \quad \theta_z \rightarrow \theta_y \rightarrow \theta_x, \quad \theta_y \rightarrow \theta_x \rightarrow \theta_z \\ \theta_z \rightarrow \theta_x \rightarrow \theta_y, \quad \theta_x \rightarrow \theta_z \rightarrow \theta_y, \quad \theta_y \rightarrow \theta_z \rightarrow \theta_x \end{aligned}$$

Each of these 12 sets can be used for attitude representation. For example  $\theta_z \rightarrow \theta_x \rightarrow \theta_z$  is regularly used in literature for orbital mechanics and the quantum theory of angular motion. Figure (2.1) shows the sequence of this symmetric Euler angles set.

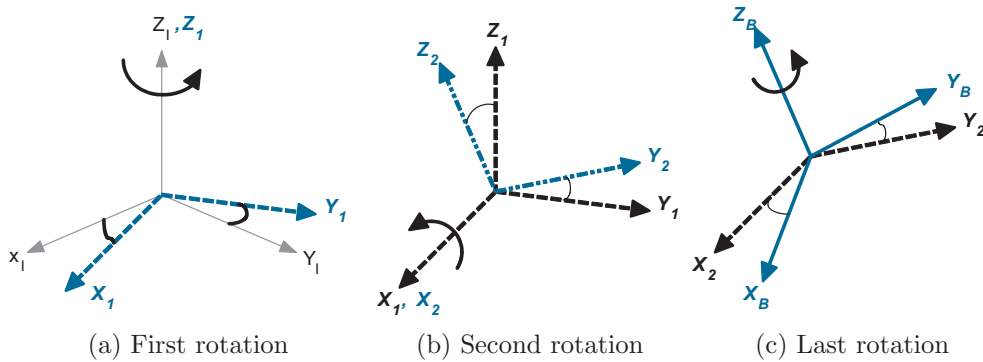


Figure 2.1: z-x-z convention of Euler angles.

Aerodynamic textbooks and aeronautics community, commonly use  $\theta_z \rightarrow \theta_y \rightarrow \theta_x$  convention of Euler angles for attitude representation. These three angles usually written as  $\psi$ ,  $\theta$  and  $\varphi$  are often called **roll** (or bank) angle, **pitch** (or elevation) angle and **yaw** (or heading) angle of an aircraft, respectively. Figure (2.2) shows the sequence of this particular Euler angle set.

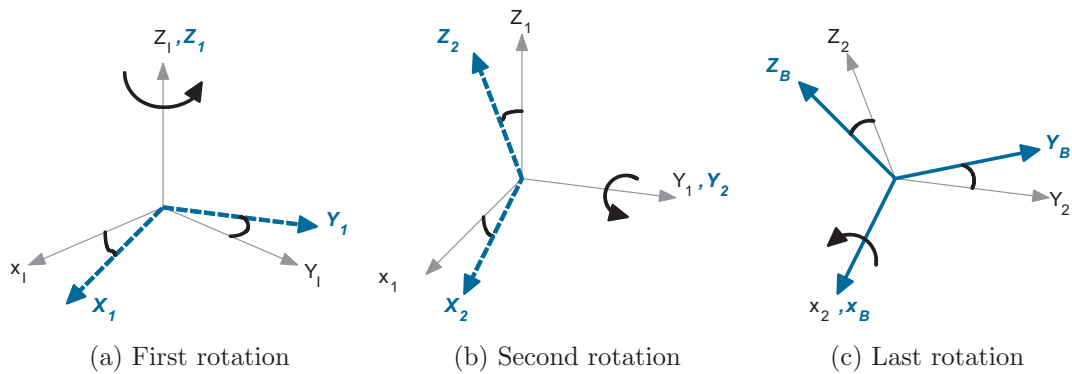


Figure 2.2: z-y-x convention of Euler angles.

As it is well illustrated in figure (2.2), starting from inertial frame, body fixed coordinate system is rotated by an angle  $\varphi$  about the  $z$  axis. Next, the revolved reference frame is rotated about the new  $y$  axis by an angle  $\theta$ . In the last rotation, the revolved reference frame is rotated about the new  $x$  axis by an angle of  $\psi$  arriving to the final body-fixed frame of reference.

## 2.2 Rotation Matrix

Imagine a rigid body in space with a frame attached to its center of mass. Finding the relation between such coordinate system and the inertial frame leads to the orientation representation of the moving object. A rotation matrix, also referred to as direction cosine matrix (DCM), is a common method to describe the transformation from one frame to another.

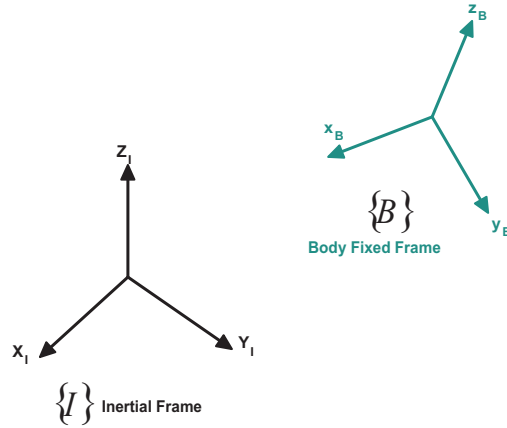


Figure 2.3: Two Frames of Reference.

When  $R_B^I$  is considered as the rotation transforming the inertial frame to body-fixed frame, this transformation can be described as

$$\begin{bmatrix} x_B \\ y_B \\ z_B \end{bmatrix} = R_B^I \begin{bmatrix} x_I \\ y_I \\ z_I \end{bmatrix} \quad (2.1)$$

Therefore,

$$R_B^I = \begin{bmatrix} x_I \cdot x_B & y_I \cdot x_B & z_I \cdot x_B \\ x_I \cdot y_B & y_I \cdot y_B & z_I \cdot y_B \\ x_I \cdot z_B & y_I \cdot z_B & z_I \cdot z_B \end{bmatrix} \quad (2.2)$$

Similarly, it is possible to transform the body fixed frame coordinates to inertial frame ;

$$\begin{bmatrix} x_I \\ y_I \\ z_I \end{bmatrix} = R_I^B \begin{bmatrix} x_B \\ y_B \\ z_B \end{bmatrix} \quad (2.3)$$

which yields to

$$R_I^B = \begin{bmatrix} x_B \cdot x_I & y_B \cdot x_I & z_B \cdot x_I \\ x_B \cdot y_I & y_B \cdot y_I & z_B \cdot y_I \\ x_B \cdot z_I & y_B \cdot z_I & z_B \cdot z_I \end{bmatrix} \quad (2.4)$$

Obviously  $R_I^B$  is the inverse of transformation matrix  $R_B^I$ . Adding this to the fact that

$$\begin{aligned} x_B \cdot x_I &= x_I \cdot x_B, \\ y_B \cdot y_I &= y_I \cdot y_B, \\ z_B \cdot z_I &= z_I \cdot z_B. \end{aligned}$$

one can conclude

$$R_I^B = (R_B^I)^{-1} = (R_B^I)^T. \quad (2.5)$$

### 2.2.1 Rotation About An Axis

Imagine a rigid body starting from the inertial frame and performing a rotation by an angle  $\theta$  about  $y_B$  axis. Note that, during this rotation  $y_B$  axis doesn't move and all three coordinate axes remain orthogonal to one another while their magnitude is unity.

$$y_B \cdot y_I = 1,$$

$$\|x_B\| = \|y_B\| = \|z_B\| = \|x_I\| = \|y_I\| = \|z_I\| = 1.$$

Also,

$$y_B \cdot x_I = 0,$$

$$y_B \cdot z_I = 0,$$

$$x_B \cdot y_I = 0,$$

$$z_B \cdot y_I = 0.$$

Taking the above expressions into account, the rotation matrix is constructed as

$$R = \begin{bmatrix} x_B \cdot x_I & 0 & z_B \cdot x_I \\ 0 & 1 & 0 \\ x_B \cdot z_I & 0 & z_B \cdot z_I \end{bmatrix} = \begin{bmatrix} \cos \theta & 0 & \cos(\frac{\pi}{2} + \theta) \\ 0 & 1 & 0 \\ \cos(\frac{\pi}{2} - \theta) & 0 & \cos \theta \end{bmatrix}$$

Therefore, the rotation matrix resultant from a rotation about  $y$  axis by an angle  $\theta$  is given by

$$R_{y,\theta} = \begin{bmatrix} \cos \theta & 0 & -\sin \theta \\ 0 & 1 & 0 \\ \sin \theta & 0 & \cos \theta \end{bmatrix} \quad (2.6)$$

Similarly,  $R_{x,\psi}$  is described as the matrix indicating a rotation by an angle  $\psi$  about  $x$  axis while  $R_{z,\varphi}$  represents a rotation about  $z$  axis by an angle  $\varphi$ . Such transformation matrices are given as

$$R_{x,\psi} = \begin{bmatrix} 1 & 0 & 0 \\ 0 & \cos \psi & \sin \psi \\ 0 & -\sin \psi & \cos \psi \end{bmatrix} \quad (2.7)$$

$$R_{z,\varphi} = \begin{bmatrix} \cos \varphi & \sin \varphi & 0 \\ -\sin \varphi & \cos \varphi & 0 \\ 0 & 0 & 1 \end{bmatrix} \quad (2.8)$$

Generally, when we have the rotation matrix  $R$  relating two coordinate frames to each other, any given vector  $\vec{u}$  defined with respect to one frame can be expressed with respect to the coordinate axes of the other frame,

$$\vec{u}_B = R_B^I \vec{u}_I \quad (2.9)$$

### 2.2.2 Composition Of Rotations

Imagine  $R_1$  as the matrix transforming frame  $A$  to frame  $B$ . As it is shown in figure (2.4), let  $R_2$  denote the transformation from frame  $A$  to frame  $B$ .

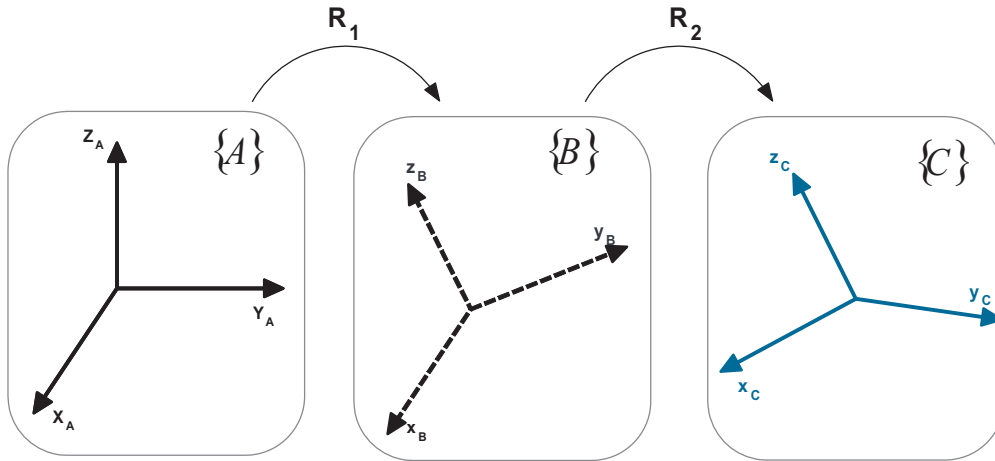


Figure 2.4: Composition of rotations

As discussed earlier, with a glance at equation (2.1), for transformation from frame  $B$  to frame  $C$  we can write

$$\begin{bmatrix} x_B \\ y_B \\ z_B \end{bmatrix} = R_1 \begin{bmatrix} x_A \\ y_A \\ z_A \end{bmatrix} \quad (2.10)$$

In a similar way, we can define the transformation from frame  $B$  to frame  $C$  as

$$\begin{bmatrix} x_C \\ y_C \\ z_C \end{bmatrix} = R_2 \begin{bmatrix} x_B \\ y_B \\ z_B \end{bmatrix} \quad (2.11)$$

In the above equation, if we replace frame  $B$  by the description given by equation (2.10), frame  $C$  can be related to frame  $A$  as

$$\begin{bmatrix} x_C \\ y_C \\ z_C \end{bmatrix} = R_2 R_1 \begin{bmatrix} x_A \\ y_A \\ z_A \end{bmatrix} \quad (2.12)$$

In other words, if we call  $R$  as the direct rotation matrix transforming frame  $A$  to frame  $C$ , such a rotation can be expressed as

$$R = R_2 R_1 \quad (2.13)$$

Note that the sequence of rotation matrices being multiplied by each other is the reverse order of the sequence of transformations happening.

### 2.2.3 Relationship Between Rotation Matrix and Euler Angles

The rotation matrix can be formed using any Euler angles set. Recalling  $\theta_z \rightarrow \theta_y \rightarrow \theta_x$  as the common set used in aircraft dynamics, consider a vector  $\vec{u}$  with components  $u_{x_I}, u_{y_I}, u_{z_I}$  in inertial frame. As it was explained in section 2.1, three rotations occur in sequence, arriving to the current body-fixed frame. Therefore, the rotation matrix for such transformation is given by

$$R = R_{(x,\psi)} R_{(y,\theta)} R_{(z,\varphi)} \quad (2.14)$$

If we call  $u_{x_B}, u_{y_B}, u_{z_B}$  the components of an arbitrary vector  $\vec{u}$  in the body-fixed coordinate system, using equations (2.6), (2.7) and (2.8) one can write

$$\begin{bmatrix} u_{x_B} \\ u_{y_B} \\ u_{z_B} \end{bmatrix} = \begin{bmatrix} 1 & 0 & 0 \\ 0 & \cos \psi & \sin \psi \\ 0 & -\sin \psi & \cos \psi \end{bmatrix} \begin{bmatrix} \cos \theta & 0 & -\sin \theta \\ 0 & 1 & 0 \\ \sin \theta & 0 & \cos \theta \end{bmatrix} \begin{bmatrix} \cos \varphi & \sin \varphi & 0 \\ -\sin \varphi & \cos \varphi & 0 \\ 0 & 0 & 1 \end{bmatrix} \begin{bmatrix} u_{x_I} \\ u_{y_I} \\ u_{z_I} \end{bmatrix} \quad (2.15)$$

Considering  $c$  and  $s$  as the abbreviated forms for the functions  $\cos$  and  $\sin$  respectively, we can wrap equation (2.15) as

$$\begin{bmatrix} u_{xB} \\ u_{yB} \\ u_{zB} \end{bmatrix} = \begin{bmatrix} c_\theta c_\varphi & c_\theta s_\varphi & -s_\theta \\ s_\psi s_\theta c_\varphi - c_\psi s_\varphi & s_\psi s_\theta c_\varphi + c_\psi c_\varphi & s_\psi c_\theta \\ c_\psi s_\theta c_\varphi + s_\psi s_\varphi & c_\psi s_\theta s_\varphi - s_\psi c_\varphi & c_\psi c_\theta \end{bmatrix} \begin{bmatrix} u_{xI} \\ u_{yI} \\ u_{zI} \end{bmatrix} \quad (2.16)$$

It is clear that for transforming the body-fixed frame  $B$  to the inertial frame, one could use  $R^T$ , recalling the fact expressed by equation (2.5).

When the rotation matrix is known, by a simple comparison of equation (2.9) and equation (2.16), one can calculate the corresponding  $z \rightarrow y \rightarrow x$  Euler angles set.

Consider a given rotation matrix

$$R = \begin{bmatrix} R_{11} & R_{12} & R_{13} \\ R_{21} & R_{22} & R_{23} \\ R_{31} & R_{32} & R_{33} \end{bmatrix}$$

Comparing with the corresponding matrix in equation (2.16), we can write

$$\begin{cases} \psi = \tan^{-1}\left(\frac{R_{23}}{R_{33}}\right) & : \theta \neq \pm \frac{\pi}{2} \\ \theta = \sin^{-1}(-R_{13}) \\ \varphi = \tan^{-1}\left(\frac{R_{12}}{R_{11}}\right) & : \theta \neq \pm \frac{\pi}{2} \end{cases} \quad (2.17)$$

When pitch angle is  $\pm \frac{\pi}{2}$ , a singularity occurs during calculation of Euler angles. This phenomenon is commonly referred to as *gimbal lock* problem. One might use another method for attitude representation to avoid these types of singularities.

## 2.3 Euler Axis Formulation

The orientation of the body-fixed frame with respect to the inertial frame can be represented in terms of a rotation by an angle  $\Theta$  about a special axis  $E$  called **Euler axis**.

This representation gives four components to describe the orientation, three of which are three components of the vector  $E$  called  $E_x, E_y, E_z$  respectively and the fourth component is the rotation angle  $\Theta$ . The vector describing Euler axis  $E$  is an arbitrary vector in magnitude. The most usual solution that comes to mind to remove this arbitrary characteristic is normalization of Euler axis vector,

$$E_x^2 + E_y^2 + E_z^2 \equiv 1. \quad (2.18)$$

While vector  $E$  remains invariant through the rotation, it has the same orientation in both inertial and body-fixed frames, *i.e.*,

$$\begin{bmatrix} E_{x_B} \\ E_{y_B} \\ E_{z_B} \end{bmatrix} = \begin{bmatrix} E_{x_I} \\ E_{y_I} \\ E_{z_I} \end{bmatrix} \quad (2.19)$$

Refereing to the early works done by Euler, a formula is derived for attitude representation (see for instance [1],[2]) called *Euler Formula*. Given the components of an arbitrary vector  $u$  in the inertial coordinate system,  $u$  can be expressed in body-fixed frame as

$$\begin{bmatrix} u_{x_B} \\ u_{y_B} \\ u_{z_B} \end{bmatrix} = \begin{bmatrix} E_{xx} + \cos \Theta & E_{xy} + E_z \sin \Theta & E_{xz} - E_y \sin \Theta \\ E_{xy} - E_z \sin \Theta & E_{yy} + \cos \Theta & E_{yz} + E_x \sin \Theta \\ E_{xz} + E_y \sin \Theta & E_{yz} - E_x \sin \Theta & E_{zz} + \cos \Theta \end{bmatrix} \begin{bmatrix} u_{x_I} \\ u_{y_I} \\ u_{z_I} \end{bmatrix} \quad (2.20)$$

where  $E_{ij} = E_i E_j (1 - \cos \Theta)$  and  $i, j \in \{x, y, z\}$ .

## 2.4 Quaternion Formulation

Quaternion formulation is yet another attitude representation method. Even though the detailed theory of a noncommutative algebraic system known as quaternion was first developed in nineteenth century by the famous mathematician Sir William Hamilton, it is clear that he didn't develop quaternion algebra merely to describe orientation of rigid bodies. Euler-Rodrigues symmetric parameters are a special subset of quaternions used to describe rotational transformations. In the following sections, first of all a brief survey is given on quaternion definition and relations. More information on the theory could be found in [18] and [16]. Once the preliminary descriptions on quaternion algebraic relations are discussed, the Euler-Rodrigues formulation of rigid body orientation is reviewed .

### 2.4.1 Quaternion Algebra

Let

$$Q = q_0 + iq_1 + jq_2 + kq_3 \quad (2.21)$$

denote the quaternion expression when  $q_0, q_1, q_2$  and  $q_3$  are called *constituents* of quaternion  $Q$ . Quaternion constituents can take any real quantity while  $i, j$  and  $k$  are three imaginary quantities with no linear relation to each other.

Let  $P = p_0 + ip_1 + jp_2 + kp_3$  represent another quaternion. Two quaternions  $P$  and  $Q$  are said to be equal only if four constituents of them are equal. *i.e.*,

$$Q = P \iff \begin{cases} q_0 = p_0, \\ q_1 = p_1, \\ q_2 = p_2, \\ q_3 = p_3. \end{cases} \quad (2.22)$$

### Quaternion Addition and Substraction

Addition and subtraction of two quaternions are defined simply, by

$$Q \pm P = q_0 \pm p_0 + i(q_1 \pm p_1) + j(q_2 \pm p_2) + k(q_3 \pm p_3) \quad (2.23)$$

In other words, the sum or subtraction of two quaternions is equal to the sum or subtraction of constituents of those quaternions.

### Quaternion Multiplication

Multiplication of two quaternion sets can be defined by considering the product as

$$\begin{aligned} QP &= (q_0 + iq_1 + jq_2 + kq_3)(p_0 + ip_1 + jp_2 + kp_3) \\ &= q_0p_0 + i(q_0p_1 + p_0q_1) + j(q_0p_2 + p_0q_2) + k(q_0p_3 + p_0q_3) \\ &\quad + i^2q_1p_1 + j^2q_2p_2 + k^2q_3p_3 + ijq_1p_2 + jiq_2p_1 \\ &\quad + ikq_1p_3 + kiq_3p_1 + jkq_2p_3 + kjq_3p_2 \end{aligned} \quad (2.24)$$

Since the product of two quaternion sets is defined to be of quaternion nature, nine expressions are adopted to cancel out the last nine terms in equation (2.24) ;

$$\begin{aligned} i^2 &= j^2 = k^2 = -1, \\ ij &= k, \quad jk = i, \quad ki = j, \\ ji &= -k, \quad kj = -i, \quad ik = -j. \end{aligned}$$

Taking above expressions into account, let  $q$  denote the imaginary constituents of  $Q$  as a vector while  $q_0$  is the scalar part. If we use the same notation to describe a quaternion generally, the multiplication of two quaternion can be shown as

$$Q * P = \begin{pmatrix} q_0 \\ q \end{pmatrix} * \begin{pmatrix} p_0 \\ p \end{pmatrix} = \begin{pmatrix} q_0p_0 - q^T p \\ q_0p + p_0q + q \times p \end{pmatrix} \quad (2.25)$$

Quaternion multiplication possesses two critical characteristics which are common in regular multiplication; Distributivity and associativity in quaternion multiplication are those properties that make quaternion system calculations relatively similar to those of ordinary algebra.

When we say quaternion multiplication is distributive, it means

$$P * (Q + K) = P * Q + P * K \quad (2.26)$$

Where  $P$ ,  $Q$  and  $K$  denote three quaternions. Also, when calling quaternion multiplication associative it means one can associate quaternions among themselves in any matter, as far as it doesn't change their order.

$$P * (Q * K) = (P * Q) * K = P * Q * K \quad (2.27)$$

Despite similar characteristics in quaternion multiplication and ordinary algebraic multiplication, there is an extremely important difference between properties of these two multiplications. Quaternion multiplication is not commutative,

$$P * Q \neq Q * P. \quad (2.28)$$

### Quaternion Inverse

The conjugate of a quaternion is defined as

$$Q^* = \begin{pmatrix} q_0 \\ -q \end{pmatrix} \quad (2.29)$$

while the norm of a quaternion is given by

$$\|Q\| = q_0^2 + q^T q \quad (2.30)$$

Using the latest two equations, the inverse of a quaternion is considered to be of quaternion nature. As it has been mentioned in [38], the inverse of a quaternion can be obtained from the following equation

$$Q^{-1} = \frac{Q^*}{\|Q\|^2} = \frac{1}{\|Q\|^2} \begin{pmatrix} q_0 \\ -q \end{pmatrix} \quad (2.31)$$

Note that when a quaternion is multiplied by its inverse, the result is always an *identity quaternion*,  $Q_I$ .

$$Q * Q^{-1} = Q_I = \begin{pmatrix} 1 \\ 0 \end{pmatrix} \quad (2.32)$$

### 2.4.2 Euler-Rodrigues Quaternion Formulation

A simple change of variables can relate Euler axis formulation to another representation in quaternion form, known as Euler-Rodrigues formulation. Four components of Euler axis representation help to define four constituents of corresponding quaternion as

$$Q_B^I = \begin{pmatrix} q_0 \\ q_1 \\ q_2 \\ q_3 \end{pmatrix} = \begin{pmatrix} \cos\left(\frac{\Theta}{2}\right) \\ E_x \sin\left(\frac{\Theta}{2}\right) \\ E_y \sin\left(\frac{\Theta}{2}\right) \\ E_z \sin\left(\frac{\Theta}{2}\right) \end{pmatrix} \quad (2.33)$$

It can be easily noted that

$$q_0^2 + q_1^2 + q_2^2 + q_3^2 = \cos^2\left(\frac{\Theta}{2}\right) + (E_x^2 + E_y^2 + E_z^2) \sin^2\left(\frac{\Theta}{2}\right)$$

Using the fact that Euler axis vector  $E$  is supposed to be unity, we can write

$$\|Q\|^2 = q_0^2 + q_1^2 + q_2^2 + q_3^2 = 1. \quad (2.34)$$

Note that, using Euler-Rodrigues formula, it can be easily proved that negating quaternion doesn't change the orientation,

$$-Q = \begin{pmatrix} -q_0 \\ -q_1 \\ -q_2 \\ -q_3 \end{pmatrix} = \begin{pmatrix} -\cos\left(\frac{\Theta}{2}\right) \\ -E_x \sin\left(\frac{\Theta}{2}\right) \\ -E_y \sin\left(\frac{\Theta}{2}\right) \\ -E_z \sin\left(\frac{\Theta}{2}\right) \end{pmatrix} = \begin{pmatrix} \cos\left(\frac{\Theta+2\pi}{2}\right) \\ E_x \sin\left(\frac{\Theta+2\pi}{2}\right) \\ E_y \sin\left(\frac{\Theta+2\pi}{2}\right) \\ E_z \sin\left(\frac{\Theta+2\pi}{2}\right) \end{pmatrix} \quad (2.35)$$

### 2.4.3 Relation Between Quaternion and Euler Angles

As it was mentioned earlier, even though it is easy to visualize Euler angles, there are some singularities involved with Euler angles formulation when it comes to attitude representation of a rigid body. Using quaternion representation to describe the attitude has the advantage of singularity-free representation in comparison with Euler angles method. In order to visualize the results given by quaternion representation, It's possible to relate the quaternion to Euler angles. We can obtain such a relation by combining Euler-Rodrigues formula with equations (2.16) and (2.20). Therefore,

$$\begin{bmatrix} q_0^2 + q_1^2 - q_2^2 - q_3^2 & 2(q_1q_2 + q_3q_0) & 2(q_1q_3 - q_2q_0) \\ 2(q_1q_2 - q_3q_0) & q_0^2 - q_1^2 + q_2^2 - q_3^2 & 2(q_2q_3 + q_1q_0) \\ 2(q_1q_3 + q_2q_0) & 2(q_2q_3 + q_1q_0) & q_0^2 - q_1^2 - q_2^2 + q_3^2 \end{bmatrix} = \begin{bmatrix} c_\theta c_\psi & c_\theta s_\psi & -s_\theta \\ s_\psi s_\theta c_\psi - c_\psi s_\psi & s_\psi s_\theta c_\psi + c_\psi c_\psi & s_\psi c_\theta \\ c_\psi s_\theta c_\psi + s_\psi s_\psi & c_\psi s_\theta s_\psi - s_\psi c_\psi & c_\psi c_\theta \end{bmatrix} \quad (2.36)$$

If we go on the same process as in section 2.2.3 to define three Euler angles, one obtains,

$$\begin{cases} \psi = \tan^{-1}\left(\frac{2(q_0q_1+q_2q_3)}{q_0^2-q_1^2-q_2^2+q_3^2}\right) & : -\pi \leq \psi \leq \pi \\ \theta = \sin^{-1}(2(q_0q_2 - q_1q_3)) & : -\frac{\pi}{2} < \theta < \frac{\pi}{2} \\ \varphi = \tan^{-1}\left(\frac{2(q_0q_3+q_1q_2)}{q_0^2+q_1^2-q_2^2+q_3^2}\right) & : -\pi \leq \varphi \leq \pi \end{cases} \quad (2.37)$$

According to [32], the quaternion representation of attitude can be obtained when the Euler angles are given. Equation (2.36) provides nine separate scalar equations. Simplifying these equations and recalling half angle identities lead to finding the relation between quaternion components and Euler angles. Such a relation is described as

$$\begin{bmatrix} q_0 \\ q_1 \\ q_2 \\ q_3 \end{bmatrix} = \pm \begin{bmatrix} C_{\frac{\psi}{2}}C_{\frac{\theta}{2}}C_{\frac{\varphi}{2}} + S_{\frac{\psi}{2}}S_{\frac{\theta}{2}}S_{\frac{\varphi}{2}} \\ S_{\frac{\psi}{2}}C_{\frac{\theta}{2}}C_{\frac{\varphi}{2}} - C_{\frac{\psi}{2}}S_{\frac{\theta}{2}}S_{\frac{\varphi}{2}} \\ C_{\frac{\psi}{2}}S_{\frac{\theta}{2}}C_{\frac{\varphi}{2}} + S_{\frac{\psi}{2}}C_{\frac{\theta}{2}}S_{\frac{\varphi}{2}} \\ C_{\frac{\psi}{2}}C_{\frac{\theta}{2}}S_{\frac{\varphi}{2}} - S_{\frac{\psi}{2}}S_{\frac{\theta}{2}}C_{\frac{\varphi}{2}} \end{bmatrix} \quad (2.38)$$

Note that there is a sign ambiguity in the above equation when it is used to extract quaternion components. Both these solutions are valid. Since in (2.35), it was proved that  $Q \sim -Q$ .

In other words, any orientation of one coordinate system relative to another can be described in terms of two different right-hand rotations. For instance, a right-hand rotation about  $x$  axis by 60 degrees is equivalent to a right-hand rotation of 300 degrees about  $-x$  axis.

#### 2.4.4 Relation Between Quaternion and Rotation Matrix

Using the equation (2.34) along with equations (2.20) and (2.33), any given arbitrary vector defined in the inertial frame can be expressed in the body-fixed coordinates by

$$\begin{bmatrix} u_{xB} \\ u_{yB} \\ u_{zB} \end{bmatrix} = \begin{bmatrix} q_0^2 + q_1^2 - q_2^2 - q_3^2 & 2(q_1q_2 + q_3q_0) & 2(q_1q_3 - q_2q_0) \\ 2(q_1q_2 - q_3q_0) & q_0^2 - q_1^2 + q_2^2 - q_3^2 & 2(q_2q_3 + q_1q_0) \\ 2(q_1q_3 + q_2q_0) & 2(q_2q_3 - q_1q_0) & q_0^2 - q_1^2 - q_2^2 + q_3^2 \end{bmatrix} \begin{bmatrix} u_{xI} \\ u_{yI} \\ u_{zI} \end{bmatrix} \quad (2.39)$$

Comparing equation (2.39) with equation (2.9), we can derive the relation between quaternion and corresponding rotation matrix as

$$R(q) = \begin{bmatrix} q_0^2 + q_1^2 - q_2^2 - q_3^2 & 2(q_1q_2 + q_3q_0) & 2(q_1q_3 - q_2q_0) \\ 2(q_1q_2 - q_3q_0) & q_0^2 - q_1^2 + q_2^2 - q_3^2 & 2(q_2q_3 + q_1q_0) \\ 2(q_1q_3 + q_2q_0) & 2(q_2q_3 - q_1q_0) & q_0^2 - q_1^2 - q_2^2 + q_3^2 \end{bmatrix} \quad (2.40)$$

Note that, the  $R(Q)$  can also be rewritten via the formula known as *Rodriguez formula*,

$$R(Q) = (q_0^2 + q^T q)I_3 + qq^T - 2q_0S(q) \quad (2.41)$$

where  $S(q)$  is the asymmetric matrix associated with the vector  $q$  and is given by

$$S(q) = \begin{bmatrix} 0 & -q_3 & q_2 \\ q_3 & 0 & -q_1 \\ -q_2 & q_1 & 0 \end{bmatrix}.$$

On the other hand, the quaternion can be extracted from direction cosine matrix as well. If we replace the left-side term of equation (2.39) by the right-side term of equation (2.9), we can write

$$\begin{bmatrix} R_{11} & R_{12} & R_{13} \\ R_{21} & R_{22} & R_{23} \\ R_{31} & R_{32} & R_{33} \end{bmatrix} = \begin{bmatrix} q_0^2 + q_1^2 - q_2^2 - q_3^2 & 2(q_1q_2 + q_3q_0) & 2(q_1q_3 - q_2q_0) \\ 2(q_1q_2 - q_3q_0) & q_0^2 - q_1^2 + q_2^2 - q_3^2 & 2(q_2q_3 + q_1q_0) \\ 2(q_1q_3 + q_2q_0) & 2(q_2q_3 - q_1q_0) & q_0^2 - q_1^2 - q_2^2 + q_3^2 \end{bmatrix} \quad (2.42)$$

Taking equation (2.34) into account, combination of diagonal components of two matrices in equation (2.42) provides three separate equations,

$$\begin{cases} R_{11} = 1 - 2(q_2^2 + q_3^2) \\ R_{22} = 1 - 2(q_1^2 + q_3^2) \\ R_{33} = 1 - 2(q_1^2 + q_2^2) \end{cases} \quad (2.43)$$

Using above equation leads to a four by four system of equations that relates the squares of the quaternion components to diagonal components of rotation matrix,

$$\begin{bmatrix} q_0^2 \\ q_1^2 \\ q_2^2 \\ q_3^2 \end{bmatrix} = \frac{1}{4} \begin{bmatrix} 1 + R_{11} + R_{22} + R_{33} \\ 1 + R_{11} - R_{22} - R_{33} \\ 1 - R_{11} + R_{22} - R_{33} \\ 1 - R_{11} - R_{22} + R_{33} \end{bmatrix} \quad (2.44)$$

Also, comparing non-diagonal components of two matrices in equation (2.42) provides another set of equations given by

$$\begin{bmatrix} q_0 q_1 \\ q_0 q_2 \\ q_0 q_3 \\ q_1 q_2 \\ q_1 q_3 \\ q_2 q_3 \end{bmatrix} = \frac{1}{4} \begin{bmatrix} R_{23} - R_{32} \\ R_{31} - R_{13} \\ R_{12} - R_{21} \\ R_{12} + R_{21} \\ R_{31} + R_{13} \\ R_{23} + R_{32} \end{bmatrix} \quad (2.45)$$

Using equation (2.44) along with equation (2.45), quaternion components can be calculated by the following formula as long as  $q_0 \neq 0$ .

$$\begin{aligned} q_0 &= \pm \frac{1}{2} (1 + R_{11} + R_{22} + R_{33})^{\frac{1}{2}} \\ q &= \frac{1}{4q_0} \begin{bmatrix} R_{23} - R_{32} \\ R_{31} - R_{13} \\ R_{12} - R_{21} \end{bmatrix} \end{aligned} \quad (2.46)$$

Two solutions expressed in this equation represent the same orientation regarding the fact proved in (2.35).

## Aerodynamic Study

Several excellent textbooks and academic papers have been published discussing the aerodynamics of helicopters, including [4], [22], [23] and [11] which the majority of this chapter is based on. In addition, there are some reviews such as [30] and [29] that use the same basic facts to cover more specific details about quadrotor aerodynamics. There are two theories commonly used to support the helicopter flight analysis: the momentum theory and the blade element theory. Both theories analyze the behavior of rotating propellers in the air and provide useful information and relations involved with important quantities like thrust and drag. These theories are discussed briefly in the following sections.

### 3.1 Momentum Theory Analysis

This theory was originally developed by Rankine in 1865 to analyze the behavior of marine propellers, but later on it was extended to spacecraft applications. Essentially, the momentum theory deals with the exchange of momentum between the rotating blades and the column of air which is being accelerated through the rotor. The motor power generates a torque applied to the rotor shaft, producing a thrust force.

The details of flow environment characteristics are not considered in momentum theory. When the fluid (air flow in this case) passes through the rotating propellers, it accelerates smoothly resulting in increase of the fluid velocity. Assuming airflow in the boundaries around the rotor to be one dimensional (only in vertical direction) and quasi-steady, a physical picture of hovering rotor can be drawn. Having this model in mind, the momentum theory discusses application of three basic conservation laws (conservation of mass, momentum, and energy) to the rotor and airflow.

As it is shown in the airflow model in figure (3.1), the airflow out of the rotor wake boundaries is considered to be relatively at rest. Plane  $P_0$

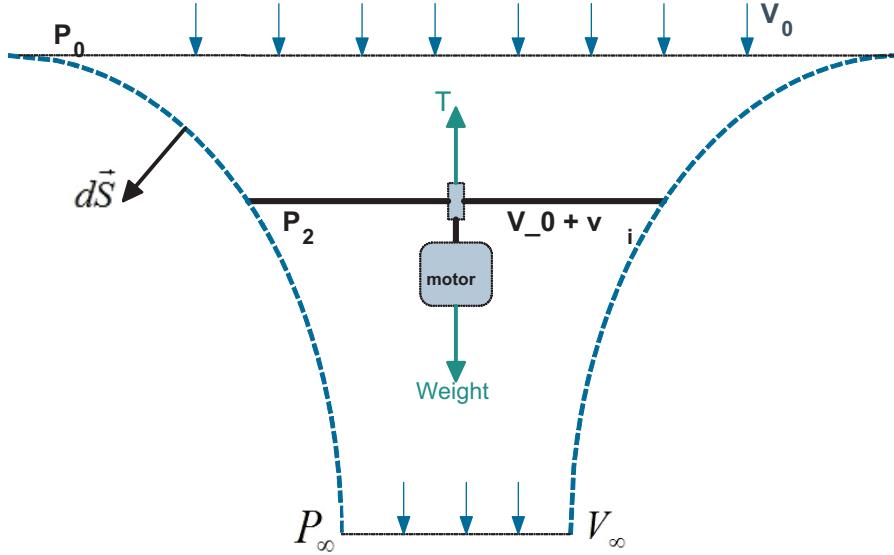


Figure 3.1: The Flow Model in Momentum Theory Analysis.

represents the far up boundary of rotor wake, while the plane  $P_\infty$  shows the far down boundary. The plane just below the rotor blades disc is named  $P_2$ . Recalling the fact that for the mass of air fluid entering the streamtube we have

$$m = \mathcal{J}\rho$$

where  $m$ ,  $\mathcal{J}$  and  $\rho$  denote mass, volume and density of the fluid respectively. Also, for the momentum of the fluid we have

$$n = m\mathcal{V},$$

where  $n$  and  $\mathcal{V}$  represent the momentum and local velocity of the fluid respectively.

Let  $S$  be the surface of the rotor wake. Considering the conservation laws of fluid mechanics, the mass flow into the rotor wake (volume) should be equal to the mass flow out of it. The conservation of fluid mass can be written as

$$\oiint_S \rho \vec{\mathcal{V}} \cdot d\vec{S} = 0, \quad (3.1)$$

where  $d\vec{S}$  denotes the normal area vector. The above equation illustrates the integration over the closed domain of imaginary streamtube. Similarly, the conservation of fluid momentum can be described as

$$\vec{F} = \oiint_S P d\vec{S} + \oiint_S (\rho \vec{\mathcal{V}} \cdot d\vec{S}) \vec{\mathcal{V}}. \quad (3.2)$$

where  $P$  represents the net pressure on the fluid. As it is clearly shown in equation (3.2), the momentum of a fluid system is a vector involving both direction and magnitude. It is the sum of momenta of individual particles. Assuming that the flow is unconstrained, one can conclude that  $P = 0$ . The force calculated in vector equation (3.2), is the reaction force corresponding to the thrust applied to the air column by the rotor. Taking Newton's third law into account, this force should be equal to the thrust but with an opposite direction. As a final step, momentum theory considers the conservation of energy in the flow stating that the work done by rotor on the flow is translated to the kinetic energy in the fluid. Conservation of energy in fluid is written as

$$w = \iint_S \frac{1}{2} (\rho \vec{V} \cdot d\vec{S}) |\vec{V}|^2. \quad (3.3)$$

### 3.1.1 Hovering Rotor Analysis

One of the most important flight regimes expected from a helicopter and more specifically a quadrotor, is the hovering condition. Hover is the unique flight condition in which the rotor doesn't have forward or vertical speed. As it was mentioned earlier, the preliminary assumptions consider the flow to be quasi-steady within the boundaries of the rotor wake. This means in time scale, the changes in boundary conditions are so slow that any inertia effects can be neglected, thus the flow velocity is time dependant. The mass flow rate is constant in the boundaries of rotor wake. Using equation (3.1), we can write

$$\dot{m} = \iint_{P_\infty} \rho \vec{V} \cdot d\vec{S} = \iint_{P_2} \rho \vec{V} \cdot d\vec{S} \quad (3.4)$$

As mentioned before, the flow velocity is time dependant, therefore the above equation can be solved as

$$\rho A_{P_\infty} \mathcal{V}_{inf} = \rho A_{P_2} \mathcal{V}_i \quad (3.5)$$

where  $A_{P_\infty}$  and  $A_{P_2}$  represent the area of rotor far wake and rotor disc respectively. Also,  $\mathcal{V}_i$  and  $\mathcal{V}_{inf}$  are considered as the induced velocities in rotor disc and rotor far wake respectively.

In the other hand, equation (3.2) can be rewritten as

$$\vec{F} = T = \iint_{P_\infty} \rho (\vec{V} \cdot d\vec{S}) \vec{V} - \iint_{P_0} \rho (\vec{V} \cdot d\vec{S}) \vec{V} \quad (3.6)$$

Considering  $\mathcal{V}_0 = 0$  in hovering condition, the thrust can be expressed using the above equation

$$T = \dot{m}\mathcal{V}_{inf}. \quad (3.7)$$

Recalling equation (3.3), the work done on the flow by the rotor can be described by

$$w = w_{P_\infty} - w_{P_0} = \iint_{P_\infty} \frac{1}{2}\rho(\vec{\mathcal{V}} \cdot d\vec{S})\vec{\mathcal{V}}^2 - \iint_{P_0} \frac{1}{2}\rho(\vec{\mathcal{V}} \cdot d\vec{S})\vec{\mathcal{V}}^2 \quad (3.8)$$

Also, the work done by the rotor can be calculated when the thrust and velocity of rotor disc are known

$$w = T\mathcal{V}_i \quad (3.9)$$

Note that by considering that in hovering condition  $\mathcal{V}_0 = 0$ , combination of equations (3.8) and (3.9) results in finding an expression for thrust in terms of rotor disc characteristics and the induced velocity in its plane. Such an expression is given by

$$T = 2\rho A\mathcal{V}_i^2 \quad (3.10)$$

where  $A$  is representing the rotor disc surface. This equation can be rearranged to find the required induced velocity when the desired thrust is given

$$\mathcal{V}_i = \sqrt{\frac{T}{2\rho A}} \quad (3.11)$$

Therefore, the required power for the desired given thrust in hovering condition can be calculated as

$$P = T\mathcal{V}_i = \frac{T^{\frac{3}{2}}}{\sqrt{2\rho A}} \quad (3.12)$$

Since the angular velocity of rotor can be measured in applications, finding a relationship between angular velocity and induced velocity can help for further modelings. Such a relation is made possible with introducing *Induced Inflow Ratio*,  $\lambda$ .

$$\mathcal{V}_i = \lambda\omega r \quad (3.13)$$

where  $\omega$  represents the angular velocity of the rotor while  $r$  represents the radius of the rotor blade disc. A simple substitution of equation (3.13) in equation (3.10) confirms that the thrust in hovering condition is related to the squared angular velocity of the rotor, proportionally.

$$T = 2\rho A\lambda^2 r^2 \omega^2 \quad (3.14)$$

### 3.1.2 Axial Movement (Climb and Descend) analysis

Considering the flow model shown in figure (3.1), the momentum theory can be used to analyze the axial flight regimes as well. In climbing regime, the rotor is ascending with a non-zero velocity  $\mathcal{V}_c$ . Therefore, the up far wake velocity is  $\mathcal{V}_0 = \mathcal{V}_c$ . similarly the velocity in blade plane and plane in the far down wake of rotor are given as

$$\mathcal{V}_2 = \mathcal{V}_i + \mathcal{V}_c$$

$$\mathcal{V}_\infty = \mathcal{V}_c + \mathcal{V}_{inf}$$

Considering the above expressions in combination with mass conservation described in equation (3.1), we can write

$$\dot{m} = \rho A_\infty (\mathcal{V}_c + \mathcal{V}_{inf}) = \rho A (\mathcal{V}_c + \mathcal{V}_i) \quad (3.15)$$

Similarly, momentum conservation expressed in equation (3.2) leads to

$$T = \dot{m}(\mathcal{V}_c + \mathcal{V}_{inf}) - \dot{m}\mathcal{V}_c = \dot{m}\mathcal{V}_{inf} \quad (3.16)$$

If we rewrite energy conservation in equation (3.3) for climbing conditions, we have

$$w = T(\mathcal{V}_0 + \mathcal{V}_i) = \frac{1}{2}\dot{m}\mathcal{V}_\infty^2 - \frac{1}{2}\dot{m}\mathcal{V}_0^2 = \frac{1}{2}\dot{m}\mathcal{V}_{inf}(2\mathcal{V}_c + \mathcal{V}_{inf}) \quad (3.17)$$

Combination of last two equations followed by a simple division by the term  $2\rho A$  results in

$$\frac{T}{2\rho A} = (\mathcal{V}_c + \mathcal{V}_i)\mathcal{V}_i \quad (3.18)$$

If we compare the above equation with the induced velocity expression in hovering flight shown in equation (3.11), a relation could be found between the induced velocities in hovering and climbing regimes. Such relation is described as

$$\frac{\mathcal{V}_i}{\mathcal{V}_h} = -\left(\frac{\mathcal{V}_c}{2\mathcal{V}_h}\right) + \sqrt{\left(\frac{\mathcal{V}_c}{2\mathcal{V}_h}\right)^2 + 1} \quad (3.19)$$

Considering  $\mathcal{V}_c$  to be negative, the same approach is used to analyze the descending flight leading to a relation between the induced velocities in hovering and descending conditions which is expressed as

$$\frac{\mathcal{V}_i}{\mathcal{V}_h} = -\left(\frac{\mathcal{V}_c}{2\mathcal{V}_h}\right) - \sqrt{\left(\frac{\mathcal{V}_c}{2\mathcal{V}_h}\right)^2 - 1} \quad (3.20)$$

An important issue to point out is that in practice, when the rotor starts to descend two flow directions are possible. This violates the preliminary assumption for the flow model drawn in figure (3.1), stating that the flow is one-dimensional. In such a condition, it's not possible to define the rotor wake boundaries, therefore, this analysis is not valid in the region. However by assuming  $|\mathcal{V}_c| > 2\mathcal{V}_h$  equation (3.20) can be used.

It must be noted that this analysis is based on ideal conditions and assumptions, in practice, friction and viscous losses could not be neglected. The boundaries and inflow conditions are not accurately specified in momentum theory analysis, in the other hand the effects of rotor blades pitch and angle of attack are not studied in this analysis. This is exactly where the rotor blade theory is used to address the role of propellers in aerodynamic analysis.

Although the momentum theory has been often used to model the thrust in quadrotor system (for instance in [16]), but a more accurate study on the role of rotor blades and their shape in aerodynamic forces could result in a better design of propellers and better overall performance. Such a review for quadrotor models has been considered for instance in [29] using rotor blade theory.

## 3.2 Rotor Blade Element Theory Analysis

The blade element theory was first introduced by Drwiecki and later on, it was extended by several other researchers. In this theory the propeller is considered as a propulsion machine which consists of aerodynamically independent narrow elements. Each element can be analyzed as a two dimensional airfoil producing aerodynamic forces. Integration of these sectional forces could result in rotor performance analysis.

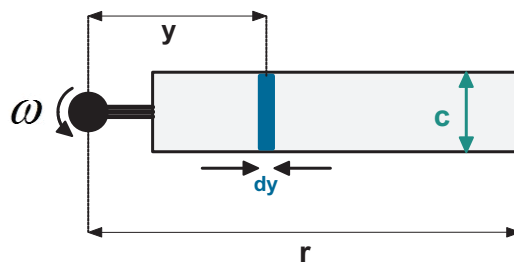


Figure 3.2: The Blade Model for Rotor Blade Element Theory.

As it is clear in the above figure,  $y$  represents the distance of each element from the rotation center. When the propeller moves, it is subject to several

components of fluid velocity. One of these components is the axial velocity  $\mathcal{V}_c$  due to vertical movement of the system. The velocity due to rotation of blade  $\omega r$  and induced velocity  $\mathcal{V}_i$  are the other two components, which are the result of rotation of propeller and disturbance of fluid by propeller respectively. Note that blade element speed due to rotation, varies over the blade span, because the distance traveled by each blade element depends on its distance from rotation center. For instance, the blade speed near the rotor shaft is smaller than the speed at the tip of the blade.

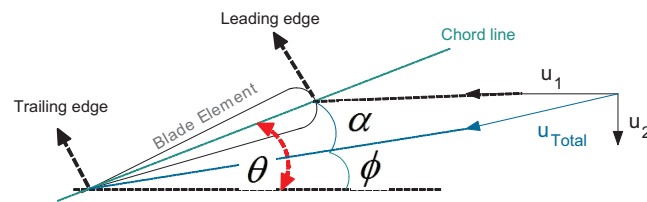


Figure 3.3: Aerodynamic of Blade Element.

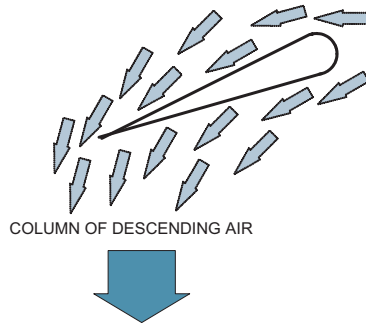


Figure 3.4: Induced Airflow Around the Blade.

As it is shown in figure (3.3), the chord  $c$  is defined as the length of the blade from leading edge to trailing edge. The angle of attack  $\alpha$  is an aerodynamic angle which is illustrated as the angle between the blade element chord and the resultant velocity seen by the airfoil. Another angle shown in figure (3.3) is the pitch angle of the blade  $\theta$ , which is rather a mechanical angle and is defined as the angle between the chord and the plane of rotation (system airframe). The total air velocity seen by the blade  $u_{Total}$  has two components  $u_1$  and  $u_2$ . A simple geometric calculation confirms

$$u_{Total} = \sqrt{u_1^2 + u_2^2},$$

$$\phi = \tan^{-1} \frac{u_2}{u_1},$$

and

$$\alpha = \theta - \phi.$$

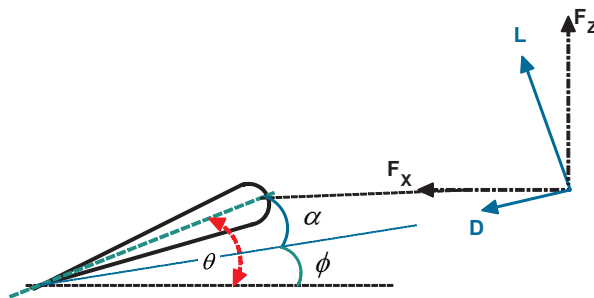


Figure 3.5: Aerodynamic Forces Applied to Blade Element.

The airflow applies lift  $L$  and drag  $D$  forces to the blade element which are perpendicular and parallel to the resultant velocity respectively. Therefore, one can write

$$L = \frac{1}{2}\rho u_T^2 c c_l \quad (3.21)$$

$$D = \frac{1}{2}\rho u_T^2 c c_d \quad (3.22)$$

where  $c_l$  and  $c_d$  are functions of the angle of attack,  $\theta$ .

As it is clearly shown in figure (3.5),  $F_x$  and  $F_z$  represent the total aerodynamic force components parallel to and perpendicular to the rotor blade disc respectively. These components are easily calculated as

$$F_x = L \cos \phi - D \sin \phi \quad (3.23)$$

$$F_z = L \sin \phi + D \cos \phi \quad (3.24)$$

Ideally, the vertical component  $F_z$  should be equal to the thrust. Thus,

$$dT = N F_z dy \quad (3.25)$$

$$dQ = N F_x y dy \quad (3.26)$$

where  $N$  is the number of blades. Using equation (3.26), we can write the following equation for the sectional power

$$dP = \omega dQ = N F \omega y dy \quad (3.27)$$

Having the thrust, torque and power for each blade element, integration of this quantities over the blade span leads to finding the total thrust, torque and power for the rotor blades.

In hovering and vertical flight, the vertical component of the velocity seen by the blade element is  $u_2 = V_c + \mathcal{V}_i$ . In the other hand,  $u_1 = \omega y$  due to rotational velocity of the blade element. Therefore, the *Inflow Ratio* can be defined as

$$\lambda = \frac{\mathcal{V}_c + \mathcal{V}_i}{\omega r} \quad (3.28)$$

Recalling that  $\tan^{-1} \phi = \frac{u_2}{u_1}$ , one can write

$$\tan^{-1} \frac{u_2}{u_1} = \tan^{-1} \frac{\mathcal{V}_c + \mathcal{V}_i}{\omega y} = \lambda \left( \frac{y}{r} \right) \quad (3.29)$$

In practice, the inflow ratio has been proved to be very small when the loading is small. The assumption of  $\lambda$  being small makes it possible to write

$$\phi \simeq \tan \phi \simeq \sin \phi$$

$$\cos \phi \simeq 1$$

which leads to

$$u_{Total} \simeq u_1. \quad (3.30)$$

If we assume that the lift coefficient  $c_l$  is linearly relative to the attack angle, *i.e.*,  $c_l = a\alpha$ , Then equations (3.21), (3.25) and (3.26) can be rewritten as

$$L = \frac{1}{2} \rho u_1^2 c a \left( \theta - \frac{u_2}{u_1} \right) \quad (3.31)$$

$$dT = NL dy \quad (3.32)$$

$$dQ = NL(\phi + D)r dr \quad (3.33)$$

Normalization of sectional thrust (shown in equation (3.32)) with respect to air density, rotational velocity and blade radius helps to find a dimensionless thrust coefficient for each blade element. Such a coefficient is given by

$$dC_T = \frac{\sigma a}{2} (\theta u_1^2 - u_1 u_2) dy = \frac{\sigma a}{2} (\theta y^2 - \lambda y) dy \quad (3.34)$$

where  $\sigma$  is the *Solidity Ratio* defined as  $\sigma = \frac{Nc}{\pi r}$ . Similarly, to find a dimensionless torque or power coefficient for blade elements, equations (3.33) and (3.27) can be normalized with respect to air density, rotational velocity and blade radius. The equation defining the torque or power coefficient is given by

$$dC_P = dC_Q = \left( \frac{\sigma a}{2} (\theta y \lambda - \lambda^2) + \frac{\sigma c_d}{2} y^2 \right) y dy \quad (3.35)$$

As mentioned earlier, integration of thrust coefficients of blade elements results in finding the coefficients of total thrust.

$$C_T = \int_0^1 \frac{\sigma a}{2} (\theta y^2 - \lambda y) dy \quad (3.36)$$

Assuming that the chord is constant and the twist is ideally linear while considering uniform inflow, equation (3.36) can be simplified as

$$C_T = \frac{\sigma a}{2} \left( \frac{\theta_{.75}}{3} - \frac{\lambda}{2} \right). \quad (3.37)$$

With similar assumptions (considering the constant chord and uniform induced velocity along the span), the power coefficient for each blade element can be rewritten as

$$dC_P = \lambda dC_T + \frac{\sigma c_d}{2} y^3 dy \quad (3.38)$$

Therefore, the power coefficient for the blade can be calculated by integration

$$C_P = \int \lambda dC_T + \int_0^1 \frac{\sigma c_d}{2} y^3 dy \quad (3.39)$$

The first term in above equation shows the induced power loss, recalling that  $dP_i = (\mathcal{V}_c + \mathcal{V}_i)dT$ . The induced power loss varies with changes in the induced angle of attack  $\phi$ . As it's assumed that the induced velocity is uniform over the span, one can conclude

$$C_{P_i} = \lambda C_T. \quad (3.40)$$

The second term in equation (3.40) represents the profile power loss as a result of drag forces on the blade. If we assume that the drag coefficient  $c_d$  is constant, the integral equation can be solved leading to

$$C_{P_o} = \frac{\sigma c_d}{8} \quad (3.41)$$

where  $C_{P_o}$  represents the profile power loss. Hence, the ideal total power coefficient of the rotor is given by

$$C_P = C_{P_i} + C_{P_o} = \lambda C_T + \frac{\sigma c_d}{8}. \quad (3.42)$$

Note that this is the ideal case analysis. In practice, the induced power loss is greater than what is calculated in ideal case. The induced power loss can be calculated more accurately considering the actual induced velocity distribution along the blade span. Also, a more accurate profile power loss calculation is possible, if we consider the drag coefficient to be a function of the angle of attack and march number.

# Quadrotor Concept

The quadrotor aerial robot under consideration, is an aircraft with four lift generating propellers rigidly mounted at equal distances from each other in a cross configuration. Each propeller is connected to a motor through a reduction gear.

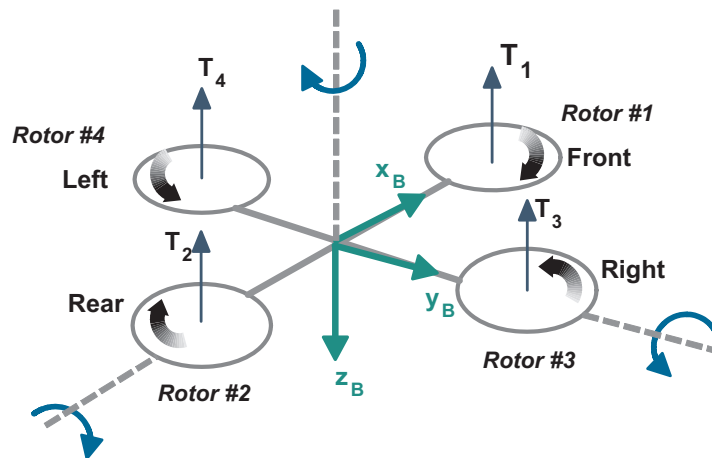


Figure 4.1: A quadrotor structure.

As it is shown in figure (4.1), the pair of rotors on one axis rotate clockwise, while the other pair on the perpendicular axis spin counter clockwise. This special configuration reduces the complexity of mechanical analysis and eliminates the need for a tail rotor as in a conventional helicopter.

In a four-rotor aerial robot, different flight regimes are achieved by changing the rotors thrusts. As fixed-pitch rotor blades are used in the quadrotor aircraft, the motion of the aircraft can be controlled by changing the angular velocity of the rotors. Some important possible movements are listed and discussed briefly in this section.

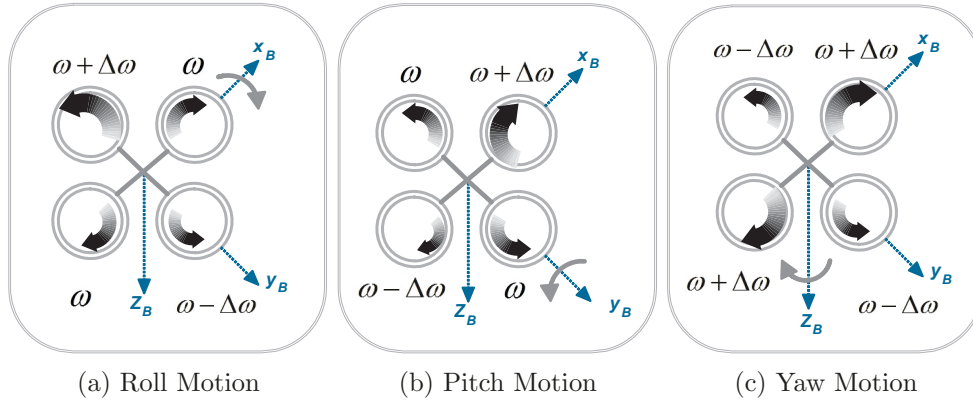


Figure 4.2: Quadrotor Motion.

- **Hovering** is achieved when the four rotors rotate with the same angular velocity  $\omega$  generating the total force to counterbalance the force due to the gravitational acceleration.
- **Roll** motion is achieved by increasing (decreasing) angular speed of the right rotor and decreasing (increasing) that of the left rotor. In such condition, if the total thrust is managed to remain unchanged (as it is shown in figure (4.2-a)), the quadrotor aircraft moves to the right (left).
- **Pitch** motion is achieved by increasing (decreasing) the front rotor speed and decreasing (increasing) that of the rear rotor. If the total thrust is managed to remain unchanged (as it is shown in figure (4.2-b)), the aircraft moves forward (backward).
- **Yaw** motion is achieved by increasing (decreasing) the angular velocity of front-rear rotors speeds and decreasing (or increasing) that of right-left rotors. The aircraft starts to spin around its  $z$  axis clockwise (counter clockwise), if the total thrust is kept unchanged (as it is shown in figure (4.2-c)).

- **Vertical Flight** is achieved by increasing (decreasing) the angular velocity of each rotor by the same proportion. In a consequence, the total thrust is increased (decreased) leading the aircraft to ascend (descend).

## 4.1 Modeling a Quadrotor Aircraft

The preliminary step in design of any model-based control system is considered to be the development of a mathematical model of the system based on known physical principles. In better words, the model of a system uncovers the philosophy behind the behavior of the system as well as the requirements to control it in desired way.

In recent years, the miniature size quadrotor aircraft has been widely used by academic research teams as a test-bed to evaluate the new control schemes. Modeling the aircraft is the crucial requirement to design the appropriate controllers. Such a model has been investigated in details and published for instance in [40], [36], [31] and [16]. Mostly, for developing a mathematical model of a quadrotor aircraft, the kinematics of motion are studied along with the Newton-Euler formulations to describe the dynamic relations in the system. The following section proceeds by a brief study of kinematics of aircraft motion followed by the dynamic model of the quadrotor aircraft.

### 4.1.1 Modeling the Kinematics of an aircraft

Through the kinematic analysis of the quadrotor aircraft, the motion of a rigid body is described in terms of vectors in three dimensional space, without detailed analysis of the mechanisms which cause the motion. As it was mentioned in earlier chapters, to describe the motion of a rigid body in space, two frames of reference need to be defined.

- **Inertial frame**  $\{I\}$  is defined as the right-hand fixed coordinate system. While the origin of the inertial frame is fixed at the home location on the Earth,  $x_I$ ,  $y_I$  and  $z_I$  are unit vectors pointing to north, east and downward directions. These three unit vectors form the Earth inertial frame together. The linear and angular position of the aircraft are usually expressed with respect to this frame.
- **Body-fixed frame**  $\{B\}$  is attached to the quadrotor airframe while its origin is located at the center of mass of the aircraft. Since the center of mass of the quadrotor usually coincides with the center of its cross configuration, the unit vectors  $x_B$ ,  $y_B$  and  $z_B$  point toward front-side, right-side and downward the airframe respectively.

Essentially, two kinds of motions can be described: translational motion and rotational motion. Considering the displacement of the center of mass of the aircraft with respect to the inertial frame, it is possible to explore translational kinematic equation.

Let  $p$  denote the vector describing the displacement of the center of mass of the aircraft in the inertial frame.

$$p = \begin{bmatrix} p_x \\ p_y \\ p_z \end{bmatrix}.$$

If we assume the aircraft to move with the linear velocity  $v$ , recalling the basic definition of velocity we can write

$$\dot{p} = v \quad (4.1)$$

The above equation is called *translational kinematic equation* and can be used to calculate the change in the aircraft position when the velocity of the aircraft is measured by a GPS device for instance. It is clear that displacement and velocity are expressed with respect to the inertial frame here.

### Direction Cosine Formulation

When an aircraft is undergoing a rotation, its orientation varies with the time. Therefore, the elements of the rotation matrix representing the attitude are functions of time, making it possible to write nine differential equations from the rotation matrix elements. The resultant nine differential equations known as *Poisson's kinematic equations* are given by [32]

$$\begin{bmatrix} \dot{R}_{11} & \dot{R}_{12} & \dot{R}_{13} \\ \dot{R}_{21} & \dot{R}_{22} & \dot{R}_{23} \\ \dot{R}_{31} & \dot{R}_{32} & \dot{R}_{33} \end{bmatrix} = \begin{bmatrix} 0 & \Omega_z & -\Omega_y \\ -\Omega_z & 0 & \Omega_x \\ \Omega_y & -\Omega_x & 0 \end{bmatrix} \begin{bmatrix} R_{11} & R_{12} & R_{13} \\ R_{21} & R_{22} & R_{23} \\ R_{31} & R_{32} & R_{33} \end{bmatrix} \quad (4.2)$$

which can be summarized as

$$\dot{R} = RS(\Omega) \quad (4.3)$$

where  $\Omega = [\Omega_x, \Omega_y, \Omega_z]^T$  is the angular velocity and  $S(\Omega)$  denotes the skew symmetric matrix associated to  $\Omega$  such that for any vector  $u \in \mathbb{R}^3$ , one can write  $S(\Omega)u = \Omega \times u$ .

Using the kinematic equation in terms of rotation matrix avoids any singularity. However, as a compromise, it is time consuming since nine equations must be integrated to update the orientation with the time.

### Quaternion Formulation

Recalling the quaternion formulation of orientation described in chapter 2, we have

$$\begin{pmatrix} \dot{q}_0 \\ \dot{q}_1 \\ \dot{q}_2 \\ \dot{q}_3 \end{pmatrix} = \begin{pmatrix} \frac{d}{dt}(\cos \frac{\Theta}{2}) \\ \frac{d}{dt}(E_x \sin \frac{\Theta}{2}) \\ \frac{d}{dt}(E_y \sin \frac{\Theta}{2}) \\ \frac{d}{dt}(E_z \sin \frac{\Theta}{2}) \end{pmatrix} = \begin{pmatrix} -\sin \frac{\Theta}{2} \\ E_x \cos \frac{\Theta}{2} \\ E_y \cos \frac{\Theta}{2} \\ E_z \cos \frac{\Theta}{2} \end{pmatrix} \frac{\dot{\Theta}}{2} + \begin{pmatrix} 0 \\ \dot{E}_x \sin \frac{\Theta}{2} \\ \dot{E}_y \sin \frac{\Theta}{2} \\ \dot{E}_z \sin \frac{\Theta}{2} \end{pmatrix}. \quad (4.4)$$

According to [32], the derivative of Euler axis formulation is given by

$$\begin{pmatrix} \dot{\Theta} \\ \dot{E}_x \\ \dot{E}_y \\ \dot{E}_z \end{pmatrix} = \frac{1}{2} \begin{pmatrix} 2E_x & 2E_y & 2E_z \\ \dot{E}_{xx} + \frac{c_\epsilon}{s_\epsilon} & \dot{E}_{xy} - E_z & \dot{E}_{xz} + E_y \\ \dot{E}_{xz} - E_y & \dot{E}_{yz} + E_x & \dot{E}_{zz} + \frac{c_\epsilon}{s_\epsilon} \end{pmatrix}$$

where  $c_\epsilon$  and  $s_\epsilon$  are abbreviated forms of the functions  $\cos \frac{\Theta}{2}$  and  $\sin \frac{\Theta}{2}$  respectively. Also,  $\dot{E}_{ij} = -E_i E_j \frac{c_\epsilon}{s_\epsilon}$ .

Substitution of the derivative of the Euler's axis formula in equation (4.4) results in

$$\begin{pmatrix} \dot{q}_0 \\ \dot{q}_1 \\ \dot{q}_2 \\ \dot{q}_3 \end{pmatrix} = \frac{1}{2} \begin{bmatrix} -E_x \sin \frac{\Theta}{2} & -E_y \sin \frac{\Theta}{2} & -E_z \sin \frac{\Theta}{2} \\ \cos \frac{\Theta}{2} & -E_z \sin \frac{\Theta}{2} & E_y \sin \frac{\Theta}{2} \\ E_z \sin \frac{\Theta}{2} & \cos \frac{\Theta}{2} & -E_x \sin \frac{\Theta}{2} \\ -E_y \sin \frac{\Theta}{2} & E_x \sin \frac{\Theta}{2} & \cos \frac{\Theta}{2} \end{bmatrix} \begin{pmatrix} \Omega_x \\ \Omega_y \\ \Omega_z \end{pmatrix}. \quad (4.5)$$

This equation can be easily simplified as

$$\begin{pmatrix} \dot{q}_0 \\ \dot{q}_1 \\ \dot{q}_2 \\ \dot{q}_3 \end{pmatrix} = \frac{1}{2} \begin{bmatrix} -q_1 & -q_2 & -q_3 \\ q_0 & -q_3 & q_2 \\ q_3 & q_0 & -q_1 \\ -q_2 & q_1 & q_0 \end{bmatrix} \begin{pmatrix} \Omega_x \\ \Omega_y \\ \Omega_z \end{pmatrix}. \quad (4.6)$$

A glance at the above equation confirms that, the quaternion form of the rotational kinematic equation is singularity-free. Also, as it has been presented in [40], [25], the quaternion representation of kinematic equation can be rewritten as

$$\dot{Q} = \frac{1}{2} Q * \bar{\Omega} \quad (4.7)$$

where  $\bar{\Omega} = \begin{pmatrix} 0 \\ \Omega \end{pmatrix}$  and “\*” denote the quaternion multiplication operation.

The above form of kinematic equation has been used through this project for modeling the quadrotor rotational kinematics.

### 4.1.2 Dynamical Model

Through the analysis of quadrotor aircraft dynamics, the forces and torques which cause the motion are studied. The Newton laws are the most important part of classical mechanics which can be applied to the system making it possible to derive the dynamic equations of a quadrotor aircraft.

Let  $F$  represent the total force affecting the aircraft in inertial frame. Classical Newton's law can be written as

$$F = M \frac{dv}{dt} \quad (4.8)$$

where  $M$  and  $v$  denote the total mass and linear velocity of the aircraft respectively. Also,  $\frac{d}{dt}$  represents the time derivative in the inertial frame. On the other hand, Euler's axiom of the Newton's second law indicates

$$\tau = I_f \frac{d\Omega_I}{dt} \quad (4.9)$$

where  $\tau$  denotes the total torque acting on the aircraft and  $I_f$  represents the body inertia matrix. Note that, Newton's law holds for inertial frame. However, in some cases it is more convenient to write the relations and equations in the non-inertial frame. In quadrotor case specifically, using the body-fixed notations, one can take the advantage of quadrotor symmetrical design configuration to simplify the equations involved with the forces. In addition, the sensors are strapped on the assumed center of mass of the quadrotor which means the measurements are taken in body frame as well. Hence, it is useful to express equation (4.8) and (4.9) in the body-fixed frame. Taking the coriolis effect into account, we can write Newton's law regarding non-inertial frame,

$$M\dot{v}_B = M\Omega \times v + F \quad (4.10)$$

where  $F$  and  $v_B$  represent the total force applied to the aircraft and linear velocity in body-fixed frame respectively. The corresponding Euler axiom reveals

$$I_f \dot{\Omega} = -\Omega \times I_f \Omega + \tau_B. \quad (4.11)$$

where  $\tau_B$  is the total torque acting on the vehicle expressed in the body frame. Since the structure is symmetrical with respect to the center of mass, one can conclude that  $I_f$  is a diagonal inertia matrix.

Combination of the last two equations leads to deriving the *dynamic equations* of a quadrotor aircraft, as far as an accurate knowledge of forces and torques acting on the aircraft is provided.

### Forces

The forces acting on the quadrotor airframe can be divided in three categories: aerodynamic drag forces, the force due to Earth gravity (weight force) and the thrust. As discussed in the previous chapter, the thrust component is perpendicular to the blade path (hence, it is perpendicular to the blade plane) while the drag force is opposite the direction of blade linear velocity (thus, it is parallel to the blade plane). On the other hand, the weight force always points to the Earth while it has a constant value  $Mg$ , where  $g$  indicates the gravitational acceleration.

If we assume the drag forces acting on the blades to be negligible, as it was

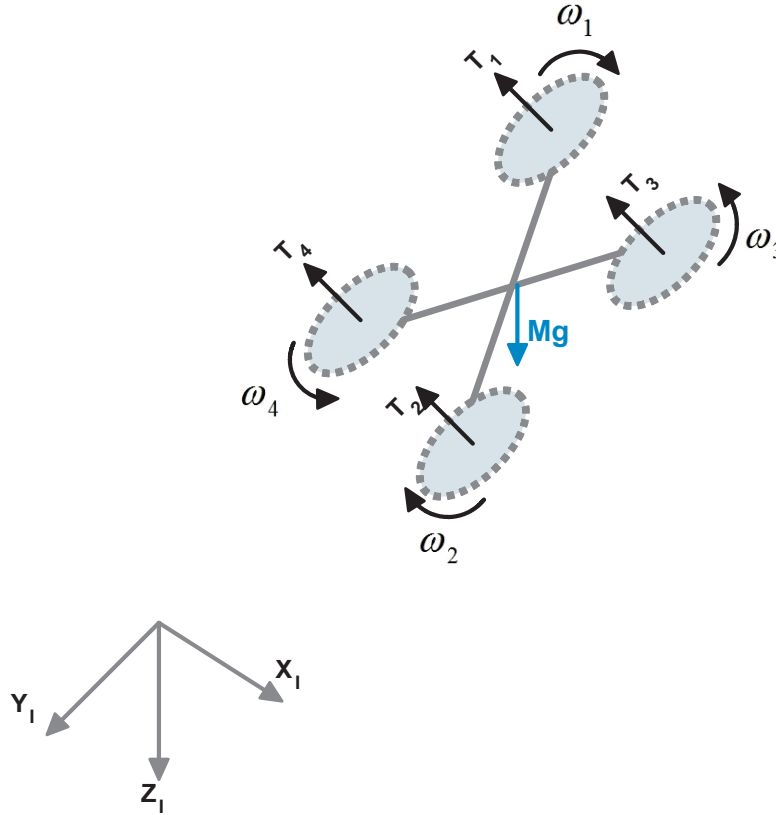


Figure 4.3: Forces Acting on a Quadrotor.

discussed in the previous chapter, for the thrust generated by each rotor we have

$$T_i = b\omega_i^2, \quad i \in \{1, 2, 3, 4\} \quad (4.12)$$

where  $\omega_i$  denotes the angular velocity of each rotor and  $b = 2\rho A\lambda^2 r^2$ . Note that,  $b$  is defined as a coefficient dependant on the physical characteristics of

the blades (including shape, pitch angle, etc.) as well as the airflow density around the blades. Here, the rotor blades and airflow are assumed to have the same characteristics, since identical devices have been used. Also, it is necessary to remind that fixed-pitch blades are used in quadrotor robot structure, thus, the generated thrust by each rotor changes with variation of the squared angular velocity proportionally. Drawing free body diagram for the system, one could easily conclude that the total thrust applied to the airframe by the rotors is given by

$$T = \sum_{i=1}^4 T_i = b \sum_{i=1}^4 \omega_i^2. \quad i \in \{1, 2, 3, 4\} \quad (4.13)$$

A glance at the equation (4.13) confirms that the thrust can be controlled by changing the angular velocity of the rotors in a quadrotor aerial robot. Recalling Newton's second law for inertial frame expressed in equation (4.8), one can write

$$F = Ma_I = Mgz_I - TRz_I \quad (4.14)$$

where  $a_I$  denotes the acceleration of the object expressed in inertial frame. From the above equation, it can be easily concluded that

$$a_I = \dot{v} = gz_I - \frac{1}{M}TRz_I \quad (4.15)$$

where  $z_I = \begin{pmatrix} 0 \\ 0 \\ 1 \end{pmatrix}$  and  $z_B$  are the unit vectors of inertial frame and body-fixed frame respectively.

### Torques

The main torques acting on a quadrotor airframe can be categorized as

- The torque applied by the rotors about the axes of the airframe,  $\tau_a$ . Recalling the relation between the force and the corresponding torque, one can write

$$\begin{aligned} \tau_a^1 &= d(T_4 - T_3) = db(\omega_4^2 - \omega_3^2) \\ \tau_a^2 &= d(T_1 - T_2) = db(\omega_1^2 - \omega_2^2) \\ \tau_a^3 &= k(T_1 + T_2 - T_3 - T_4) = k(\omega_1^2 + \omega_2^2 - \omega_3^2 - \omega_4^2) \end{aligned} \quad (4.16)$$

where  $d$  represents the distance between the center of mass of the airframe and the rotor center.  $\tau_a = \begin{pmatrix} \tau_a^1 \\ \tau_a^2 \\ \tau_a^3 \end{pmatrix}$  denotes the torque applied by the rotors about the origin of the body frame. Also,  $k$  denotes the proportionality constant dependant on the physical characteristics of the blades and airflow.

- The Gyroscopic torques applied to the airframe,  $G_a$ . Note that, the rotors are rigidly mounted on the body frame (which can rotate freely), while each rotor is spinning itself. This makes the rotors to act similar to a gyroscope in creating the torque given by [40]

$$G_a = I_r(\Omega \times z_I)(\omega_1 + \omega_2 - \omega_3 - \omega_4) \quad (4.17)$$

where  $I_r$  denotes the constant momentum inertia of the rotor.

Hence, Newton's law of motion expressed in equation (4.11) can be rewritten for the quadrotor aircraft as

$$I_f \dot{\Omega} = -\Omega \times I_f \Omega - G_a + \tau_a. \quad (4.18)$$

### Dynamic Model of Rotors

The dynamic equation of each rotor can be expressed as [40]

$$I_r \dot{\omega}_i = \tau_i - Q_i, \quad \omega_i \in \{1, 2, 3, 4\} \quad (4.19)$$

where  $I_r$  denotes the moment of inertia of each rotor.  $\omega_i, \tau_i$  and  $Q_i$  represent the angular velocity, rotor torque and reactive torque generated by each rotor respectively. As discussed earlier, the reactive torque applied by the rotor on the airflow due to the aerodynamic drag, depends mainly on the blade physical factors and is related to the squared angular velocity of the rotor proportionally. Such relation is given by

$$Q_i = k\omega_i^2. \quad (4.20)$$

where  $k$  is the proportionality constant.

### 4.1.3 Quadrotor Model

A mathematical model of the quadrotor aircraft can be developed by a comprehensive study on the kinematics and dynamics of the system. The resul-

tant model is presented by [40]

$$\begin{cases} \dot{p} = v \\ \dot{v} = gz_I - \frac{1}{M}TRz_I \\ \dot{R} = RS(\Omega) \\ I_f \dot{\Omega} = -\Omega \times I_f \Omega - G_a + \tau_a \\ I_r \dot{\omega}_i = \tau_i - Q_i, \quad i \in \{1, 2, 3, 4\} \end{cases} \quad (4.21)$$

## Attitude Estimation

The fundamental challenge to achieve autonomous stable flight for any unmanned aerial vehicle, is the accurate attitude estimation. In theory, orientation estimation of a rigid body can be provided by the integration of well-known kinematic model of the moving object as far as the angular velocity is measured precisely. There are a number of publications in literature that investigate the design of attitude stabilization schemes for UAVs, assuming that the angular velocity of the aircraft is measured accurately. However, in practice, the gyro sensors used for the measurement of angular velocity, are not flawless. There are biases and misalignments involved with gyro measurements. Thus, the attitude estimation is not practically reliable when the dynamic model of the system is used only along with gyro measurements. Over the past few years, attitude estimation of rigid bodies has received excessive attention in the academic control and navigation community. A common approach used for attitude estimation, is fusing at least two non-collinear inertial measurements taken on body frame of the the object along with the angular velocity. Accelerometers and magnetometers are the sensor units widely used to serve this purpose.

A typical challenge in most of control engineering applications involving signals and measurements is filtering the noise out of the signals. More specifically for the attitude estimation problem, different nonlinear filtering techniques have been used by researchers (see reference [12]). The Extended Kalman Filtering (EKF) is one of the oldest methods in this case proved to be practical. However, the complex mathematics which is the back bone of EKF attitude estimation methods highlights the demand for an easier and more understandable practical approach to the problem. The complementary filtering algorithm presented in [33] leads to a more simple and yet practical attitude observer. In this method, the gyroscope bias is considered to be constant while the gyro measurements are affected by the noise in low frequencies. When the acceleration of the vehicle is negligible, an estimation algorithm is introduced by fusing measurements of gyros with those of

accelerometers and magnetometers which are more reliable in low frequencies. At high frequencies, the observer reading mainly relies on the angular velocity while on the other hand, it mostly relies on the accelerometer and magnetometer measurements at low frequencies.

Through this project, two estimation algorithms have been implemented based on the observers presented in [41]. In the following sections, these algorithms are discussed briefly followed by the required measurement description and calibration discussion presented in the final section of this chapter.

## 5.1 Estimation Algorithms

Due to certain advantages of quaternion attitude representation over the other common formulations, this type of notation is used in [41] to derive the estimation algorithms. Consider the well-known rotational kinematics of the rigid body

$$\begin{cases} \dot{Q} = \frac{1}{2}Q * \bar{\Omega}, \\ I_f \dot{\Omega} = -\Omega \times I_f \Omega + \tau \end{cases} \quad (5.1)$$

where  $\bar{\Omega} = \begin{pmatrix} 0 \\ \Omega \end{pmatrix}$ . As it was discussed in Chapter 2, any vector in inertial frame  $u_I$ , can be expressed in body frame by

$$u_B = Q^{-1} * u_I * Q \quad (5.2)$$

Consider 3-axis accelerometer and magnetometer strapped down on the body of the aircraft. While the acceleration of the aircraft is assumed to be negligible, the accelerometer measures merely the projection of the gravitational acceleration in the body-fixed frame. In better words,

$$b_1 = R e_1 = Q^{-1} * \bar{e}_1 * Q$$

where  $b_1$  denotes the vector measurement obtained from the accelerometer. Also,  $e_1$  represents the value of gravitational acceleration in the inertial frame. Since such value is known in any location on the Earth, we can easily conclude that

$$e_1 = a_g$$

where  $a_g$  represents the gravitational acceleration vector in the inertial frame. Similarly, when no external magnetic field is present in the surrounding environment of a the body frame, the magnetometer measures only the projection of the Earth magnetic field in body-frame. Therefore,

$$b_2 = R e_2 = Q^{-1} * \bar{e}_1 * Q$$

where  $b_2$  denotes the vector measurement obtained from the magnetometer. Also,  $e_2$  represents the Earth magnetic field in the inertial frame which its value is available and known for any location in the inertial frame,

$$e_2 = \mathcal{H}_I$$

where  $\mathcal{H}_I$  represents the Earth magnetic field. Having these facts in mind, one can easily conclude that

$$\bar{b}_i = Q^{-1} * \bar{e}_i * Q \quad (5.3)$$

where  $b_i$  denotes the measured vectors in body-fixed frame and  $e_i$  represents the known inertial vectors. Note that, any vector  $u \in \mathbb{R}^3$ , can be expressed in quaternion format given by

$$\bar{u} = \begin{pmatrix} 0 \\ u \end{pmatrix}$$

### 5.1.1 Algorithm 1: Attitude Estimation Using Raw Vector Measurements

In [41], a unit-quaternion based attitude observer is introduced by

$$\dot{\hat{Q}} = \frac{1}{2} \hat{Q} * \bar{\beta} \quad (5.4)$$

where

$$\beta = \Omega - \sum_{i=1}^{i=n} \gamma_i S(\hat{b}_i) b_i. \quad n = 2 \quad (5.5)$$

with  $\hat{Q}$  representing the estimated attitude. Also, in the above equation,  $\gamma_i$  is a constant gain and  $\bar{\beta} = \begin{pmatrix} 0 \\ \beta \end{pmatrix}$  denotes the quaternion formulation of vector  $\beta$ . Note that,

$$\bar{\hat{b}}_i = \hat{Q}^{-1} * \bar{e}_i * \hat{Q}.$$

where  $\hat{b}_i$  denotes the estimated non-collinear vectors (in this case, acceleration and magnetic field) in body-fixed frame. The actual values for these vectors  $b_i$ , can be obtained from the accelerometer and magnetometer directly.

**Proof**

Let  $\tilde{R} = R^T R$  denote the orientation error. The corresponding quaternion error  $\tilde{Q}$ , is given by

$$\tilde{Q} = Q * \hat{Q}^{-1}.$$

Consider the Lyapunov function candidate as [41]

$$\mathcal{E} = \frac{1}{2} \sum_{i=1}^n \gamma_i \tilde{b}_i^T \tilde{b}_i \quad (5.6)$$

where  $\tilde{b}_i = \hat{b}_i - b_i$ . Recalling the fact that for any vector  $u$ , it is possible to write  $RS(u) = -S(Ru)R$ . Therefore, we have

$$\frac{d}{dt} \tilde{b}_i = \frac{d}{dt} \begin{pmatrix} 0 \\ b_i \end{pmatrix} = \begin{pmatrix} 0 \\ \dot{R}e_i \end{pmatrix} = \begin{pmatrix} 0 \\ -S(\Omega)Re_i \end{pmatrix} = \begin{pmatrix} 0 \\ S(b_i)\Omega \end{pmatrix}. \quad (5.7)$$

Similarly,

$$\frac{d}{dt} \bar{\tilde{b}}_i = \frac{d}{dt} \begin{pmatrix} 0 \\ \hat{b}_i \end{pmatrix} = \begin{pmatrix} 0 \\ \dot{\hat{R}}e_i \end{pmatrix} = \begin{pmatrix} 0 \\ S(\hat{b}_i)\beta \end{pmatrix}. \quad (5.8)$$

Using the last two equations, the derivative of the proposed lyapunov function can be written as

$$\dot{\mathcal{E}} = \sum_{i=1}^n \gamma_i \tilde{b}_i^T S(\hat{b}_i)(\beta - \Omega) \quad (5.9)$$

If we replace the term  $(\beta - \Omega)$  by its equivalent term extracted from equation (5.5), we can rewrite the above equation as

$$\dot{\mathcal{E}} = \left( \sum_{i=1}^n \gamma_i \tilde{b}_i^T S(\hat{b}_i) \right) \left( - \sum_{i=1}^n \gamma_i S(\hat{b}_i) b_i \right) \quad (5.10)$$

Since it can be easily proved that  $S(\hat{b}_i) b_i = -S(\hat{b}_i) \tilde{b}_i$ , the above equation can be simplified as

$$\dot{\mathcal{E}} = - \left( \sum_{i=1}^n \gamma_i S(\hat{b}_i) b_i \right)^T \left( \sum_{i=1}^n \gamma_i S(\hat{b}_i) b_i \right) \quad (5.11)$$

The above equation confirms that  $\mathcal{E}$  is non-increasing and bounded. Since  $\ddot{\mathcal{E}}$  is also bounded, we can write

$$\lim_{t \rightarrow \infty} \sum_{i=1}^n \left( \gamma_i S(\hat{b}_i) b_i \right) = \lim_{t \rightarrow \infty} \sum_{i=1}^n \left( \gamma_i \hat{R} S(e_i) \underbrace{\hat{R}^T R}_{\hat{R}} e_i \right) = \lim_{t \rightarrow \infty} \sum_{i=1}^n \left( \gamma_i \hat{R} (e_i \times \tilde{R} e_i) \right) = 0 \quad (5.12)$$

It is clear from the above equation that  $\tilde{R} = I_3$  (corresponding to quaternion  $\tilde{Q} = (\pm 1, 0)$ ), is one of the equilibrium points. This is the desired equilibrium point, however, there are other possible solutions for the equation named as *undesired equilibria* in [41]. To find these undesired solutions, substitution of  $\tilde{R}$  in the above equation with its corresponding representation expressed in equation (2.41), yields to

$$-\tilde{q}_0 \tilde{q}^T \mathcal{W} \tilde{q} = 0 \quad (5.13)$$

while

$$\mathcal{W} = - \sum_{i=1}^n \gamma_i S(e_i)^2.$$

As it can be concluded easily,  $q_0 = 0$  is the solution to equation (5.13). Therefore, the undesired equilibria is given by  $Q = (0, \tilde{q})$ , with  $q$  being an eigenvector of  $\mathcal{W}$ .

It has been proved in [41] that the undesired equilibria are unstable. meaning that  $\tilde{q}_0(t)$  will never cross zero, as long as  $\tilde{q}_0 \neq 0$ . (see reference [41] for more details).

### 5.1.2 Algorithm 2: Attitude Estimation Using Filtered Vector Measurements

In practice, measurements are often subject to noise. In most of engineering applications, filtering methods are applied to eliminate the noise contaminating the measurements. A simple and yet practical filter often used in control algorithms is low-pass filter. In the second attitude observer presented in [41], the low-pass filtered measurements are used to estimate the orientation of a rigid body.

Recalling that in frequency domain, the low-pass filter transfer function is given by

$$H(s) = \frac{\alpha}{\alpha + s} \quad (5.14)$$

In the above equation  $\alpha = \frac{1}{2\pi f_c} > 0$  where  $f_c$  represents the cut-off frequency of the filter. In [41], an attitude observer is presented by

$$\dot{\hat{Q}} = \frac{1}{2} \hat{Q} * \bar{\beta} \quad (5.15)$$

where

$$\beta = \Omega - \alpha \mu \quad (5.16)$$

and  $\mu$  is given by

$$\dot{\mu} = -\alpha\mu + \alpha \sum_{i=1}^n \gamma_i S(\hat{b}_i) b_i \quad (5.17)$$

where  $\alpha > 0$  and  $\gamma_i > 0$ .

### Proof

Consider the Lyapunov function candidate given by

$$\mathcal{E} = \frac{1}{2} \sum_{i=1}^n \gamma_i \tilde{b}_i^T \tilde{b}_i + \frac{1}{2} \mu^T \mu \quad (5.18)$$

Using equations (5.15), the time derivative of the above equation can be calculated as

$$\dot{\mathcal{E}} = \sum_{i=1}^n \gamma_i \tilde{b}_i^T S(\hat{b}_i) (\beta - \Omega) + \mu^T \dot{\mu} \quad (5.19)$$

Replacing equations (5.16) and (5.17) in the above equation leads to

$$\dot{\mathcal{E}} = -\alpha \mu^T \mu = -\alpha \|\mu\|^2 \quad (5.20)$$

Recalling the fact that measurements are bounded, the above equation confirms that  $\mathcal{E}$  is non-increasing and converges to a constant value when  $t$  goes to infinity. Since it can be proved that  $\dot{\mathcal{E}}$  is also bounded, we have

$$\lim_{t \rightarrow \infty} \mu(t) = 0. \quad (5.21)$$

Consequently, we have

$$\lim_{t \rightarrow \infty} \left( \sum_{i=1}^n \gamma_i S(\hat{b}_i) b_i \right) = 0.$$

Using similar argument as those used in the proof of algorithm 1, we can show that the desired equilibria are  $(\tilde{q}_0 = \pm 1, \tilde{q} = 0, \mu = 0)$  and also the *undesired equilibria* are given as

$$(q_0 = 0, \tilde{q}, \mu = 0)$$

with  $\tilde{q}$  being an eigenvector of  $\mathcal{W}$ . It can be shown that the undesired equilibria are unstable.

## 5.2 Measurements and Calibrations

As mentioned in earlier sections, three types of sensors are commonly used for the aircraft attitude estimation: gyroscopes, accelerometers and magnetometers. The local magnetic field observation from the body frame and the acceleration of the airframe are measured by 3-axis magnetometer and 3-axis accelerometer respectively. In light of advantageous factors including low-cost, light weight, small size and low power consumption, the Micro Electro Mechanical Systems (MEMS) inertial sensors have been used on-board the quadrotor under consideration. As a compromise to numerous advantages, there are some uncertainties involved with MEMS sensors measurements specially when it comes to navigation applications in which very accurate measurements are required.

There are a number of valuable publications including [28] which discuss the structure and characteristics of MEMS inertial sensors, giving a general knowledge of possible sources of biases and uncertainties in measurements of these type of sensors. A brief description of each sensor is presented through this chapter followed by a calibration method.

### 5.2.1 Gyroscopes

The performance of MEMS gyroscope is based on the coriolis effect. A pair of masses oscillate constantly with equal magnitude in opposite directions. In consequence, when the sensor is rotated, the coriolis phenomena affects the masses in opposite directions, leading to an orthogonal vibration that can be sensed by a variety of mechanisms (see [13] for more details). Generally, the uncertainties involved with gyro measurements can be divided into the following categories

- **Constant bias** or device offset is usually specified by the manufacturer. However, the offset value may vary slightly in a range. Therefore, for the applications with high precision required like the attitude estimation case, the sensor must be calibrated.
- **Bias drift** or flicker noise, effects the electronic components of gyro sensors at low frequencies.
- **Temperature effect** is generated over a long-term run due to self heating of the device.
- **White noise** contaminates the gyro output in high frequencies.

Generally, the gyros measurements can be modeled as

$$\Omega_{measured} = \Omega + B_g + \xi_g \quad (5.22)$$

where  $B_g$  and  $\xi_g$  represent the constant bias and noise affecting gyro measurements respectively. The gyroscope device used on board of the quadrotor under consideration is an ADXRS300EB, with analog voltage output proportional to the angular rate about the axis normal to the top surface of the sensor.

### Gyro Calibration

While the gyro sensor is still and stationary, the actual angular velocity is zero. Hence, the average of sensor readout is considered as the constant bias. The gyro measurements can be calibrated using this bias. It is clear that the calibrated value would be used in estimation algorithms, such that

$$\Omega = \Omega_{measured} - B_g \quad (5.23)$$

To determine the constant biases, while the gyroscopes are left still and stationary, their output data is collected. Figures (5.1), (5.2), and (5.3) show the data collected from the gyroscopes which have been rigidly attached to the body frame to measure the angular velocity in  $x_B$ ,  $y_B$  and  $z_B$  directions respectively.

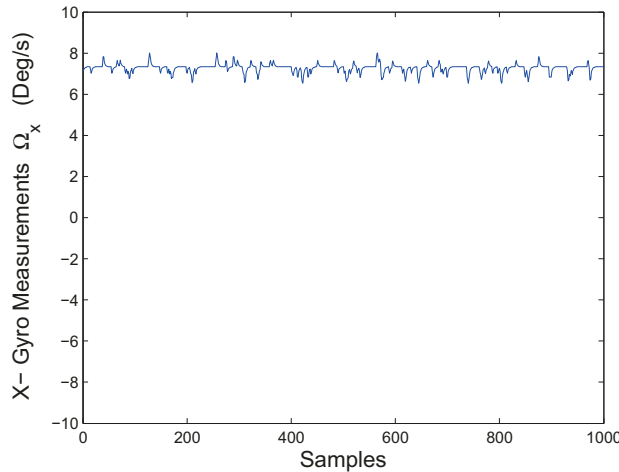


Figure 5.1: Collected Data From Biased X-Gyro

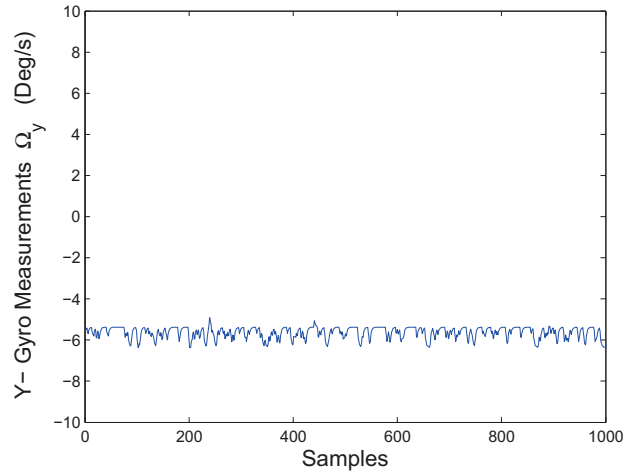


Figure 5.2: Collected Data From Biased Y-Gyro.

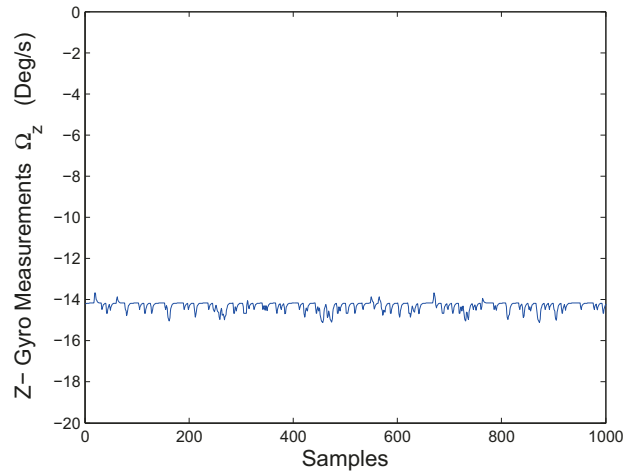


Figure 5.3: Collected Data From Biased Z-Gyro.

As it was mentioned earlier, the average readings obtained from the gyroscopes are considered as the constant biases. Such values have been calculated as

$$\begin{cases} B_{g_x} = 7.27 & \text{Deg/s} \\ B_{g_y} = -5.64 & \text{Deg/s} \\ B_{g_z} = -14.322 & \text{Deg/s} \end{cases}$$

Using the bias values, equation (5.23) is used to provide more accurate angular rate readings.

To verify the effectiveness of the calibration process, while the gyroscopes are left in stationary condition, the output data is collected. Such data is calibrated using equation (5.23) and the bias values which were calculated through the previous experiment. The results are plotted and shown in figures (5.4), (5.5) and (5.6). A simple comparison between the gyro readings in the last two experiments confirms that the accuracy of angular rate measurements have been improved in terms of constant bias elimination.

Note that when the sensor is powered in a long interval of time, the bias changes slightly due to temperature variations.

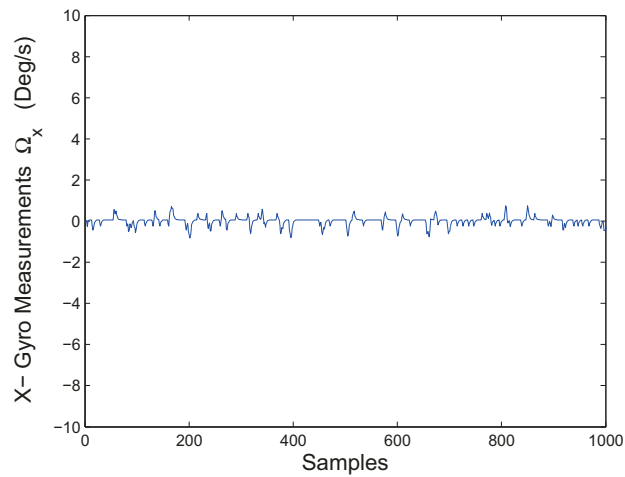


Figure 5.4: Collected Data From the Calibrated X-Gyro

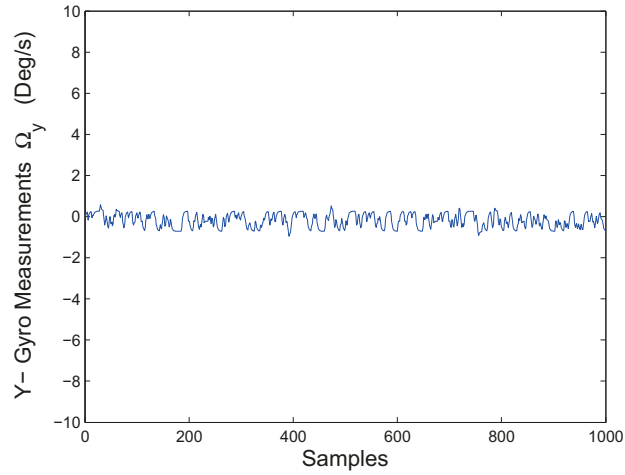


Figure 5.5: Collected Data From the Calibrated Y-Gyro.

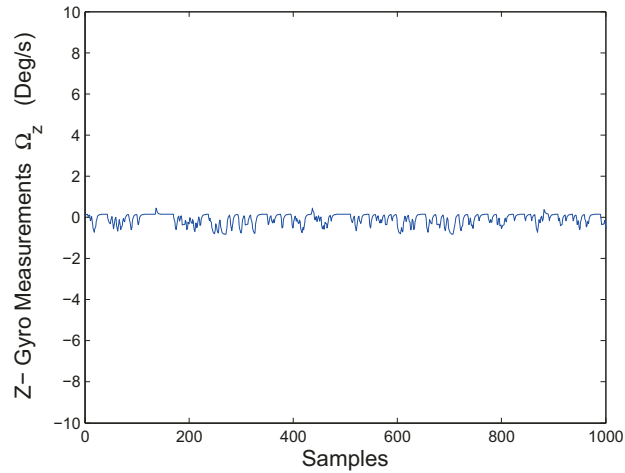


Figure 5.6: Collected Data From the Calibrated Z-Gyro.

### 5.2.2 3-axis Accelerometer

The performance of the most successful type of MEMS accelerometers, is based on capacitive transduction. Among several attractive features fulfilled by this type of accelerometers, the low power consumption and good stability with respect to the temperature variation can be mentioned. ADXL330 is a three axis capacitive accelerometer used in our application. Typically, a MEMS accelerometer consists of a movable proof mass attached to a reference frame through a mechanical suspension system. The acceleration is

given by measuring the displacement of proof mass caused by the capacitance difference (see [34],[7] and [6] for more details).

If we assume the misalignments in measurements to be negligible, the accelerometer output can be modeled as

$$\mathcal{A}_{measured} = \mathcal{A} + B_a + \xi_a \quad (5.24)$$

where  $B_a$  and  $\xi_a$  represent the constant bias and noise affecting accelerometer measurements respectively.

In quadrotor attitude estimation case, the accelerometer must be placed as close as possible to the center of gravity of the aircraft to provide more accurate acceleration readout. As mentioned by manufacturer, the output of the ADXL330 has a typical bandwidth greater than 500 Hz. A common practical approach to eliminate the high frequency noise is low-pass filtering the output signal of the sensor. To fulfill this purpose, in this project, a hardware low pass filter was implemented on the output circuitry of Eval-ADXL330 with a cut-off frequency of  $50Hz$ .

### Accelerometer Calibration

Due to limitations in test instruments and setup configuration, a very accurate accelerometer calibration for vibration and sensitivity issues is not considered in this project. However, a simple possible bias calibration method is provided by collecting the accelerometer data while it is placed in known orientations. Ideally, Considering the sensor to be stationary, the acceleration sensed by the sensor is the gravitational acceleration. Therefore, equation (5.24) can be rewritten as

$$\mathcal{A}_{measured} = -gRz_I + B_a \quad (5.25)$$

where  $g$  denotes the gravitational acceleration. Thus, collecting the accelerometer measurements in known orientations yields to finding the constant bias. It is clear that, the calibrated measurements are used in attitude estimation algorithms.

### 5.2.3 Magnetometer

The 3-axis magnetometer used through this project is HMC2003, a magneto resistive sensor. A typical magneto resistive chip is composed of permalloy strips. The electrical resistance of the permalloy thin films changes with local magnetic field variation leading to measurement of magnetic field strength and direction [37]. In practice, there are some limitations in using this type

of sensors in a wide temperature range due to the effect of heat on the resistance of the strips. In addition to white noise and temperature effects, the magnetometer output is mainly effected by the magnetic distortions based on ferromagnetic materials in the environment. Magnetic distortions can be divided into two categories,

- **Soft iron** distortions arise from the soft ferromagnetic materials in surrounding environment. This type of magnetic distortions are dependent upon the orientation of the material relative to the sensor and magnetic field. Since compensation for soft iron disturbances requires complex calculations and specific instruments, the best approach is to evacuate the surrounding environment from the soft iron materials.
- **Hard iron** distortions are originated from permanent magnets or magnetized materials on the magnetometer platform. In better words, since these materials are fixed-located relative to the sensor, hard iron effects cause a constant bias in sensor readings. There are a number of valuable publications in literature including [10] and [21] discussing a calibration method to eliminate the hard iron effects. The compensation method for hard iron biases presented in the coming section is inspired by [14].

### Magnetometer Calibration

Considering the hard iron biases, the magnetometer output can be modeled as

$$\mathbf{m}' = \mathbf{m} + B_m + \xi_m \quad (5.26)$$

where  $\mathbf{m}'$  and  $\mathbf{m}$  denote the measured and actual magnetic field respectively.

Also,  $B_m = \begin{pmatrix} B_{m_x} \\ B_{m_y} \\ B_{m_z} \end{pmatrix}$  and  $\xi_m$  represent constant biases and noise respectively.

In theory, when the surrounding environment is not disturbed by any external field, the magnetometer measures the Earth magnetic field which has a constant distinguished value in every location on the Earth. Generally, the Earth magnetic field points down toward the geographic north pole in northern hemisphere. Taking the longitude and latitude of a geographical location into the account, the Earth magnetic field vector can be decomposed in two components: horizontal and vertical. As on the Earth level the horizontal component always directs toward the geographical north, this fact has been used for decades to determine the heading in aircraft and navigation.

Let  $\vec{\mathcal{H}}$  denote the Earth magnetic field with a known local magnitude  $\mathcal{H}$ .

Therefore,

$$\mathcal{H}^2 = \mathcal{H}_x^2 + \mathcal{H}_y^2 + \mathcal{H}_z^2 \quad (5.27)$$

where  $\mathcal{H}_x$ ,  $\mathcal{H}_y$  and  $\mathcal{H}_z$  represent the projection of the Earth magnetic field on the axes of the inertial frame. In practice, while no external field is present about the magnetometer, each component of the magnetometer output measures the projection of Earth magnetic field on the corresponding axis. using equations (5.26) and (5.27) one can write

$$\mathcal{H}^2 = (\mathbf{m}' - B_m)^2 = (\mathbf{m}'_x - B_{m_x})^2 + (\mathbf{m}'_y - B_{m_y})^2 + (\mathbf{m}'_z - B_{m_z})^2 \quad (5.28)$$

It is clear that equation (5.28) is the parametric equation of a sphere centered at  $B_m$ . A possible compensation method for constant bias is collecting magnetometer data in any possible orientation in three dimensional space and apply some specific numerical calculations to fit the data in a sphere located at body-frame origin by estimating the bias (see for instance [14] and [21]). However, the required process can be decreased to minimum by considering the problem in two dimensions. Therefore, an appropriate calibration procedure is to locate the sensor such that its  $z$  axis is normal to the Earth level and collect data while the sensor is undergoing a rotation by 360 degrees about its  $z$  axis. Thus, the sensor output model can be rewritten as

$$(\mathcal{H}_h)^2 = (\mathbf{m}'_x - B_{m_x})^2 + (\mathbf{m}'_y - B_{m_y})^2 \quad (5.29)$$

where  $\mathcal{H}_h$  denotes the horizontal component of Earth magnetic field. Equation (5.29) is the parametric equation of a circle centered at  $\begin{pmatrix} B_{m_x} \\ B_{m_y} \end{pmatrix}$ . Fitting the collected data in this equation leads to finding  $B_{m_x}$  and  $B_{m_y}$ . Similarly, if we repeat the experiment for at least one of the other normal axes  $x$  and  $y$ , the third component of hard iron bias,  $B_{m_z}$  can be determined.

### Verification of Hard Iron Calibration

Figures (5.7) and (5.8) show the collected data from the magnetometer under consideration, during the calibration process described earlier.

While the upper and lower extreme values of each axis measurement is provided, a simple way to calculate the biases is given by

$$\begin{cases} B_x = \frac{1}{2}(\mathbf{m}_{x \max} + \mathbf{m}_{x \min}) \\ B_y = \frac{1}{2}(\mathbf{m}_{y \max} + \mathbf{m}_{y \min}) \\ B_z = \frac{1}{2}(\mathbf{m}_{z \max} + \mathbf{m}_{z \min}) \end{cases} \quad (5.30)$$

Figures (5.9) and (5.10) show the collected data during the same process from the calibrated sensor. Comparison of raw and calibrated measurements confirms that accuracy has been improved through the sensor calibration.

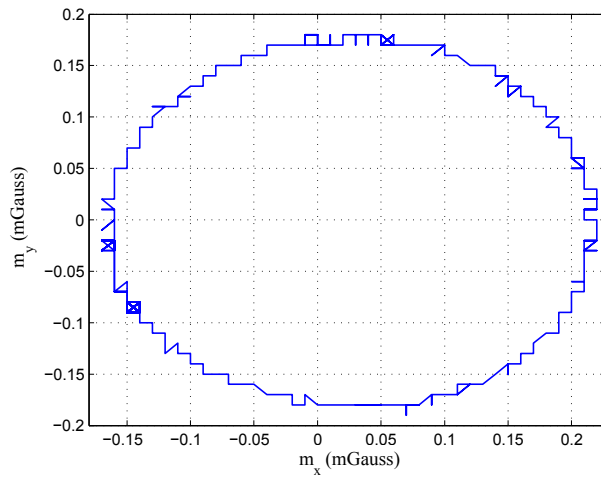


Figure 5.7: Collected Data From Biased Magnetometer (through 360° rotation about z axis)

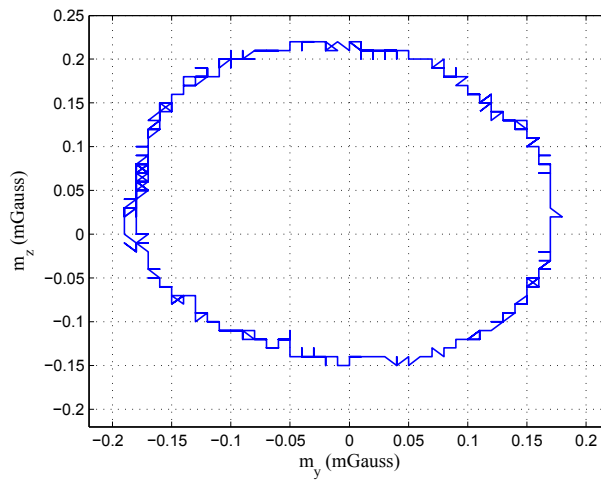


Figure 5.8: Collected Data From Biased Magnetometer (through 360° rotation about x axis).

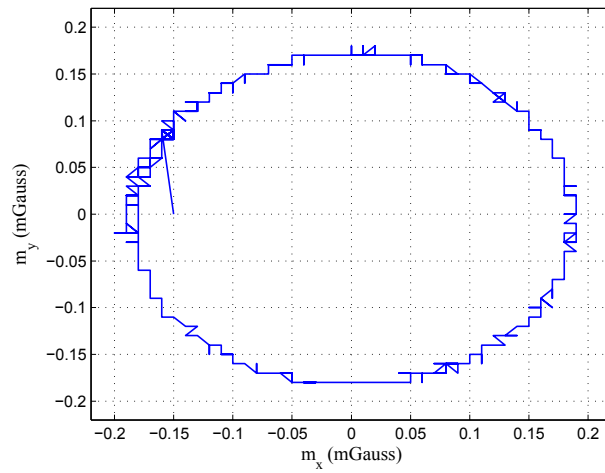


Figure 5.9: Collected Data From the Calibrated Magnetometer (through 360° rotation about z axis).

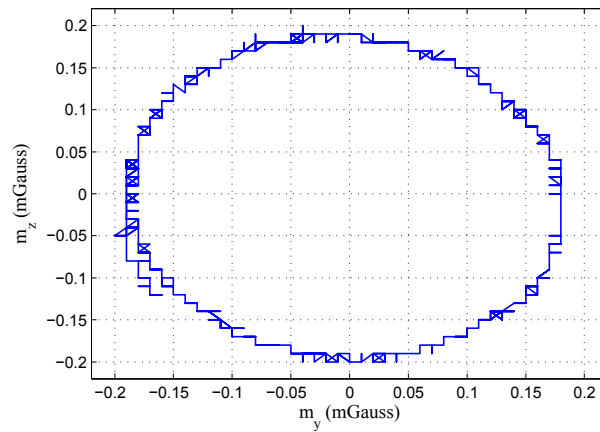


Figure 5.10: Collected Data From the Calibrated Magnetometer (through 360° rotation about x axis).

## Attitude Control

Attitude stabilization of an aircraft is the crucial requirement for autonomous navigation. For a small scale quadrotor robot, the combination of the aircraft model and estimated orientation provided through fusion of sensor information, makes it possible to design a feedback controller for this platform.

PID control is a simple and practical method proved to be reliable in attitude stabilization case. A large group of attitude controllers discussed in the literature consist of a PD controller plus a compensation term. For instance, the gyroscopic effect due to nonlinear coupling of rotational motion of the rotors and the airframe can be compensated for, through the control law. In general, the proportional gain is provided in terms of the vector part of the quaternion error while the derivative feedback is introduced in terms of the angular velocity. The stability analysis of such control approaches has been discussed for instance in [42]. The main goal in attitude stabilization problem is to drive the rigid body to a desired stable target orientation. Once the control law is designed assuring the attitude stabilization, some steps are taken to develop the required motor velocities corresponding to such a control input.

In addition to the  $PD$  approach, a few other control strategies have been implemented and proved to be practical in different research projects. For instance a  $PD^2$  attitude controller is introduced and implemented successfully in [40]. Also, a backstepping control technique is provided in [8] and [20], which has been used to achieve hovering flight for a model quadrotor aircraft successfully. There are also a number of projects including [5], which use visual sensors and communication capabilities to control the orientation of a miniature quadrotor aircraft.

Through this project the classical  $PD$  controller is discussed and implemented to stabilize the orientation of the quadrotor aerial robot under consideration.

## 6.1 PD Control

Consider quadrotor kinematic model expressed in (4.21), under the following control law

$$\tau_a = -\Lambda\Omega - \lambda q \quad (6.1)$$

where  $\lambda$  is a positive scalar gain and  $\Lambda$  represents a  $3 \times 3$  positive definite matrix gain. It has been proved in [40], that equilibrium point ( $q_0 = \pm 1, q = 0, \Omega = 0$ ) is globally asymptotically stable. The proof is reviewed in the following section.

Since the control law expressed in (6.1), contains no terms related to inertia matrix of the body frame, it is robust with respect to uncertainties of the system parameters.

### 6.1.1 Stability Proof

Consider the following Lyapunov function candidate motivated by the total energy of the the rigid body,

$$\mathcal{E} = \frac{1}{2}\Omega^T I_f \Omega + \lambda q^T q + \lambda(q_0 - 1)^2 \quad (6.2)$$

Recalling the definition of unit quaternion norm, the above equation can be simplified as

$$\mathcal{E} = \frac{1}{2}\Omega^T I_f \Omega + 2\lambda(1 - q_0). \quad (6.3)$$

Taking derivative of such Lyapunov candidate function with respect to the time, results in

$$\dot{\mathcal{E}} = \frac{1}{2}\left(\dot{\Omega}^T I_f \Omega + \Omega^T I_f \dot{\Omega}\right) - 2\lambda\dot{q}_0 \quad (6.4)$$

which can be simplified as

$$\dot{\mathcal{E}} = \Omega^T I_f \dot{\Omega} - 2\lambda\dot{q}_0 \quad (6.5)$$

On the other hand, substitution of  $\dot{q}_0$  in the above equation by the definition given in equation (4.6), leads to

$$\dot{\mathcal{E}} = \Omega^T I_f \dot{\Omega} - 2\lambda\left(-\frac{1}{2}q^T \Omega\right). \quad (6.6)$$

Recalling the dynamic model of the rigid body expressed in equation (4.21), we have

$$\dot{\Omega} = I_f^{-1} \left( (-\Omega \times I_f \Omega) - G_a + \tau_a \right) \quad (6.7)$$

Considering equation (6.7), we can rewrite equation (6.6) as

$$\dot{\mathcal{E}} = \Omega^T \left( (-\Omega \times I_f \Omega) - G_a + \tau_a \right) + \lambda q^T \Omega. \quad (6.8)$$

The first term in the right side of the previous equation can be rewritten, recalling the fact that

$$\Omega^T (-\Omega \times I_f \Omega) = 0$$

and also

$$-\Omega^T G_a = -I_r \Omega^T \left( (\Omega \times z_I) (\omega_1 + \omega_2 - \omega_3 - \omega_4) \right) = 0$$

Therefore, equation (6.8) can be simplified as

$$\dot{\mathcal{E}} = \Omega^T \tau_a + \lambda q^T \Omega \quad (6.9)$$

On the other hand, replacing the control law modified by equation (6.1) in the previous equation, one can simply conclude

$$\dot{\mathcal{E}} = -\Omega^T \Lambda \Omega. \quad (6.10)$$

Since  $\Lambda$  was defined earlier as a positive definite matrix, it is clear that the above equation is negative semi-definite. This can be used to conclude that  $q_0$ ,  $\Omega$  and consequently  $\dot{\Omega}$  are bounded. Hence,

$$\lim_{t \rightarrow \infty} \dot{\Omega}(t) = \lim_{t \rightarrow \infty} \Omega(t) = 0 \quad (6.11)$$

Combination of the above expression and the dynamic model of the aircraft proves that

$$\lim_{t \rightarrow \infty} \tau_a(t) = \lim_{t \rightarrow \infty} \left( -\Lambda \Omega - \lambda q \right) = 0. \quad (6.12)$$

Using equation (6.12) and the fact that the quaternion norm is unit, it is clear that

$$\begin{cases} \lim_{t \rightarrow \infty} q(t) = 0, \\ \lim_{t \rightarrow \infty} q_0(t) = \pm 1. \end{cases} \quad (6.13)$$

The above equation indicates that the equilibrium point  $(q_0 = \pm 1, q = 0, \Omega = 0)$ , is asymptotically stable.

## 6.2 Rotors Speed Controller

The quadrotor aerial robot is capable of attaining hovering flight, once the speed of the rotors are driven to the desired speed corresponding to designed attitude control law. To control the speed of the rotors, a high gain feedback control strategy is used through this project. Such approach is based on using a feedback proportional to the rotor speed error which is defined as

$$\tilde{\omega}_i = \omega_i - \omega_d \quad , i \in \{1, 2, 3, 4\} \quad (6.14)$$

where  $\omega_d$  denotes the desired speed of the rotors. To obtain the desired speed corresponding to the control law given in (6.1), consider equations (4.13) and (4.16). Therefore, one can write

$$\begin{pmatrix} \tau_a^1 \\ \tau_a^2 \\ \tau_a^3 \\ T \end{pmatrix} = \begin{pmatrix} 0 & 0 & -db & db \\ db & -db & 0 & 0 \\ k & k & -k & -k \\ b & b & b & b \end{pmatrix} \begin{pmatrix} \omega_{d1}^2 \\ \omega_{d2}^2 \\ \omega_{d3}^2 \\ \omega_{d4}^2 \end{pmatrix}. \quad (6.15)$$

Using the above equation, the desired speed of rotors can be derived as

$$\bar{\omega}_d = F^{-1}\chi \quad (6.16)$$

where  $\bar{\omega}_d = \begin{pmatrix} \omega_{d1}^2 \\ \omega_{d2}^2 \\ \omega_{d3}^2 \\ \omega_{d4}^2 \end{pmatrix}$  and  $\chi = \begin{pmatrix} \tau_a^1 \\ \tau_a^2 \\ \tau_a^3 \\ T \end{pmatrix}$ . Also  $F$  denotes the  $4 \times 4$  matrix in

equation (6.15).

When the desired speed of rotors are known, considering the rotor dynamic model expressed in equation (4.19), a control law can be developed as

$$\tau_i = Q_i + I_r \dot{\omega}_{d,i} - \kappa_i \tilde{\omega}_i, \quad i \in \{1, 2, 3, 4\} \quad (6.17)$$

where  $\kappa_i$  represents four positive design parameters.

As mentioned in earlier chapters, four permanent magnet brushed DC motors are used in the quadrotor platform under the consideration. These motors are the actuators at the heart of control system. Since DC motors are voltage controlled via PWM signals, it is necessary to define a relation between designed rotor torques  $\tau_i$  and corresponding motor voltage  $V_i$ .

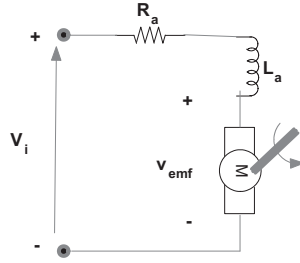


Figure 6.1: Electro-mechanical model of a DC motor.

As it is shown in figure (6.1), applying voltage  $V_i$  to the poles of a DC motor causes the current  $I_a$  to flow, making the armature accelerate. Assuming an ideal motor with no friction in bearings and no electrical loss, while the armature inductance is negligible, one can write

$$V_i = R_a I_a + v_{e.m.f}^i \quad (6.18)$$

where  $v_{e.m.f}^i$  denotes the back e.m.f and can be expressed in terms of motor torque as

$$v_{e.m.f}^i = K_m \omega_m^i \quad (6.19)$$

where  $K_m$  and  $\omega_m^i$  represent the motor constant and motor speed respectively. On the other hand, generated torque by each motor  $\tau_m$ , due to flow of current  $I_a$  can be written as [26]

$$\tau_m = K_m I_a. \quad (6.20)$$

Let  $K_g$  denote the gear ratio, the motor torque  $\tau_m^i$  and motor speed  $\omega_m^i$  are related to the rotor torque  $\tau_i$  and speed  $\omega_i$ , respectively. Such relation is expressed as

$$\begin{cases} \tau_m^i = \frac{\tau_i}{K_g} \\ \omega_m^i = K_g \omega_i. \end{cases} \quad (6.21)$$

Substitution of the above expressions as well as equations (6.19) and (6.20) in equation (6.18) leads to finding a relation between motor voltage and rotor torque, given as

$$V_i = \frac{R_a}{K_m K_g} \tau_i + K_m K_g \omega_i. \quad (6.22)$$

This voltage can be converted to appropriate PWM signal to derive the motors.

### 6.3 Control Design Summary

Figure (6.2) shows the flowchart of control design for a quadrotor aerial robot.

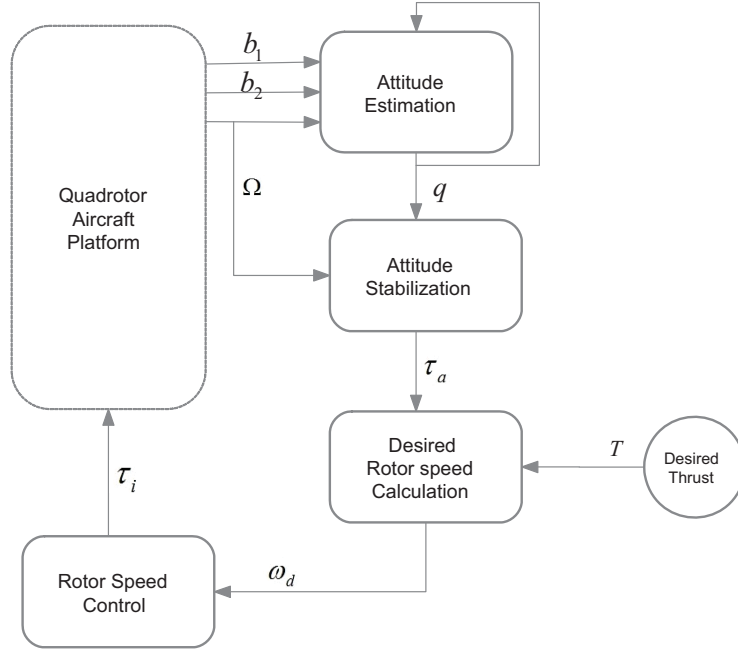


Figure 6.2: Control Strategy Diagram.

### 6.4 Attitude Tracking Problem

In fact, the quadrotor system under the control law presented in equation (6.1), can be managed to achieve the capability of attitude tracking. The desired orientation of the aircraft is  $(\psi_d, \theta_d, \varphi_d)$  is provided by the pilot through a joystick or software interface. The orientation error is defined as

$$\begin{pmatrix} \tilde{\psi} \\ \tilde{\theta} \\ \tilde{\varphi} \end{pmatrix} = \begin{pmatrix} \psi - \psi_d \\ \theta - \theta_d \\ \varphi - \varphi_d \end{pmatrix}. \quad (6.23)$$

Let  $\bar{Q}$  denote the quaternion formulation of the above error expression. Hence, if we apply  $\bar{q}$  to the control law in equation (6.1) as the quaternion

part, one can conclude

$$\begin{cases} \lim_{t \rightarrow \infty} \bar{q}(t) = 0, \\ \lim_{t \rightarrow \infty} \bar{q}_0(t) = \pm 1. \end{cases} \quad (6.24)$$

which means

$$\lim_{t \rightarrow \infty} \begin{pmatrix} \psi \\ \theta \\ \varphi \end{pmatrix} = \begin{pmatrix} \psi_d \\ \theta_d \\ \varphi_d \end{pmatrix}. \quad (6.25)$$

This ensures that the attitude of the quadrotor aerial robot can be regulated to any desired orientation.

## Simulations

Through this chapter, the performance of the attitude controller is testified and analyzed via a number of simulations. The dynamical model of a quadrotor aircraft has been coded in Matlab Simulink environment, while the required model parameters were chosen as shown in table (7.2). These parameters are mostly related to the physical characteristics of the hardware. The information presented in table (7.2) have been investigated using a series of experiments mainly inspired by the methods discussed in [26] and have been documented in appendix 1. While the PD controller described in the previous chapter was applied, the controller gains were tuned through trial and error to provide a satisfactory system performance. For each simulation presented in the following sections, the initial conditions are considered equivalent to those given in table (7.1). Also the desired thrust is defined as  $T = 12N$ .

| Parameter         | Value                                                                                                                                                                                                |
|-------------------|------------------------------------------------------------------------------------------------------------------------------------------------------------------------------------------------------|
| Initial Condition | $\Omega = 0$<br>$Q(0) = (0.94, -0.17, 0.31, -0.04)^T$<br>$\begin{pmatrix} \psi(0) \\ \theta(0) \\ \varphi(0) \end{pmatrix} = \begin{pmatrix} -12.5^\circ \\ 34.3^\circ \\ -24.4^\circ \end{pmatrix}$ |
| Controller Gains  | $\lambda = 0.8$<br>$k_i = 0.0012$<br>$\Lambda = \text{diag}(0.1, 0.1, 0.08)$                                                                                                                         |

Table 7.1: Simulation Parameters

It must be mentioned that, there are practical limitations involved with the motors in terms of angular speed and input voltage. The maximum angular velocity and input voltage of the motors in physical setup under consideration are  $300 \text{ rad/s}$  and  $12V$  respectively. Hence, the controller gains have been tuned such that the angular speed and the input voltage of each motor would not exceed the limitations.

| Model Parameter | Description              | Value                  | Units    |
|-----------------|--------------------------|------------------------|----------|
| $d$             | Distance                 | 0.225                  | $m$      |
| $g$             | Gravity                  | 9.81                   | $m/s^2$  |
| $M$             | Mass                     | 0.50071                | $kg$     |
| $R_a$           | Motor Resistance         | 1.1                    | $\Omega$ |
| $K_m$           | Motor Constant           | $4.137 \times 10^{-3}$ | $Nm/A$   |
| $K_g$           | Gear Ratio               | 5.6                    |          |
| $K$             | Proportionality Constant | $1.120 \times 10^{-6}$ |          |
| $b$             | Proportionality Constant | $2.923 \times 10^{-5}$ |          |
| $I_r$           | Rotor Inertia            | $4.43 \times 10^{-5}$  | $kg.m^2$ |
| $I_{f_\psi}$    | Roll Inertia             | $3.735 \times 10^{-3}$ | $kg.m^2$ |
| $I_{f_\theta}$  | Pitch Inertia            | $3.735 \times 10^{-3}$ | $kg.m^2$ |
| $I_{f_\varphi}$ | Yaw Inertia              | $1.33 \times 10^{-2}$  | $kg.m^2$ |

Table 7.2: Quadrotor Aircraft Model Parameters.

## 7.1 Simulation 1

Given the initial conditions, the objective of simulation 1 is to explore the performance of the controller in stabilizing the quadrotor in hovering condition,  $Q = (1, 0, 0, 0)$ . Performing this simulation, the angular velocity of the aircraft  $\Omega$  and the control effort  $\tau_i$  of each motor were plotted. The results are presented in figures (7.3) and (7.5)-(7.8) respectively. Also to provide a better attitude visualization, a plot is given in figure (7.2) for the aircraft angles. The required input voltage for motors is monitored as well and the results are given in a plot via figure (7.4).

Simulation results clearly confirm the convergence of the aircraft attitude to the equilibrium point (hovering condition), as it was expected.

## 7.2 Simulation 2

While disturbance is introduced in the attitude of the aircraft model, the task of simulation 2 is to test the performance of the closed loop system in the presence of disturbance. Starting from the initial conditions given in table (7.2), a disturbance is considered to affect roll, pitch and yaw angle of the aircraft separately at a specified time. Table (7.3) shows the specifications of the disturbances considered in this simulation.

| Effectuated Angle | Disturbance | Duration ( <i>sec</i> ) | Time ( <i>sec</i> ) |
|-------------------|-------------|-------------------------|---------------------|
| Roll, $\psi$      | $-20^\circ$ | 0.05                    | 6.5                 |
| Pitch, $\theta$   | $15^\circ$  | 0.05                    | 4.5                 |
| Yaw, $\varphi$    | $10^\circ$  | 0.05                    | 2.5                 |

Table 7.3: Disturbance Specification in Simulation 2.

The plots are given for the angular velocity and the orientation of the aircraft  $Q$  as shown in figures (7.11) and (7.9). Also, the control effort  $\tau_i$  and the input voltage of the motors are depicted in figures (7.13)-(7.16) and (7.12). From the simulation results, it can be seen that the system is capable of rejecting external disturbances, once the balance is disturbed. Monitoring the simulation results for the control effort shows a sharp rise and fall, shortly after the disturbance is introduced in the system. The simulation results for the control effort reflect the quick reaction of the control system to compensate for the disturbance effects.

## 7.3 Simulation 3

While a desired attitude is introduced, the objective of simulation 3 is to investigate the performance of the system in tracking the desired orientation. Performing this simulation, it has been considered that the pilot demands to stabilize the aircraft in hovering condition, then introduces a desired attitude as

$$\begin{pmatrix} \psi_d \\ \theta_d \\ \varphi_d \end{pmatrix} = \begin{pmatrix} 25^\circ \\ 10^\circ \\ 30^\circ \end{pmatrix}$$

at the specified time  $t = 3sec$ .

Similar to the other simulations presented in this chapter, the plots are given

for the angular velocity and the orientation of the aircraft as shown in figures (7.17) and (7.19). Also, the control effort and the required input voltage for motors are presented in figures (7.21)-(7.24) and (7.20). The results clearly insure that, once introduced by the pilot, the desired attitude can be reached with a satisfactory settling time.

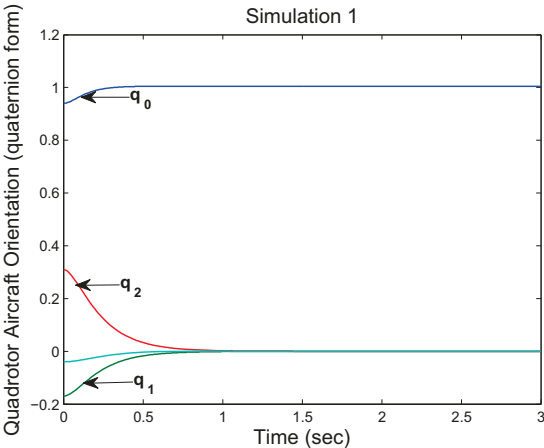


Figure 7.1: Aircraft Orientation, Simulation 1.

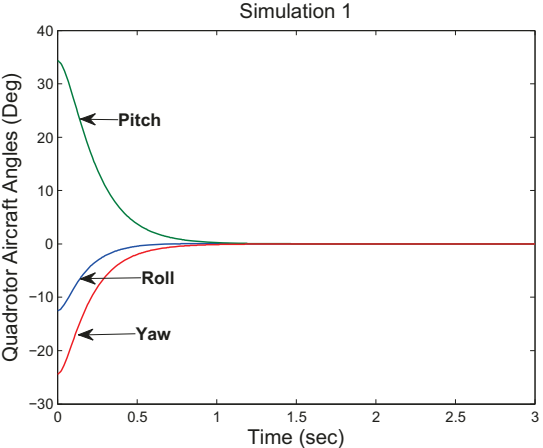


Figure 7.2: Aircraft Angles, Simulation 1.

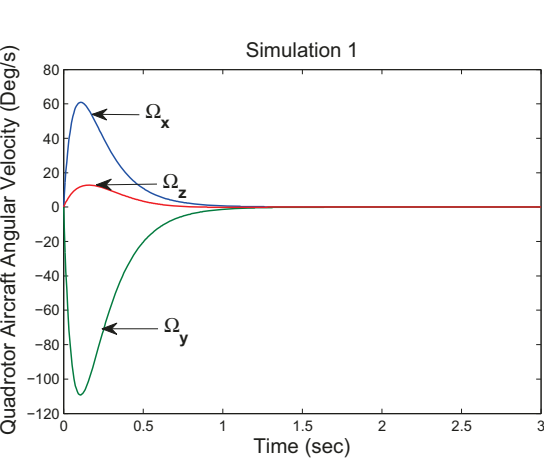


Figure 7.3: Angular Velocity, Simulation 1.

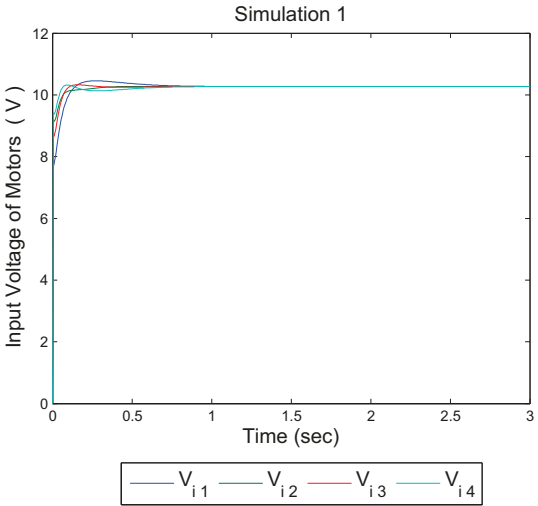


Figure 7.4: Input Voltage, Simulation 1.

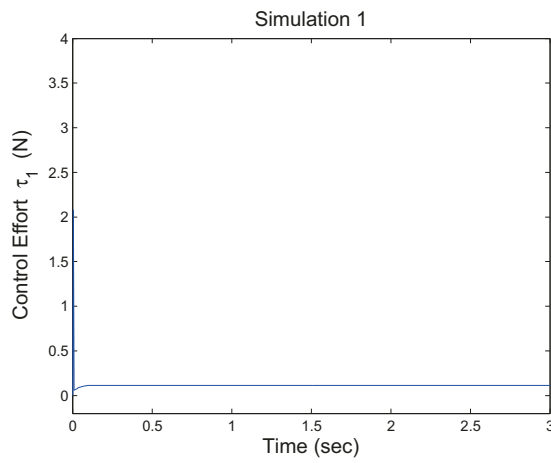


Figure 7.5: Control Effort 1, Simulation 1.

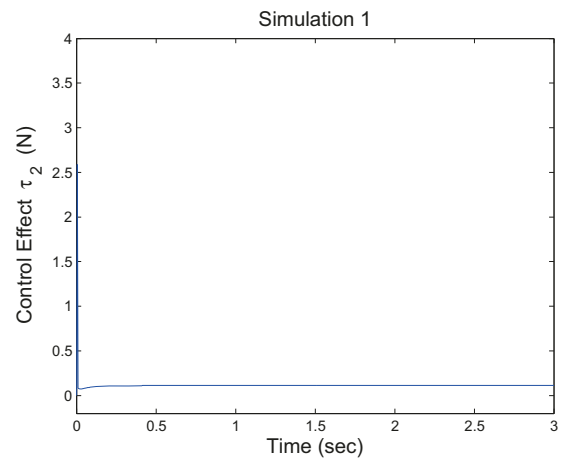


Figure 7.6: Control Effort 2, Simulation 1.

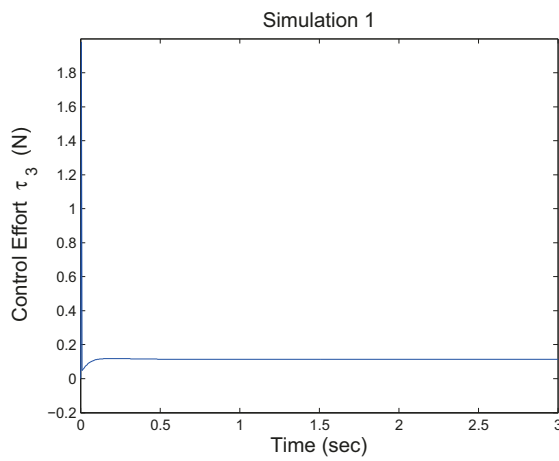


Figure 7.7: Control Effort 3, Simulation 1.

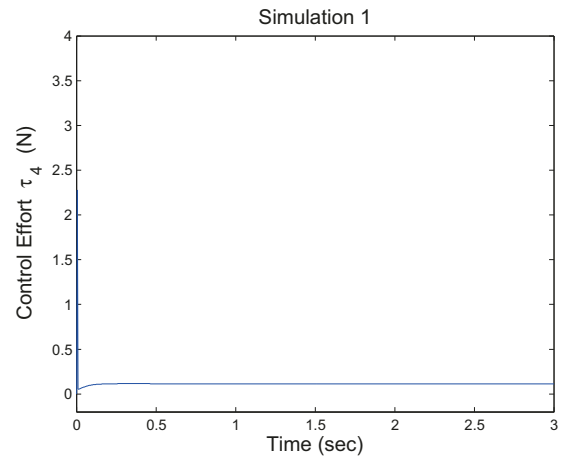


Figure 7.8: Control Effort 4, Simulation 1.

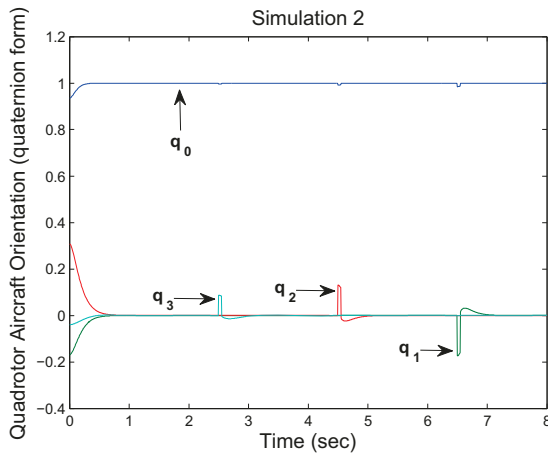


Figure 7.9: Aircraft Orientation, Simulation 2.

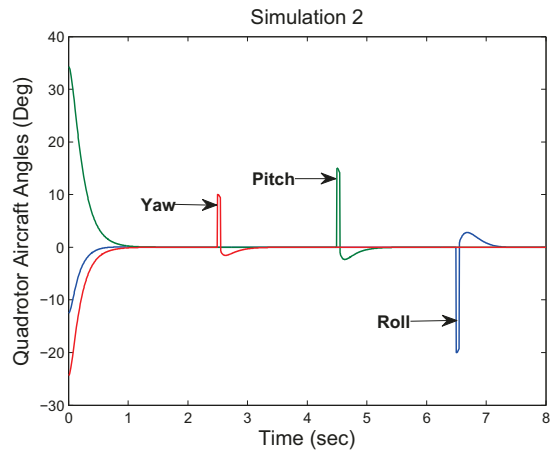


Figure 7.10: Aircraft Angles, Simulation 2.

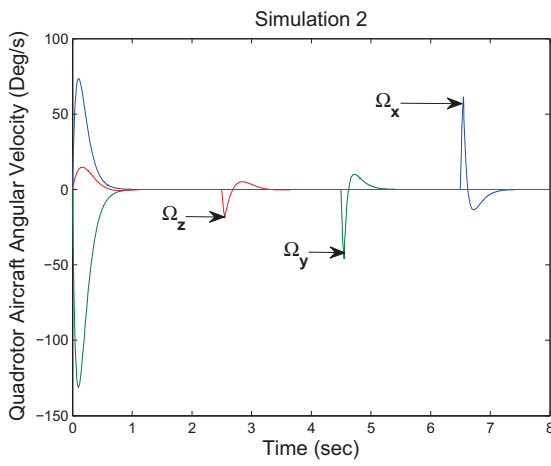


Figure 7.11: Angular Velocity, Simulation 2.

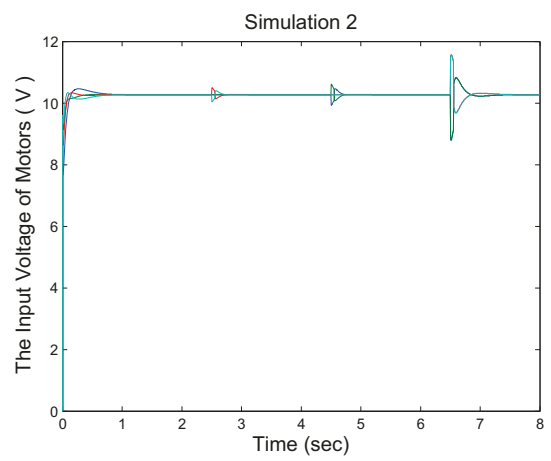


Figure 7.12: Input Voltage, Simulation 2.

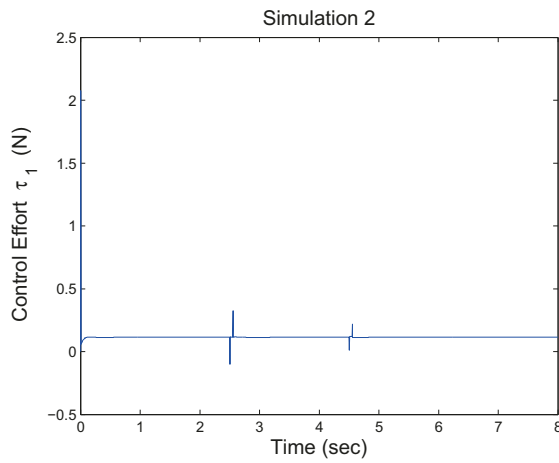


Figure 7.13: Control Effort 1, Simulation 2.

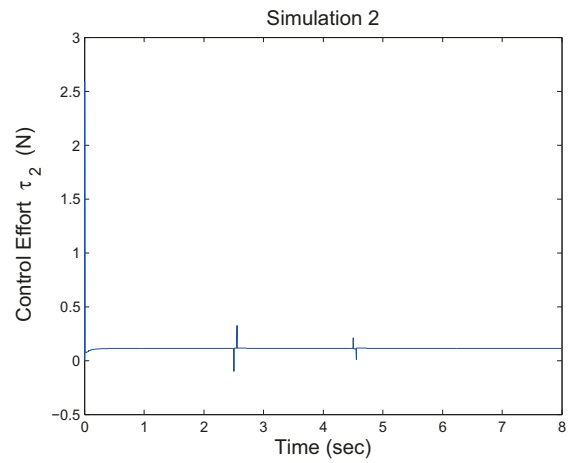


Figure 7.14: Control Effort 2, Simulation 2.

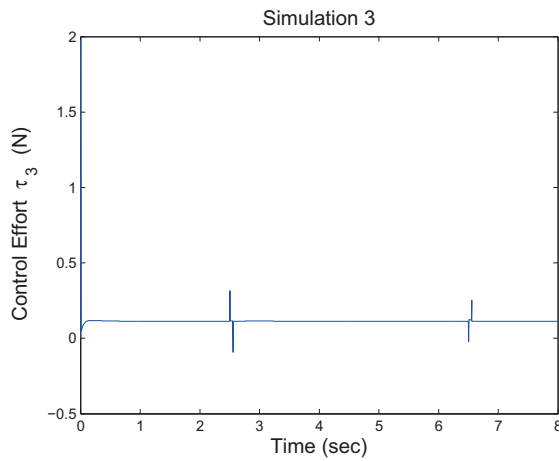


Figure 7.15: Control Effort 3, Simulation 2.

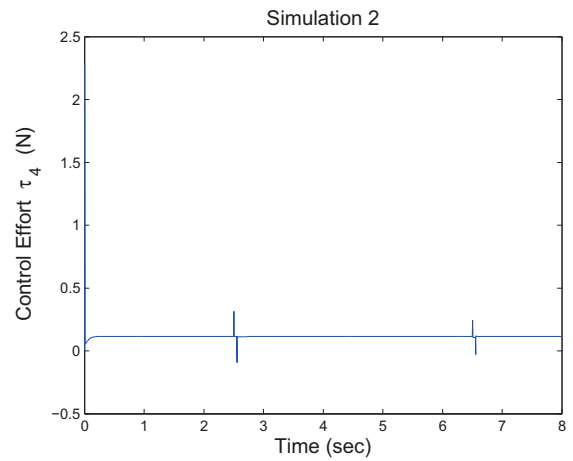


Figure 7.16: Control Effort 4, Simulation 2.

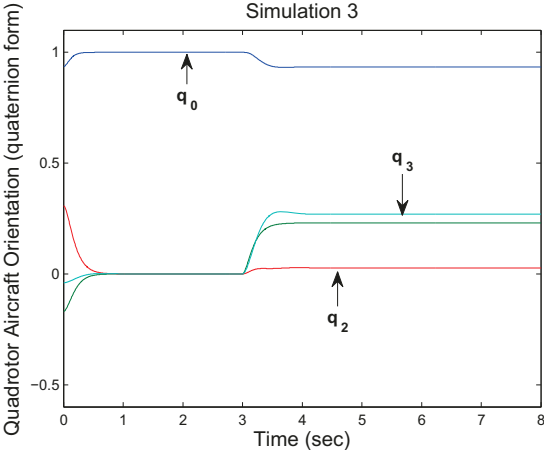


Figure 7.17: Aircraft Orientation, Simulation 3.

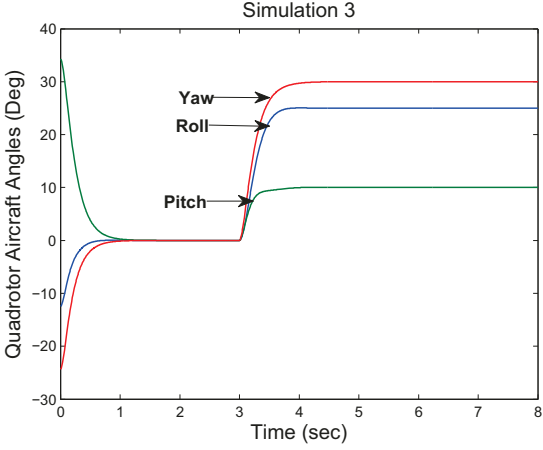


Figure 7.18: Aircraft Angles, Simulation 3.

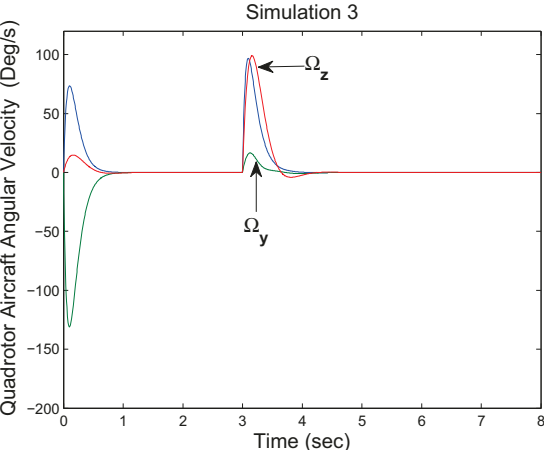


Figure 7.19: Angular Velocity, Simulation 3.

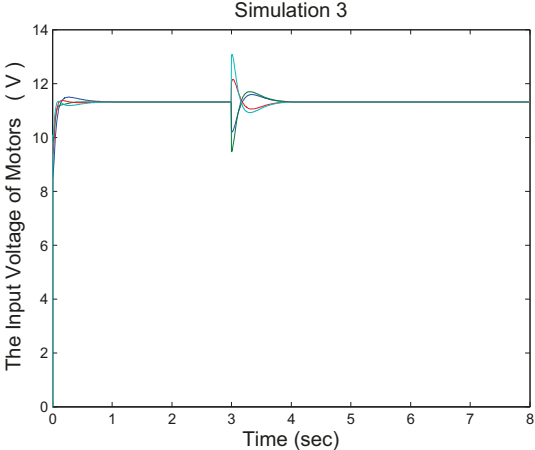


Figure 7.20: Input Voltage, Simulation 3.

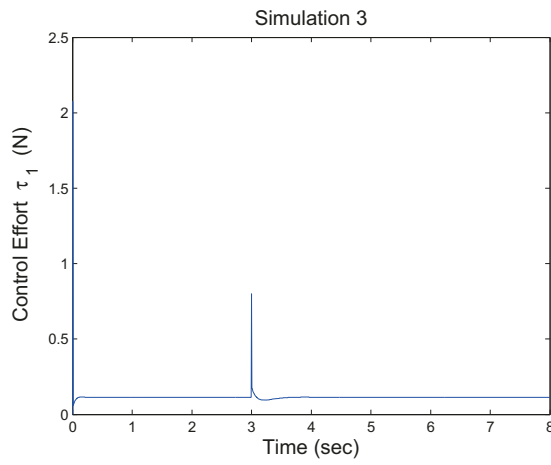


Figure 7.21: Control Effort 1, Simulation 3.

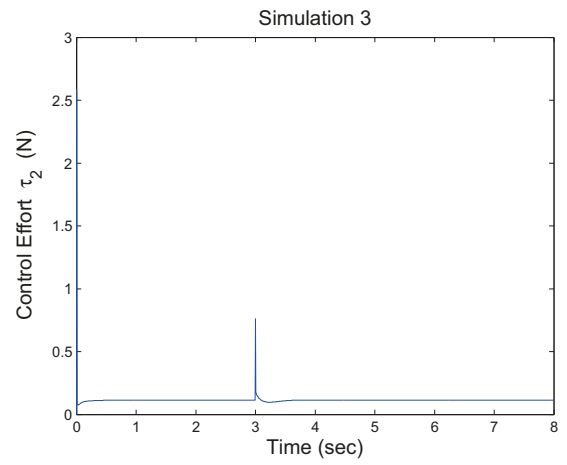


Figure 7.22: Control Effort 2, Simulation 3.

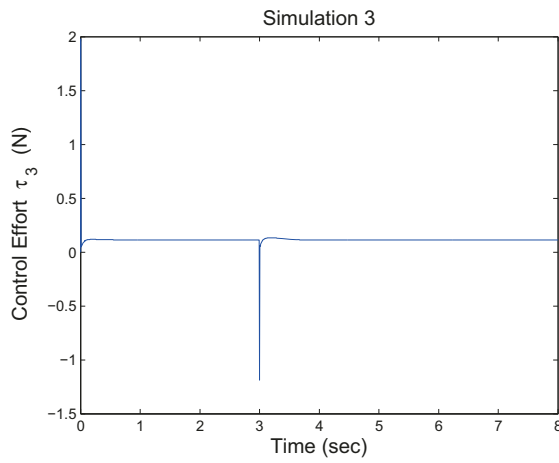


Figure 7.23: Control Effort 3, Simulation 3.

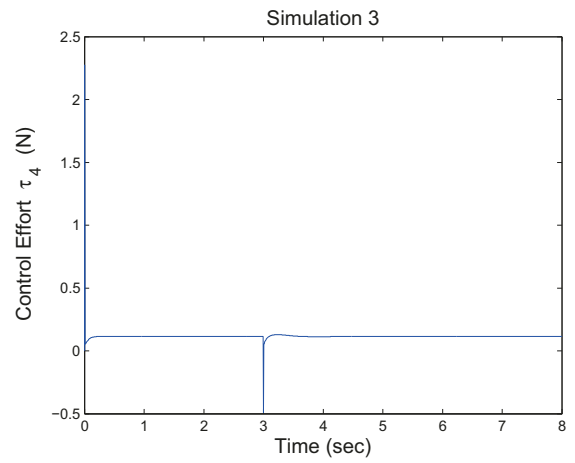


Figure 7.24: Control Effort 4, Simulation 3.

## Experimental Results

This chapter concerns the real-time implementation of the attitude estimation and stabilization algorithms discussed throughout this document. The physical setup as well as the individual hardware parts are described. Several experiments are performed, while the results are presented in the final section of this chapter.

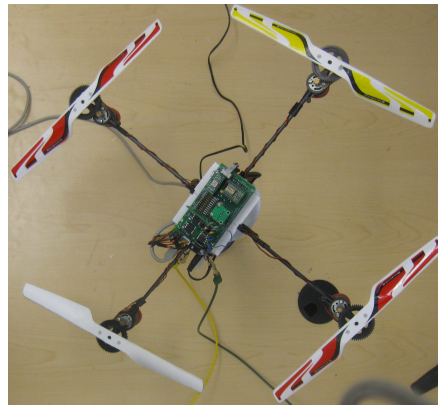


Figure 8.1: The Quadrotor Aerial Robot in Automatic Control Lab.

### 8.1 Test-bed Platform

To implement the discussed algorithms through this project, a commercial mini-scale quadrotor aerial robot called *DraganFlyer*<sup>®</sup> - III was used. While the airframe, motors and propeller sets were kept, the original control unit PCB was discarded and replaced by a customized PCB board equipped with the inertial sensors for attitude estimation purpose as well as motors driver circuitries. In addition, the necessary power safety and distribution plants were designed and implemented on the same PCB. To complete the control set-up, a microprocessor was added to the electronic design.

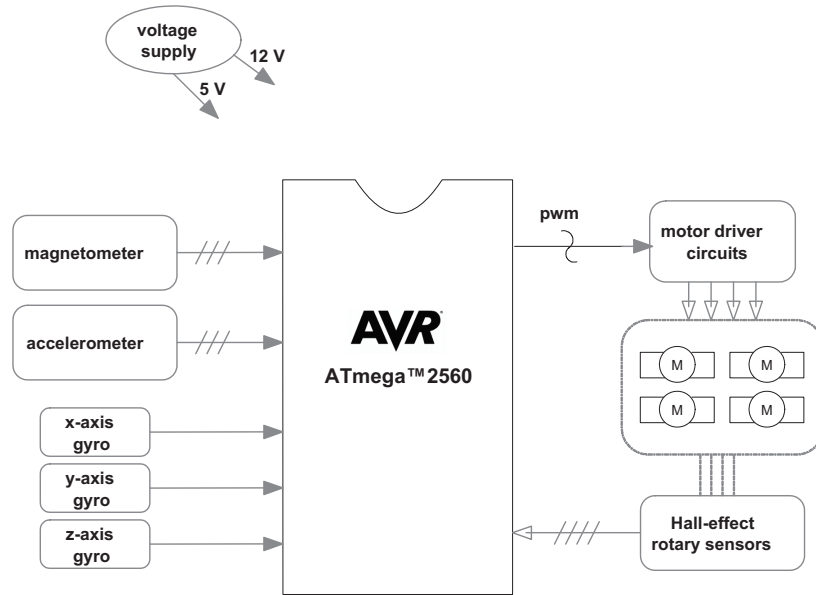


Figure 8.2: Hardware Communication Diagram.

Figure (8.2) depicts the hardware communication of the customized control unit designed for the aerial vehicle under consideration.

### 8.1.1 Actuators

In the quadrotor platform under study, the four motors mounted on the airframe are permanent magnet brushed DC motors manufactured by *mabuchi*<sup>®</sup>. These motors take a maximum voltage of 12V and offer the speed of approximately 9000rpm under no-load conditions in maximum efficiency. Since the rotation of each rotor is unidirectional (*i.e.*, for each motor the direction of rotation is not expected to vary during the flight), a possible scheme is using MOSFET based circuits to drive the motors by pulse width modulation (PWM) signals.

In the driver circuitries designed for this project, *LZ44Z* power MOSFETs are used, dimensioned for the 490 Hz switching frequency.

### 8.1.2 Processor and Software

Prior to the selection of a microcontroller, the technical features offered by a mentionable number of microcontroller chips were investigated in terms of the required criteria such as light weight, relatively large number of available analog input pins, number of available pins capable of providing PWM sig-

nals and available memory. *ArduinoMega*<sup>®</sup> 2560 is the electronic prototype board with an AVR<sup>®</sup> chip, *Atmege 2560* as the core processor, chosen to be used in this project. The microcontroller operates at  $20MHz$  and must be programmed in *C*. In addition to monitoring the sensors, the chip provides the required control signals to the four motors of the quadrotor while processing the estimation and control algorithms.

The *ArduinoMega*<sup>®</sup> prototype board handles up to  $12V$  input power and has the capability of providing two different output voltages,  $3.3V$  and  $5V$ . This factor has been used in the control platform design to power the inertial sensors.

### 8.1.3 Sensors

- **Inertial sensors:** three gyroscopes as well as a 3-axis accelerometer and 3-axis magnetometer are used. The detailed specifications of these type of sensors have been discussed in earlier chapters. All inertial devices used in physical setup are analog sensors. In the control board design, wired transformation of analog signals have been avoided to decrease the risk of noise. Additionally, to eliminate the noise generated in presence of motor vibrations, the collected data from the inertial sensors were low pass filtered in software, with a cut-off frequency of  $10Hz$ .

The analog signals are converted to 10 bit digital data by the internal *A/D* in the microcontroller. While this fact doesn't have a considerable impact on the accuracy of gyros and accelerometer readings in the problem under consideration, the conditions are relatively more challenging for magnetometer measurements. As the geographical location in which the tests are performed is relatively close to the North, the horizontal component of the Earth magnetic field has a small value. When the customized IMU is pitched, the magnetic field sensed in the horizontal surface of the magnetometer decreases to a very small value. Under such conditions, since the magnetometer has a limited sensitivity, the accuracy of measurements decreases when the pitch angle increases. The restricted accuracy in *A/D* intensifies this problem.

- **Hall-effect sensors :** in addition to the inertial sensors used for attitude estimation, Hall-effect rotary sensors are used in the hardware platform to determine the angular velocity of the motors. The sensors under consideration, are light weight three-terminal voltage-output devices working based on Hall effect. There are two small magnetic sticks

originally mounted on the rotors,  $180^\circ$  apart from each other. The Hall-effect rotary sensors are placed in a fixed position under the main rotor gear. While the normal output of the sensor is  $5V$ , sensing the magnet stick in close distance causes the device to output  $0V$ . Consequently, the angular speed of the rotors can be calculated by measuring the time interval  $t_{on}$  in which the output signal stays high. It has been shown by experiments [26] that for any given frequency,

$$2 t_{on} = 0.8737 t_{rev}$$

where  $t_{rev}$  denotes the time for one rotor revolution expressed in seconds. Therefore, the angular velocity of each rotor can be calculated as

$$\omega_i = \frac{2\pi}{t_{rev}} = \frac{0.8737\pi}{t_{on}} \text{ (rad/s)}$$

#### 8.1.4 Discussion

Through this project, the microcontroller was managed to update the rotors speed readings every  $0.02 \text{ sec}$ . To avoid the halt in calculations due to low speed of the rotors, a minimum angular velocity and a maximum waiting time have been considered in the program. If no low pulse was detected during the specified waiting time, the measured angular velocity would be considered zero. However, the reading process for the Hall-effect sensors causes a time delay in the whole program. This problem prevented the control system to react within the appropriate time and any further attempts for stabilizing the customized quadrotor platform were turned unsuccessful.

## 8.2 Experimental Data

To explore the real-time performance of attitude estimation algorithms, several experiments were performed. A number of these experiments are described in the following sections, while the results are presented and discussed. Two different estimation algorithms were coded into the microcontroller and the data containing the estimated orientation were collected using *Eltima*<sup>®</sup> serial data logger software. The sampling time is about 0.03 sec while the orientation of the aircraft and the estimation algorithms gains are given in table (8.1).

| Parameter         | Value                                             |
|-------------------|---------------------------------------------------|
| Observer 1, Gains | $\gamma_1 = 35$<br>$\gamma_2 = 4$                 |
| Observer 2, Gains | $\alpha = 5$<br>$\gamma_1 = 35$<br>$\gamma_2 = 4$ |

Table 8.1: Experiment 1 Parameters

While the customized control unit has been strapped down rigidly on a commercial IMU, the physical setup was moved in a series of rotations. The objective of this experiment is to compare the estimated orientation provided by the attitude observers with the precise orientation given by the commercial IMU. The IMU device used during this experiment is *3DM-GX1*<sup>®</sup> manufactured by *Microstrain*. While the sampling times of the industrial and the customized IMUs were synchronized, the estimated orientation data were collected. The plots are given for the estimated orientations, making a comparison possible. As mentioned earlier, this experiment has been repeated for several rotational motions. These movements are described in the following.

- **Experiment 1-1:** the estimation algorithm 1 was coded in the microcontroller and the setup was forced through a random roll movement. While the setup was undergoing such motion, the estimated orientation provided by both commercial and customized IMUs were collected and the corresponding components were plotted in the same figure to make a simple comparison possible. The results for the estimated quaternion components are presented in figures (8-3)-(8-6).
- **Experiment 1-2:** the estimation algorithm 1 was coded in the microcontroller and the setup was forced through a random pitch movement.

To verify the real-time performance of the customized IMU and check whether it is capable of a relatively accurate attitude estimation, the output data was collected from both commercial and customized IMUs. Corresponding quaternion components have been plotted in the same figure to make a simple comparison possible. The results are depicted in figures (8.7)-(8.10).

- **Experiment 1-3:** the estimation algorithm 1 was coded in the micro-controller and the setup was forced through a random yaw movement. While the setup was undergoing such motion, the estimated orientation provided by both commercial and customized IMUs were collected and the corresponding components were plotted in the same figure to make a simple comparison possible. The results for the estimated quaternion components are presented in figures (8-7)-(8-10).
- **Experiment 2-1:** the estimation algorithm 2 was coded in the micro-controller and the setup was forced through a random roll movement. To verify the real-time performance of the customized IMU and check whether it is capable of a relatively accurate attitude estimation, the output data was collected from both commercial and customized IMUs. Corresponding quaternion components have been plotted in the same figure to make a simple comparison possible. The results are depicted in figures (8.11)-(8.14).
- **Experiment 2-2:** the estimation algorithm 2 was coded in the micro-controller and the setup was forced through a random pitch movement. While the setup was undergoing such motion, the estimated orientation provided by both commercial and customized IMUs were collected and the corresponding components were plotted in the same figure to make a simple comparison possible. The results for the estimated quaternion components are presented in figures (8-5)-(8-18).
- **Experiment 2-3:** the estimation algorithm 2 was coded in the micro-controller and the setup was forced through a random yaw movement. To verify the real-time performance of the customized IMU and check whether it is capable of a relatively accurate attitude estimation, the output data was collected from both commercial and customized IMUs. Corresponding quaternion components have been plotted in the same figure to make a simple comparison possible. The results are depicted in figures (8.19)-(8.22).
- **Experiment 3-1:** the estimation algorithm 1 was coded in the micro-controller and the setup was forced through a random 3 dimensional

movement. While the setup was undergoing such motion, the estimated orientation provided by both commercial and customized IMUs were collected and the corresponding components were plotted in the same figure to make a simple comparison possible. The results for the estimated quaternion components are presented in figures (8-23)-(8-26).

- **Experiment 3-2:** the estimation algorithm 2 was coded in the microcontroller and the setup was forced through a random 3 dimensional movement. Similar to the previous experiments, the estimated orientation provided by both commercial and customized IMUs were collected and the corresponding components were plotted in the same figure to make a simple comparison possible. The results for the estimated quaternion components are presented in figures (8-27)-(8-30).

As it is clearly confirmed by the experimental results for several random movements that, the estimated orientation given by both algorithms are relatively accurate in terms of estimating the first three components of the quaternion. A slight difference can be seen between the estimated  $q_3$  and its real value provided by 3DM-GX1. It can be deduced from the experimental data that,  $q_3$  component is effectively involved with the yaw motion of the aircraft and consequently it is strongly dependant on the magnetometer readings. Since the experiments have been performed in an environment surrounded by electrical equipments and power cables, a possible reason for this misalignment can be the lack of an appropriate soft-iron calibration for the magnetometer under consideration.

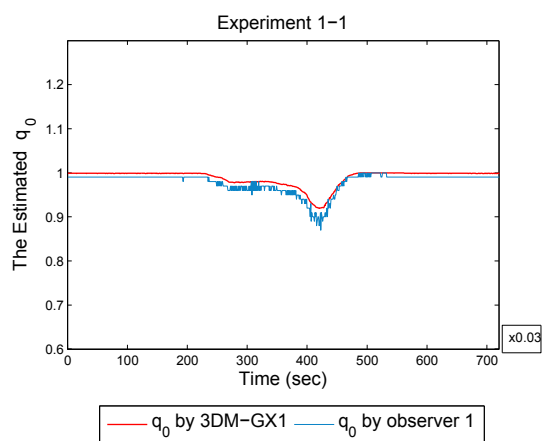


Figure 8.3: The Estimated  $q_0$ , Experiment 1-1.

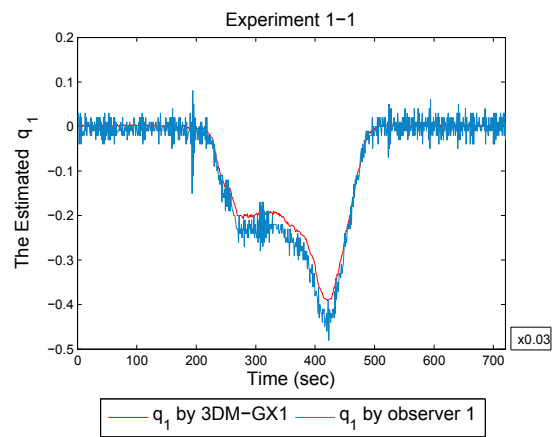


Figure 8.4: The Estimated  $q_1$ , Experiment 1-1.

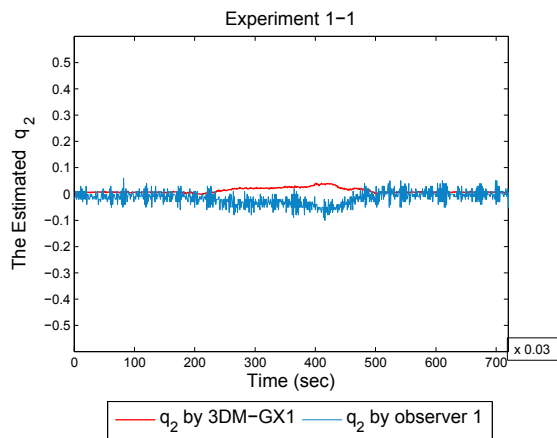


Figure 8.5: The Estimated  $q_2$ , Experiment 1-1.

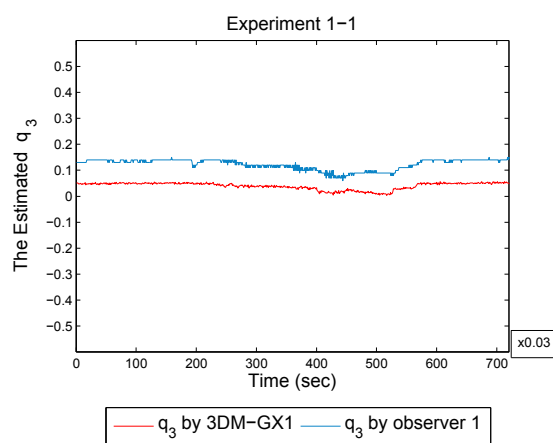


Figure 8.6: The Estimated  $q_3$ , Experiment 1-1.

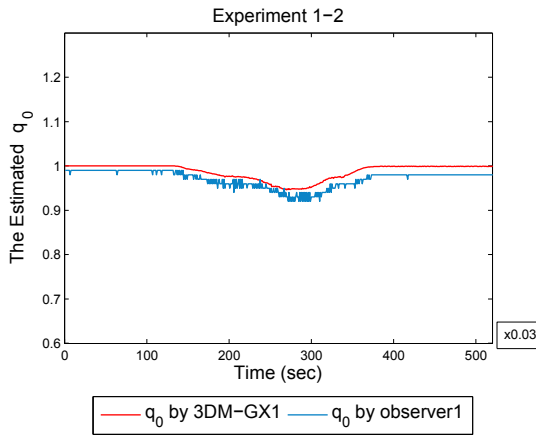


Figure 8.7: The Estimated  $q_0$ , Experiment 1-2.

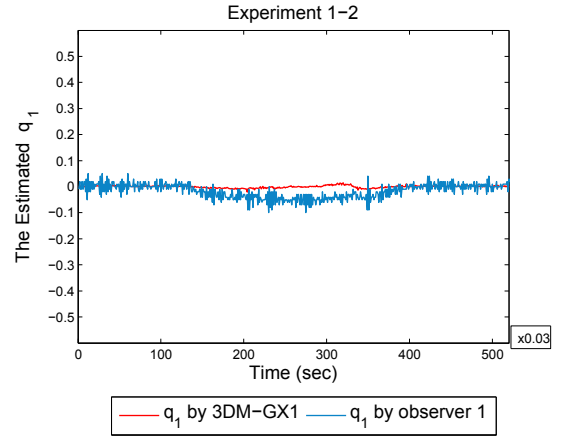


Figure 8.8: The Estimated  $q_1$ , Experiment 1-2.

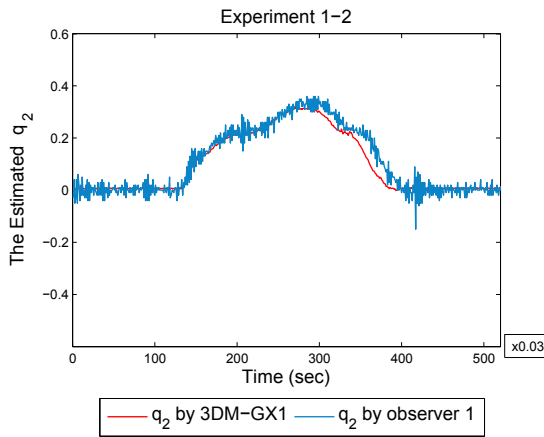


Figure 8.9: The Estimated  $q_2$ , Experiment 1-2.

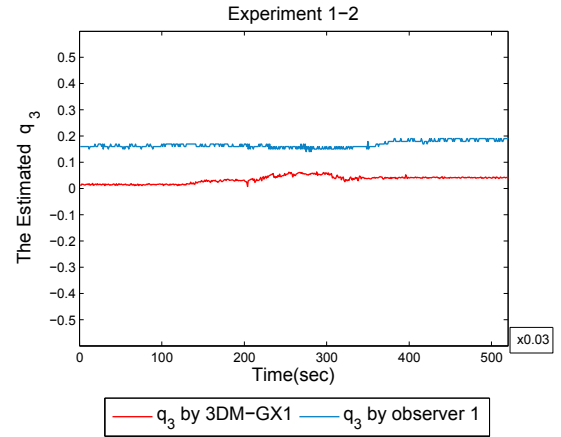


Figure 8.10: The Estimated  $q_3$ , Experiment 1-2.

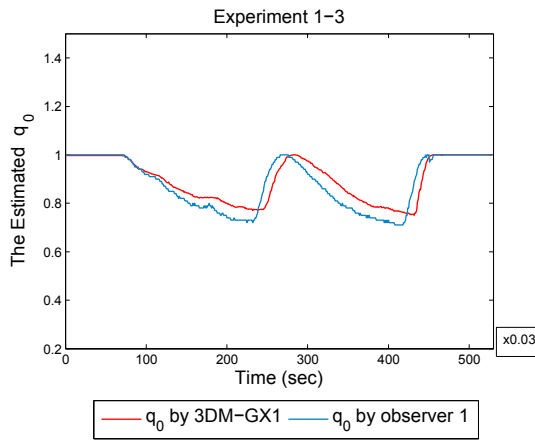


Figure 8.11: The Estimated  $q_0$ , Experiment 1-3.

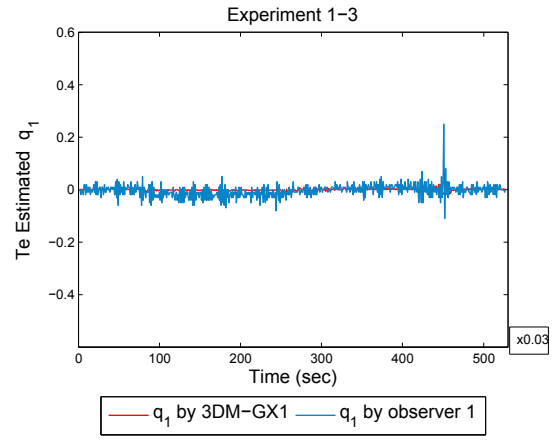


Figure 8.12: The Estimated  $q_1$ , Experiment 1-3.

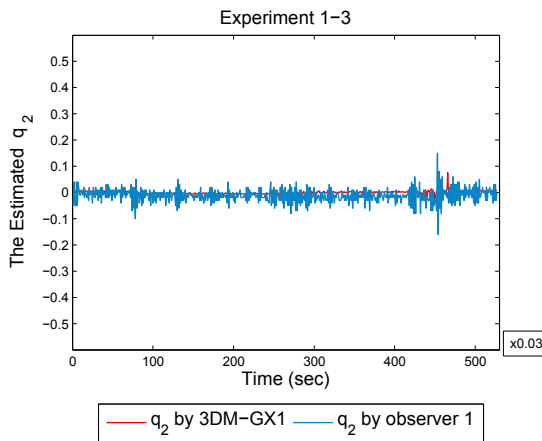


Figure 8.13: The Estimated  $q_2$ , Experiment 1-3.

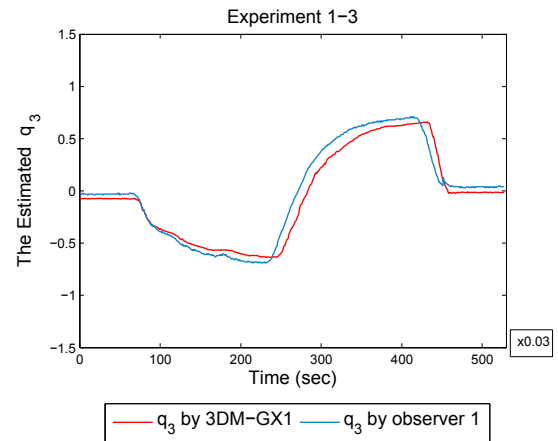


Figure 8.14: The Estimated  $q_3$ , Experiment 1-3.

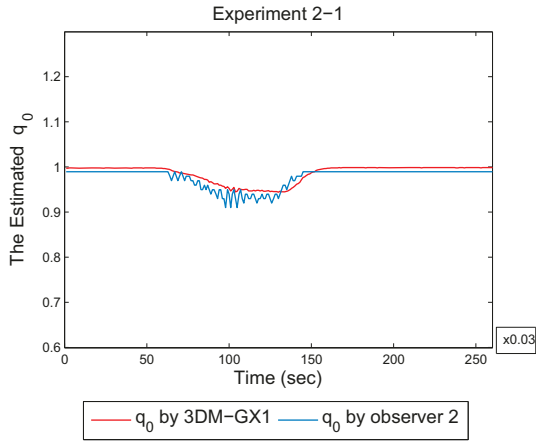


Figure 8.15: The Estimated  $q_0$ , Experiment 2-1.

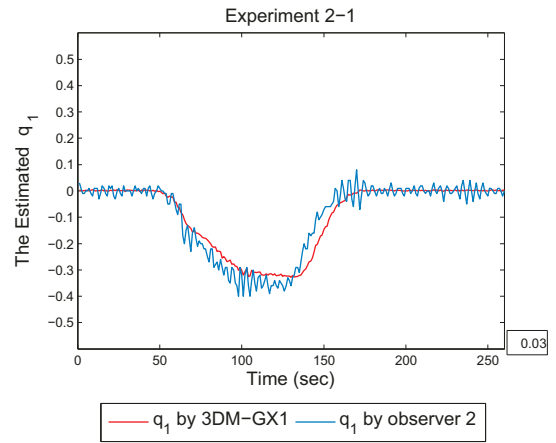


Figure 8.16: The Estimated  $q_1$ , Experiment 2-1.

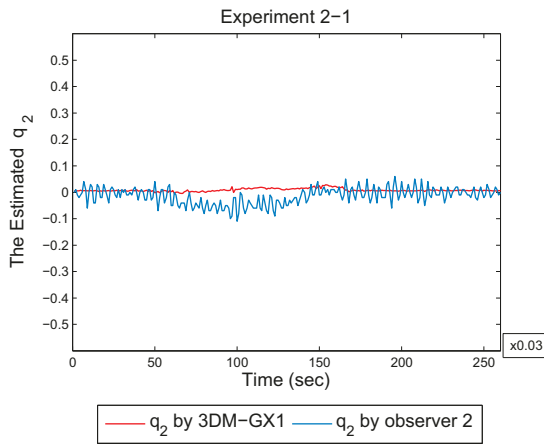


Figure 8.17: The Estimated  $q_2$ , Experiment 2-1.

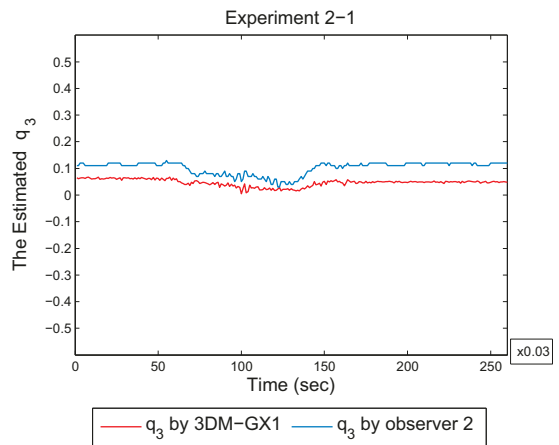


Figure 8.18: The Estimated  $q_3$ , Experiment 2-1.

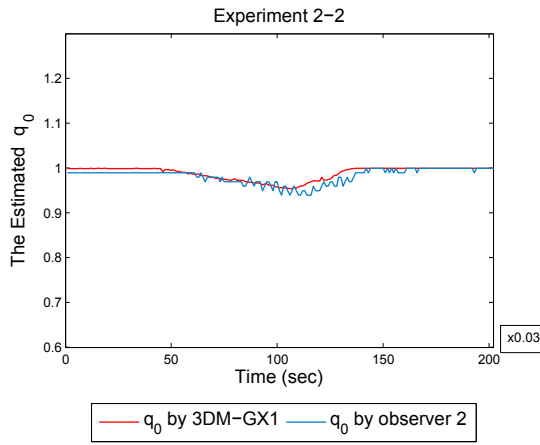


Figure 8.19: The Estimated  $q_0$ , Experiment 2-2.

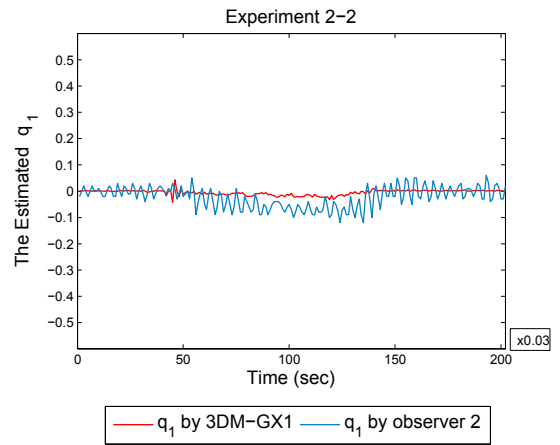


Figure 8.20: The Estimated  $q_1$ , Experiment 2-2.

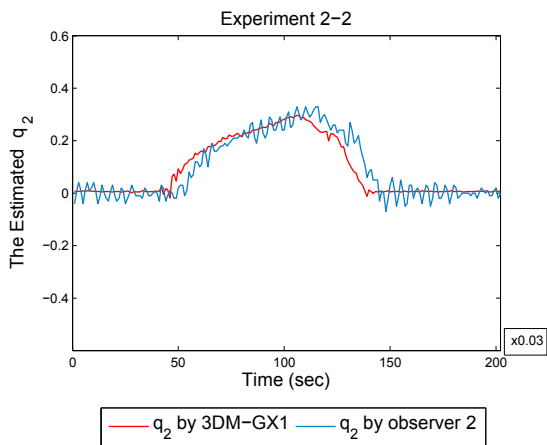


Figure 8.21: The Estimated  $q_2$ , Experiment 2-2.

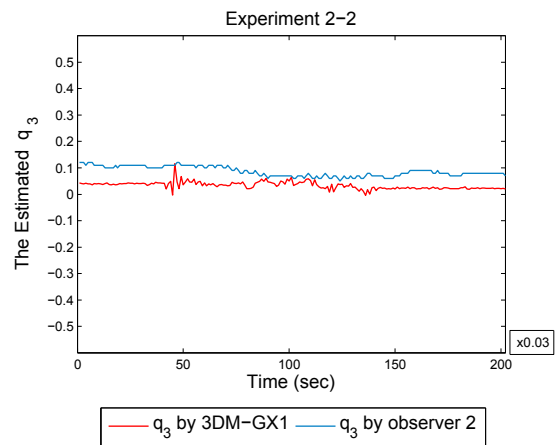


Figure 8.22: The Estimated  $q_3$ , Experiment 2-2.

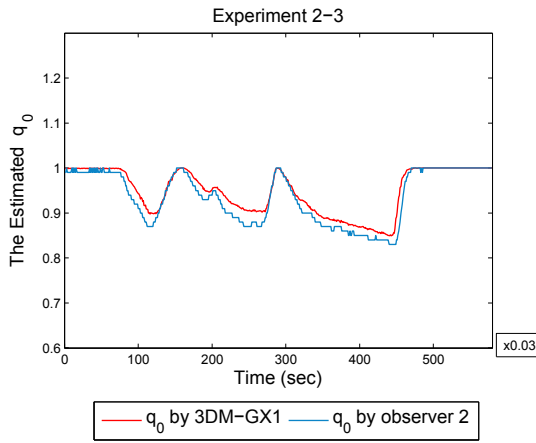


Figure 8.23: The Estimated  $q_0$ , Experiment 2-3.

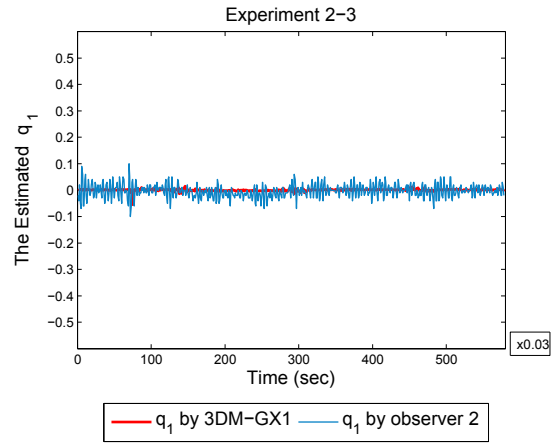


Figure 8.24: The Estimated  $q_1$ , Experiment 2-3.

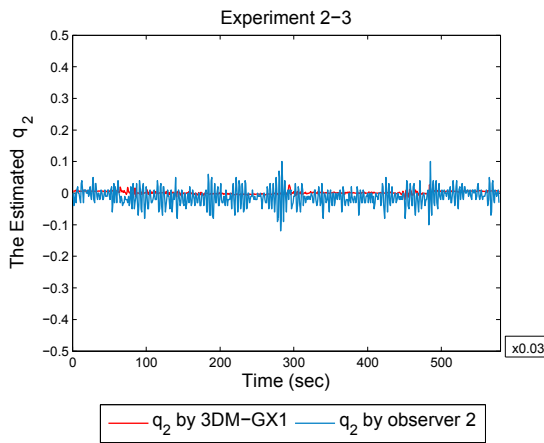


Figure 8.25: The Estimated  $q_2$ , Experiment 2-3.

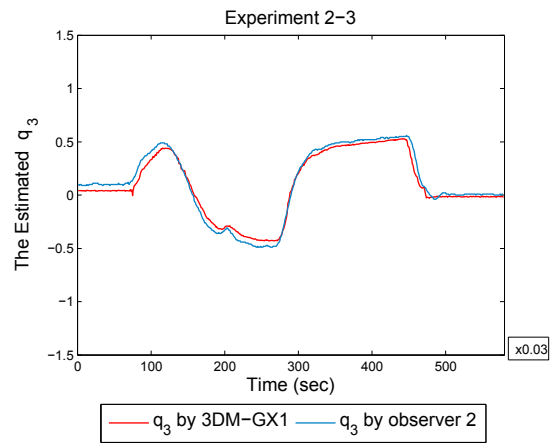


Figure 8.26: The Estimated  $q_3$ , Experiment 2-3.

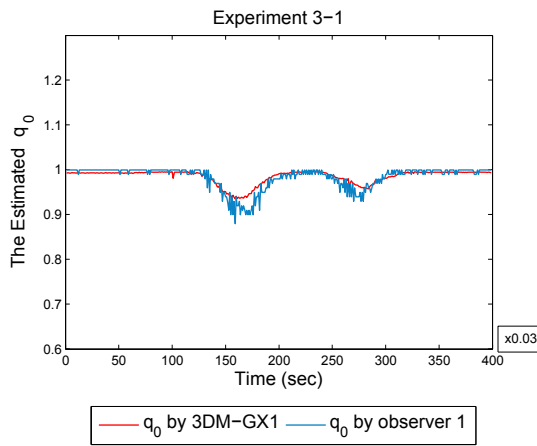


Figure 8.27: The Estimated  $q_0$ , Experiment 3-1.

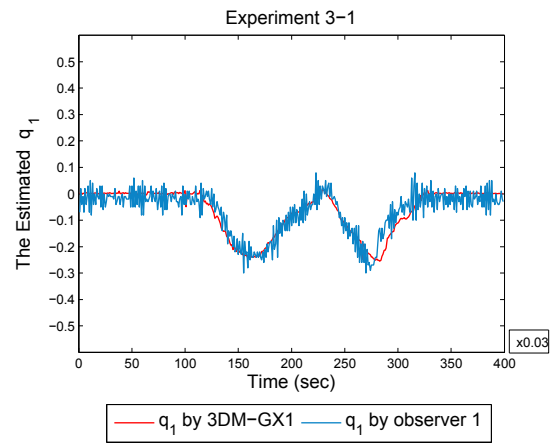


Figure 8.28: The Estimated  $q_1$ , Experiment 3-1.

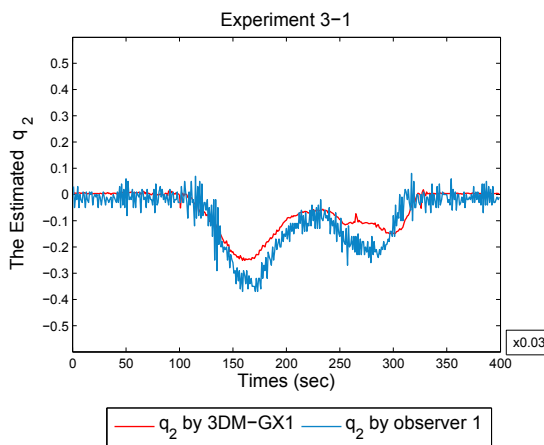


Figure 8.29: The Estimated  $q_2$ , Experiment 3-1.

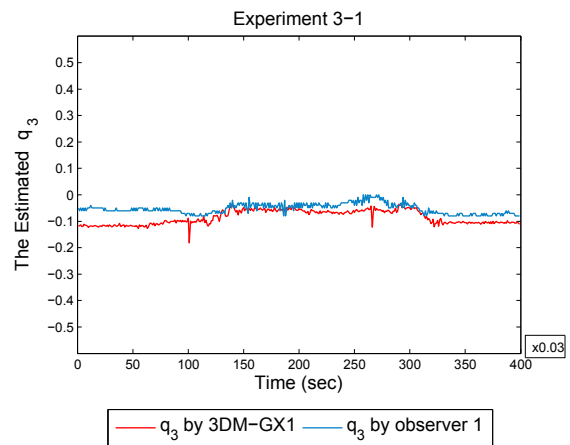


Figure 8.30: The Estimated  $q_3$ , Experiment 3-1.

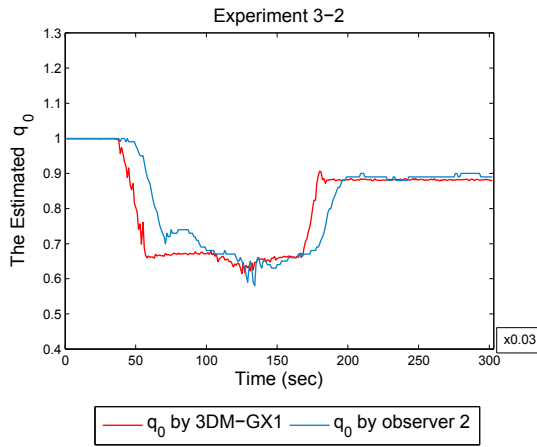


Figure 8.31: The Estimated  $q_0$ , Experiment 3-2.

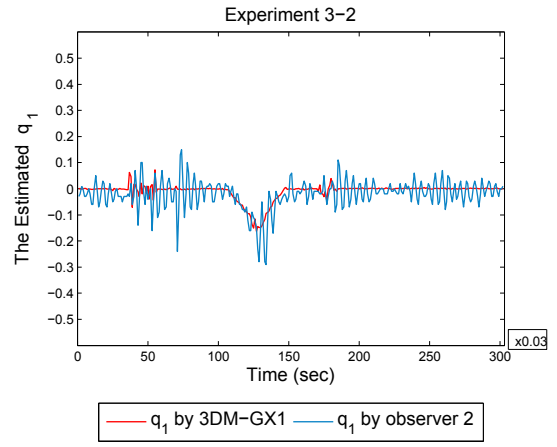


Figure 8.32: The Estimated  $q_1$ , Experiment 3-2.

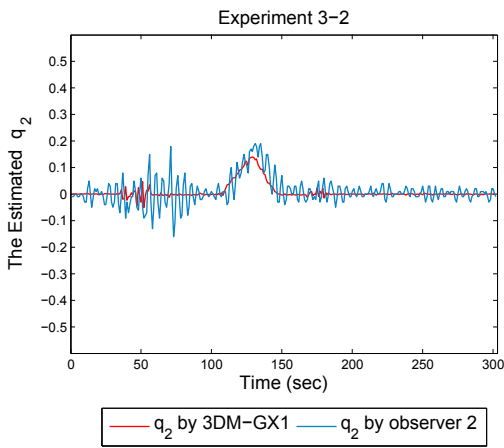


Figure 8.33: The Estimated  $q_2$ , Experiment 3-2.

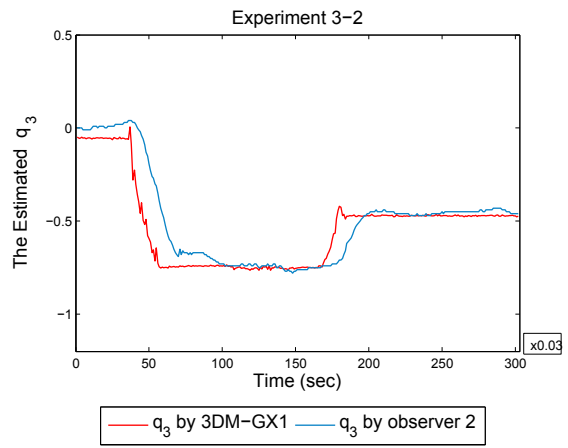


Figure 8.34: The Estimated  $q_3$ , Experiment 3-2.

## Conclusion

The development of unmanned aerial vehicles has been the subject of extensive research over the past decade. These type of vehicles are considered as a promising design to serve in many civil and military applications including surveillance, intervention in hostile environments, remote monitoring, and area mapping. The recent revolutionary advances in measurement techniques, computing power and wireless communication have made it possible to deploy an inexpensive UAV system to operate autonomously.

Quadrotor aerial robot is a prevalent test-bed for autonomous flight experiments due to the numerous advantages in terms of simplicity and intuitive motion control. This configuration is a highly nonlinear, multi-variable, strongly coupled and under-actuated system. To control six degrees of freedom, only four control inputs are used in such system. The development of a mini scale quadrotor aerial robot capable of autonomous hovering flight has been the main objective in this thesis.

Accurate attitude estimation is the prerequisite cornerstone to control the orientation and balance a rigid body in three-dimensional space. Despite being recommended by theory, the integration of aircraft kinematics is not a practically reliable approach for attitude determination, due to the time-varying additive biases involved with the angular rate measurements. To obtain a more accurate estimation of the attitude, in addition to three orthogonal angular rate sensors, a 3-axis accelerometer and 3-axis magnetometer have been used to provide the body-fixed vector measurements from the Earth gravity acceleration and magnetic field. Two different attitude observers were discussed in this thesis [41]. These algorithms have been implemented for the first time through this project and several real-time experiments have been performed. The first algorithm is based on the use of raw vector measurements, while the second observer uses filtered vector measurements.

The accuracy of vector measurements has a crucial role in both estimation algorithms. Since the accelerometer and magnetometer measurements are contaminated with biases, appropriate calibration methods have been dis-

cussed to reduce the effect of sensor biases. Both attitude observers presented in this thesis are capable of tracking a broad range of dynamical movements and are not dependant on any external signal sources such as GPS or optical trackers.

A model size quadrotor aerial robot has been developed using a pre-owned commercially available airframe. A whole new electronic platform has been designed and mounted. The physical setup has been used to demonstrate the real-time performance of the algorithms discussed throughout this thesis.

There are a number of open issues and future works that could be done to improve the attitude control system. These issues are addressed in order of priority in the following section.

## 9.1 Perspectives

- To the knowledge of the author, the main complications experienced in this research have been related to the sensor inadequacies. The performance of the system is directly related to the accuracy, delay and update rate of the attitude estimation. Using higher sampling rates, more accurate ADC (12 or 16-bit) would improve the accuracy of the estimated attitude. Also, more precise measurements are possible either by using digital sensors or external 16-bit ADC devices implemented close to the analog sensors.
- The accuracy of the magnetic field measurement was proved to be vital in precise yaw estimation. Performing further flight experiments in outdoor environment would enhance the estimation results, due to the absence of possible magnetic disturbances.
- Substitution of brushed DC motors in the current setup, with brushless counter-parts improves the reliability of the system in the sense of high thrust to weight ratio and decreases the noise and vibration generated by motors.

## Identification of Model Parameters

To implement the controller algorithm, a number of parameters related to the hardware components need to be determined. Through this project, assuming four motors are the same, model parameters were identified for one motor. The parameters determination methods are inspired by the early works done on this platform in 2003, [26].

While the armature resistance,  $R_a$  was measured simply by a multimeter, the gear ratio,  $K_g$  was determined by counting the number of teeth on gears. The remaining parameters are measured through more sophisticated methods as explained in the following sections.

### Motor Constant, $K_m$

As mentioned earlier, assuming the electrical loss and friction to be negligible, the torque generated by a simple DC motor depends on the current flowing through the motor circuit. Such relation can be written as

$$\tau_m = K_m I_a \quad (\text{A.1})$$

On the other hand, the preliminary assumption of no energy loss indicates that the electrical power injected to a DC motor system equals the outgoing mechanical power. This can be written as

$$V_a I_a = \tau_m \omega_m \quad (\text{A.2})$$

where  $V_a$  and  $I_a$  represent the armature voltage and current respectively. Combination of equations (A.1) and (A.2) leads to finding a formulation for motor constant  $K_m$ , given as

$$K_m = \frac{V_a}{\omega_m} = \frac{\tau_m}{I_a} \quad (\text{A.3})$$

Considering the above expression, while the motor is under no-load conditions (the propeller is removed), the back emf voltage and corresponding

| Input Voltage | $I_a$ (A) | $V_a$ (V) | $\omega_m$ (rad/s) | $K_m$ (N.m/A) |
|---------------|-----------|-----------|--------------------|---------------|
| 3.58          | 0.09      | 3.481     | 812                | 0.004286      |
| 5.6           | 0.15      | 5.435     | 1288               | 0.004219      |
| 6.8           | 0.20      | 6.28      | 1590.4             | 0.00395       |
| 7.8           | 0.23      | 7.547     | 1859.2             | 0.00406       |
| 8.9           | 0.24      | 8.636     | 2071               | 0.00417       |
| 9.5           | 0.26      | 9.214     | 2223.2             | 0.00414       |

Table A.1: Collected Data for Motor Constant Identification.

angular velocity data were measured. For each set of data, a  $K_m$  value can be calculated. Table (A.1) shows the results of such experiment.

Through this project, the average of  $K_m$  values presented in the above table is used as the motor constant.

### Moment of Inertia

A relatively simple way to determine the body moment of inertia, is the experiment-based method called *compound pendulum* [26]. In this experiment, suspending the aircraft while only the very end of one axis is fixed to a surface, the mass is twisted. Acting like a pendulum, a torque is applied to the mass, tending to rotate it back to its original position. This makes the mass to oscillate back and forth, creating a harmonic motion. Once the resonance frequency of this oscillation is known, the moment of inertia can be determined as

$$I = \frac{mgl}{\omega_n^2} - ml^2 \quad (\text{A.4})$$

where  $\omega_n$  and  $m$  represent the natural frequency and the mass respectively. Also  $l$  and  $g$  denotes the distance between the fixed point of oscillation and the center of gravity (in this case, the center of mass of the aircraft) and gravity acceleration respectively.

To calculate the body inertia, the parameters  $m$  and  $l$  were simply measured and determined to be  $500.71g$  and  $23.2cm$  respectively.

To ensure the reliability of the compound pendulum experiment, it was repeated seven times. The time interval of four complete cycles,  $t_{4cyc}$  was recorded for each trial. To determine the natural frequency of oscillation  $\omega_{n,\varphi}$  about yaw axis, the results of trial sessions are presented in table (A.2).

| Trial | $t_{4cyc}$ (sec) |
|-------|------------------|
| 1     | 4.088            |
| 2     | 4.527            |
| 3     | 4.795            |
| 4     | 5.251            |
| 5     | 5.374            |
| 6     | 4.775            |
| 7     | 4.906            |

Table A.2: Collected Data for Determination of Body Inertia Component  $I_{f_\varphi}$ .

While the average time is given as

$$t_{ave,\varphi} = 4.816 \text{ sec},$$

the natural frequency of the oscillations is calculated as,

$$\omega_{n,\varphi} = 5.21 \text{ rad/s}$$

Substitution of these parameters in equation (A.4), yields to finding the mass moment of inertia given by

$$I_{f_\varphi} = \frac{(0.50071)(9.81)(0.232)}{(5.21)^2} - (0.50071)(0.232)^2 = 1.33 \times 10^{-2}$$

Since the quadrotor configuration is symmetrical the moment of inertia around roll and pitch axes are the same. To determine these parameters, the experiments were performed similar to those for the identification of  $I_{f_\varphi}$ . Table (A.3) shows the collected data in terms of  $t_{4cyc}$  in several trials.

Using the information in table (A.3), we can calculate

$$t_{ave} = 4.122 \text{ sec}$$

also

$$\omega_{n,\theta} = 6.094 \text{ rad/s}$$

Replacing these values in equation (A.4) results in

$$I_{f_\theta} = \frac{(0.50071)(9.81)(0.232)}{(6.094)^2} - (0.50071)(0.232)^2 = 3.735 \times 10^{-3}$$

| Trial | $t_{4cyc}$ (sec) |
|-------|------------------|
| 1     | 4.405            |
| 2     | 4.014            |
| 3     | 4.134            |
| 4     | 3.698            |
| 5     | 4.432            |
| 6     | 3.728            |
| 7     | 4.445            |

Table A.3: Collected Data for Determination of Body Inertia Component  $I_{f\theta}$ .

Therefore, the mass moment of inertia is identified as

$$I_f = \text{diag}(I_{f\psi}, I_{f\theta}, I_{f\varphi}) = \text{diag}(3.735, 3.735, 13.3) \times 10^{-3}$$

Also, a similar approach was used to determine the rotor inertia. Considering  $l = 15$  cm and  $m = 6.71$  g, table (A.4) shows the data collected via experiments.

| Trial | $t_{4cyc}$ (sec) |
|-------|------------------|
| 1     | 3.42             |
| 2     | 3.623            |
| 3     | 3.260            |
| 4     | 3.612            |
| 5     | 3.76             |
| 6     | 3.517            |
| 7     | 3.548            |

Table A.4: Collected Data for Determination of Rotor Inertia  $I_r$ .

While  $t_{ave}$  is calculated as 3.53 sec, the natural frequency is given by

$$\omega_{n,r} = 7.11 \text{ rad/s}$$

Hence, the rotor moment of inertia is obtained as

$$I_r = \frac{(0.00671)(9.81)(0.15)}{(7.11)^2} - (0.00671)(0.15)^2 = 4.43 \times 10^{-5}.$$

## Mathematical Notation and Identities

In this section, a brief overview is given for a number of important mathematical notations used through this thesis.

**Rotation matrix :**A rotation  $R$  maps an orthonormal basis to another orthonormal coordinate. This orthonormality condition can be expressed as

$$R^T R = I \quad (\text{B.1})$$

where  $I$  is the identity matrix

$$I = \begin{pmatrix} 1 & 0 & 0 \\ 0 & 1 & 0 \\ 0 & 0 & 1 \end{pmatrix} \quad (\text{B.2})$$

Rotation matrices preserve the length of vectors undergoing the rotation. Every rotation can be represented uniquely by an orthogonal matrix with unit determinant. *i.e.*,

$$\det(R) = 1 \quad (\text{B.3})$$

**Skew-symmetric matrix:** Let  $u$  and  $v$  denote two arbitrary vectors,  $u, v \in \mathbb{R}^3$ . The following identities can be described.

$$S(u) = \begin{pmatrix} 0 & -u_3 & u_2 \\ u_3 & 0 & -u_1 \\ -u_2 & u_1 & 0 \end{pmatrix} \quad (\text{B.4})$$

For any two skew-symmetric matrices, commutation is defined as

$$[S(u), S(v)] = S(u)S(v) - S(v)S(u) \quad (\text{B.5})$$

**Cross Product:**

$$u \times v = S(u)v = \begin{pmatrix} u_2v_3 - u_3v_2 \\ u_3v_1 - u_1v_3 \\ u_1v_2 - u_2v_1 \end{pmatrix} \quad (\text{B.6})$$

**Dot Product**

$$u \cdot v = u^T v = u_1 v_1 + u_2 v_2 + u_3 v_3 \quad (\text{B.7})$$

**Norm**

- Vector norm

$$\|u\| = \sqrt{u^T u} = \sqrt{u_1^2 + u_2^2 + u_3^2} \quad (\text{B.8})$$

- Matrix norm

$$\|A\| = \left( \sum_{i=1}^m \sum_{j=1}^n A_{ij} \right)^{\frac{1}{2}} \quad (\text{B.9})$$

**Quaternion Form:**

$$\bar{v} = \begin{pmatrix} 0 \\ v \end{pmatrix} \quad (\text{B.10})$$

**Other important Notations**

$$S(Rv) = RS(v)R^T \quad (\text{B.11})$$

$$\|v\|^2 = \frac{1}{2} \|S(v)\|^2 \quad (\text{B.12})$$

# Bibliography

- [1] <http://rctoys.ca>.
- [2] <http://aero.stanford.edu/Reports/AHSPaper.pdf>.
- [3] <http://hybrid.eecs.berkeley.edu/starmac/>.
- [4] J. C. Myers A. Gessow, *Aerodynamics of the helicopter*, F. Ungara Pub. Co., 1967.
- [5] E. Altug, *Vision based control of unmanned aerial vehicles with applications to an autonomous four-rotor helicopter, quadrotor.*, PHD Dissertation, Pensilvania University, 2004.
- [6] M. Anderjasic, *Mems accelerometers*, seminar report, University of Ljubljana, 2008.
- [7] J. Bernstein, *An overview of mems inertial sensing technology*, Corning IntelliSense Corp., 2003.
- [8] S. Bouabdallah and R. Siegwart, *Backstepping and sliding-mode techniques applied to an indoor micro quadrotor*, IEEE International Conference on Robotics and Automation (ICRA) (Barcelona, Spain), 2005, pp. 2247–2252.
- [9] R. J. Brown, *Planes that go straight up; open new fields for aviation*, Popular Science Monthly **126** (1935).
- [10] M. J. Caruso, *Applications of magnetic sensors for low cost compass systems*, Position Location and Navigation Symposium. IEEE (2000), 177–184.
- [11] A. T. Conlisk, *Modern helicopter rotor aerodynamics*, Progress in Aerospace Sciences **37** (2001), 419–476.
- [12] J. L. Crassidis, *Survey of nonlinear attitude estimation methods*, Journal of Guidance, Control, and Dynamics **30** (2007).

- [13] R. Rajamani D. Piyabongkarn and M. Greminger, *The development of a mems gyroscope for absolute angle measurement*, IEEE Transactions on Control Systems Technology **13** (2005), 185–195.
- [14] A. Monin F. Camps, S. Harasse, *Numerical calibration for 3-axis accelerometers and magnetometers*, IEEE Transactions on Aerospace and Electronic Systems **47** (2011), 1293–1306.
- [15] S. Vaslander D. Dostal J. Jang G. Hoffmann, D. Rajnarayan and C. Tomlin, *The stanfor testbed of autonomous rotorcraft for multi agent control (starmac)*, In Proc. of the 23rd Digital Avionic Systems Conference (Salt Lake City, UT), 2004.
- [16] S. L. Wasl G. M. Hoffmann, H. Huang and J. Tomlin, *Quadrotor helicopter flight dynamics and control: Theory and experiment*, In Proc. of the AIAA Guidance, Navigation, and Control Conference, 2007.
- [17] C. Gablehouse, *Helicopters and autogiros; a history of rotating-wing and v/stol aviation*, J.B. Lippincott Company, 1969.
- [18] W. R. Hamilton, *On quaternions; or on new system of imaginaries in algebra*, Philosophical Magazine **25** (1844), 489–495.
- [19] M. D. Hua, *Attitude observers for accelerated rigid bodies based on gps and ins measurements*, In proc. of the 48th IEEEConference on Decision and Control (Shanghai, China), 2009, pp. 8071–8076.
- [20] A. Martinez B. Lafavergeres J. Colorado, A. Barrientos and J. Valente, *Mini-quadrotor attitude control based on hybrid backstepping amp; frenet-serret theory*, IEEE International Conference on Robotics and Automation (ICRA) (Anchorage, AK), 2010, pp. 1617 – 1622.
- [21] C. Silvestre P. Oliveira B. Cardeira J. F. Vasconcelos, G.Elkaim, *Geometric approach to strapdown magnetometer calibration in sensor frame*, IEEE International Conference on Electro/Information Technology, 2009. eit '09 (2009), 217–221.
- [22] M. Johnson, *Helicopter theory*, Courier Dover Publications, 1994.
- [23] J. C. Leishman, *Principles of helicopter aerodynamics*, Cambridge University Press, 2000.
- [24] R. Mahony, T. Hamel, and J.-M. Pfimlin, *Complementary filter design on the special orthogonal group  $so(3)$* , Decision and Control, 2005 and

- 2005 European Control Conference. CDC-ECC '05. 44th IEEE Conference on, dec. 2005, pp. 1477 – 1484.
- [25] R. A. Mayo, *Relative quaternion state transition relation*, Journal of Guidance and Control **2** (1979).
- [26] S. J. McGilvray, *Attitude stabilization of a quadrotor aircraft*, M.Sc Thesis, Lakehead University, 2004.
- [27] K. Munson, *Helicopters and other rotorcraft since 1907*, LONDON, BLANDFORD PRESS, 1973.
- [28] F. Ayazi N. Yazdi and K. Najafi, *Micromachined inertial sensors*, Proceeding of the IEEE **86** (1998), 1640–1659.
- [29] E. Salaun N. Petit P. J. Bristeau, P. Martin, *The role of propeller aerodynamics in the model of a quadrotor uav*, Proceeding of the European Control Conference (Budapest, Hungary), 2009.
- [30] J. Gresham P. Pounds, R. Mahony, *Towards dynamically-favourable quad-rotor aerial robots*, In Proceedings of American Control Conference (Canberra, Australia), 2004.
- [31] R. Mahony P. Pounds and P. Corke, *Modelling and control of a quadrotor robot*, In Proceedings of the Australian Conference on Robotics and Automation, 2006.
- [32] W. F. Phillips and C. E. Hailey, *Review of attitude representations used for aircraft kinematics*, Journal of Aircraft **12** (2004).
- [33] J. M. Pfimlin R. Mahony, T. Hamel, *Nonlinear complementary filters on the special orthogonal group*, IEEE Transactions on Automatic Control **53** (2008), 1203–1218.
- [34] J. L. Champion R. Osiander, M. A. Garrison Darrin, *Mems and microstructures in aerospace applications*, Taylor & Francis Group, 2006.
- [35] A. D. Roberts, *Attitude estimation and control of a ducted fan vtol uav*, M.Sc Thesis, Lakehead University, 2007.
- [36] P. Murrieri S. Bouabdallah and R. Siegwart, *Towards autonomous indoor micro vtol*, Autonomous Robots **18** (2005), 171–183.
- [37] M. Schneider S. Hubschmann, *Magneto resistive sensors; principles of operation and application*, ZETEX Co. application note 20 (1996).

- [38] M. D. Shuster, *A survey of attitude representations*, The Journal of Astronautical Sciences **41** (1993), 439–517.
- [39] M. N. Spong and M. Vidyasagar, *Robot dynamics and control*, John Wiley and Sons., 1984.
- [40] A. Tayebi and S. McGilvray, *Attitude stabilization of a vtol quadrotor aircraft*, IEEE Transactions on Control Systems Technology **14** (2006), 562–571.
- [41] A. Tayebi, A. Roberts, and A. Benallegue, *Inertial measurements based dynamic attitude estimation and velocity-free attitude stabilization*, In Proc. of American Control Conference (San Francisco, CA, USA), 2011.
- [42] J. T-Y. Wen and K. Kreutz-Delgado, *The attitude control problem*, IEEE Transactions on Automatic Control **36** (1991), 1148 – 1162.